

ICETI

ENGINEERING TECHNOLOGY INNOVATION

3RD INTERNATIONAL CONFERENCE ON ENGINEERING TECHNOLOGY AND INNOVATION

BOOK OF PROCEEDINGS

www.iceti.org

April 17-21 2019 Belgrade Serbia





III INTERNATIONAL CONFERENCE ON ENGINEERING TECHNOLOGY AND INNOVATION

ISBN 978-605-67955-9-6

ISSN 2687-2323

**PROCEEDINGS OF THE
III INTERNATIONAL CONFERENCE ON ENGINEERING TECHNOLOGY
AND INNOVATION**

APRIL 17-21, 2019 BELGRADE

Edited by
Prof. Dr. Özer Çınar

info@iceti.org
www.iceti.org

Publisher: CNR GROUP Publishing
www.cnrgroup.eu

CNR Group Laboratuvar ve Arge Hizmetleri Sanayi Ticaret Limited Şirketi Çifte Havuzlar Mah., Eski Londra Asfaltı Cad., Kuluçka Mrk., A1 Blok, 151/1C, İç Kapı No:1 B-20, Esenler /Istanbul, 34220

© CNR Group, 2019

This work is subject to copyright. All rights are reserved, whether the whole or part of the material is concerned. Nothing from this publication may be translated, reproduced, stored in a computerized system or published in any form or in any manner, including, but not limited to electronic, mechanical, reprographic or photographic, without prior written permission from the publisher. The individual contributions in this publication and any liabilities arising from them remain the responsibility of the authors. The publisher is not responsible for possible damages, which could be a result of content derived from this publication.

ISBN 978-605-67955-9-6

ISSN 2687-2323

SCIENTIFIC COMMITTEE

1. Prof. Dr. Adisa Parić - University of Sarajevo - Bosnia and Herzegovina
2. Prof. Dr. Aleksandar Dimitrov - Ss. Cyril and Methodius University - Macedonia
3. Prof. Dr. Anita Grozdanov - Ss. Cyril and Methodius University - Macedonia
4. Prof. Dr. Asif Šabanović – International University of Sarajevo - Bosnia and Herzegovina
5. Prof. Dr. Christos Douligeris - University of Erlangen-Nurnberg - Germany
6. Prof. Dr. Dragutin T. Mihailović - University of Novi Sad - Serbia
7. Prof. Dr. Erkan Şahinkaya – İstanbul Medeniyet University - Turkey
8. Prof. Dr. Falko Dressler - University of Paderborn - Germany
9. Prof. Dr. Harry Miller – International University of Sarajevo - Bosnia and Herzegovina
10. Prof. Dr. Houssam Toutanji – Western Michigan University - USA
11. Prof. Dr. Ian F. Akyıldız – Georgia Institute of Technology - USA
12. Prof. Dr. İsmail Usta - Marmara University - Turkey
13. Prof. Dr. Liljana Gavrilovska - Ss Cyril and Methodius University - Macedonia
14. Prof. Dr. Lukman Thalib - Qatar University - Qatar
15. Prof. Dr. M. Asghar Fazel – University of Environment - Iran
16. Prof. Dr. Mehmet Akalin - Marmara University - Turkey
17. Prof. Dr. Mehmet Kitiş – Süleyman Demirel University - Turkey
18. Prof. Dr. Muammer Koç - Hamad bin Khalifa University - Qatar
19. Prof. Dr. Özer Çınar – Yıldız Technical University - Turkey
20. Prof. Dr. Perica Paunovik - Ss. Cyril and Methodius University - Macedonia
21. Prof. Dr. Rifat Škrijelj – University of Sarajevo - Bosnia and Herzegovina
22. Prof. Dr. Samir Đug - University of Sarajevo - Bosnia and Herzegovina
23. Prof. Dr. Tanju Karanfil – Clemson University - USA
24. Prof. Dr. Tibor Biro - National University of Public Service, Budapest - Hungary
25. Prof. Dr. Ümit Alver – Karadeniz Technical University - Turkey
26. Prof. Dr. Wolfgang Gerstaecker - University of Erlangen-Nurnberg - Germany
27. Prof. Dr. Yılmaz Yıldırım - Bülent Ecevit University - Turkey
28. Prof. Dr. Yousef Haik - Hamad bin Khalifa University - Qatar
29. Assoc. Prof. Dr. Alaa Al Hawari - Qatar University - Qatar
30. Assoc. Prof. Dr. Izudin Dzafic - International University of Sarajevo - Bosnia and Herzegovina
31. Assoc. Prof. Dr. Muhamed Hadziabdic - International University of Sarajevo - Bosnia and Herzegovina
32. Assoc. Prof. Dr. Nusret Drešković - University of Sarajevo - Bosnia and Herzegovina
33. Assist. Prof. Dr. Faruk Berat Akçeşme - International University of Sarajevo - Bosnia and Herzegovina
34. Assist. Prof. Dr. Fouzi Tabet - German Biomass Research Center - Germany
35. Assist. Prof. Dr. Haris Gavranovic - International University of Sarajevo - Bosnia and Herzegovina
36. Assist. Prof. Dr. Murat Karakaya - Atılım University - Turkey
37. Assist. Prof. Dr. Sasan Rabieh - Shahid Beheshti University - Iran
38. Assist. Prof. Dr. Ševkija Okerić - University of Sarajevo - Bosnia and Herzegovina
39. Dr. Hasan Bora Usluer - Galatasaray University - Turkey
40. Dr. Muhammet Uzun - RWTH Aachen University - Germany
41. Dr. Zsolt Hetesi - National University of Public Service, Budapest - Hungary
42. Dr. Zsolt T. Németh - National University of Public Service, Budapest - Hungary

ORGANIZATION COMMITTEE

Chairman(s) of the Conference

Prof. Dr. Özer Çınar – Yıldız Technical University

Members of the Committee

Prof. Dr. M. Asghar Fazel – University of Environment - Iran

Prof. Dr. Ümit Alver - Karadeniz Technial University - Turkey

Assoc. Prof. Dr. Lukman Thalib - Qatar University - Qatar

Assoc. Prof. Dr. Nusret Drešković - University of Sarajevo - Bosnia and Herzegovina

Assist. Prof. Dr. Sasan Rabieh - Shahid Beheshti University - Iran

Alma Ligata - Zenith Group - Bosnia and Herzegovina

Ismet Uzun - Zenith Group - Bosnia and Herzegovina

Musa Kose - Zenith Group - Bosnia and Herzegovina

WELCOME TO ICETI 2019

On behalf of the organizing committee, we are pleased to announce that the International Conference On Engineering Technology And Innovation is held from April 17-21, 2019 in Belgrade. ICETI 2019 provides an ideal academic platform for researchers to present the latest research findings and describe emerging technologies, and directions in Engineering Technology And Innovation. The conference seeks to contribute to presenting novel research results in all aspects of Engineering Technology And Innovation.

The conference aims to bring together leading academic scientists, researchers and research scholars to exchange and share their experiences and research results about all aspects of Engineering Technology And Innovation. It also provides the premier interdisciplinary forum for scientists, engineers, and practitioners to present their latest research results, ideas, developments, and applications in all areas of Engineering Technology And Innovation. The conference will bring together leading academic scientists, researchers and scholars in the domain of interest from around the world. ICETI 2019 is the oncoming event of the successful conference series focusing on Engineering Technology And Innovation.

The International Conference on Engineering Technology and Innovation (ICETI 2019) aims to bring together leading academic scientists, researchers and research scholars to exchange and share their experiences and research results about all aspects of Engineering Technology and Innovation. It also provides the premier interdisciplinary forum for scientists, engineers, and practitioners to present their latest research results, ideas, developments, and applications in all areas of Engineering Technology and Innovation. The conference will bring together leading academic scientists, researchers and scholars in the domain of interest from around the world. The conference's goals are to provide a scientific forum for all international prestige scholars around the world and enable the interactive exchange of state-of-the-art knowledge. The conference will focus on evidence-based benefits proven in technology and innovation and engineering experiments.

Best regards,

Prof. Dr.Özer ÇINAR



CONTENT	COUNTRY	PAGE
Improving the Measurement Procedure of Qubit-Based Sensor via Feedback Control Algorithms	Turkey	1
Effectiveness of a Cycloidal Pulse Model for Evaluating Isolation Systems of Buildings with LRBs Considering Heating Effects	Turkey	9
Effect of Accidental Eccentricity on the Isolation System Responses of Cylindrical Liquid Storage Tanks	Turkey	14
The Benefits and Challenges of On-Site 3D-Printed Construction: A Case Study	USA	21
Earing Prediction of a Cup Drawing Process Based on the Quadratic Hill Yield Function	Turkey	30
The Metrics to Measure and Evaluate Software Developers' Performance	Turkey	39
EMIC: An Ensemble Approach for Improving Multi-Instance Classification	Turkey	45
Response Surface Method for Optimization of Suspension Ball Joint Pull Out Force by Using Ansys	Turkey	52
The Pure Bending Fatigue Behaviour Of The Heavily Drawn Steel Filaments	Turkey	60
The Fatigue Crack Propagation Of The Heavily Drawn Steel Cord Filaments	Turkey	64
Optimization of Parameters of Tuned Mass Dampers by Using Hybrid Metaheuristic Algorithms	Turkey	68
Optimum Design of T-Beams Using Jaya Algorithm	Turkey	75
Antifouling PEBA Membranes for Biobutanol Recovery by Pervaporation	Turkey	81
Systems of Systems: The Innovation phase - How are they born?	Israel	88



Improving the Measurement Procedure of Qubit-Based Sensor via Feedback Control Algorithms

Sergey Borisenok¹

Abstract

The extreme sensitivity of quantum systems towards the external perturbations and their ability to be strongly coupled to the measured target field makes them to be stable under the environmental noise. A high quality quantum sensor can be engineered even on the platform of a single trapped qubit.

Different measurement procedures, like Jachymski - Wasak - Idziaszek (JWI) measurement protocol proposed in 2018, have been developed experimentally for qubit-based quantum sensors. In JWI sensing the particles pass through 1D waveguides containing confined ultracold atoms (trapped measuring qubits). The probability for transmission or reflection of the colliding particles depends strongly on the total external field strength.

For the JWI sensing procedure we developed a control algorithm for measuring qubits. The external field defining the effectiveness of the JWI measurement acts for the given qubit as a set of quantum operators changing their properties in time. For that reason we involve here completely novel object, the universal dynamical quantum gate, Switching from one logical operation to another dynamically but not in the sequence of different static logical gates can optimize the efficiency of quantum algorithm and minimize the negative effect of decoherence.

We applied this concept to improve the sensor performance based on the set of parameters, including the operational fidelity and the quantum Fisher parameter that defines a lower bound of uncertainty of the inferred value for the measured external field.

We check different alternative optimal and sub-optimal feedback control algorithms to compare their pros and cons. Here we present our results for a single qubit without the distinct decay due to its weak coupling to the environment and discuss the perspectives for the development of our approach.

Keywords: quantum sensors, control algorithms, feedback tracking

1. INTRODUCTION: QUANTUM SENSORS

In the last three years we observe a distinct progress in different engineering applications of quantum systems trapped by the specific shapes of potentials and interacting with static impurities. Such systems are used for the purpose of quantum computation, quantum simulations of many-body physics and for development of precise quantum analyzers and sensors. A high quality quantum sensor can be engineered even on the **platform of a single trapped qubit** [1-4]. The extreme sensitivity of quantum systems towards the external perturbations and in the same time their ability to be strongly coupled to the measured target field makes them to be stable under the environmental noise [5].

1.1. Single Qubit-Based Sensors

The experimental technique for controlled trapped ions, photons and superconducting circuits reached the point where few tens of qubits can be manipulated with high quantum gate fidelities involves the algorithms for quantum error correction [6]. Physicists developed different measurement protocols for qubit-based quantum

¹Corresponding author: Abdullah Gül University, Faculty of Engineering, Department of Electrical and Electronics Engineering, 38080, Kocasinan/Kayseri, Turkey. sergey.borisenok@agu.edu.tr



sensors. One of them, *Jachymski - Wasak - Idziaszek (JWI) measurement protocol* [7], is drawn on Fig. 1 (left).

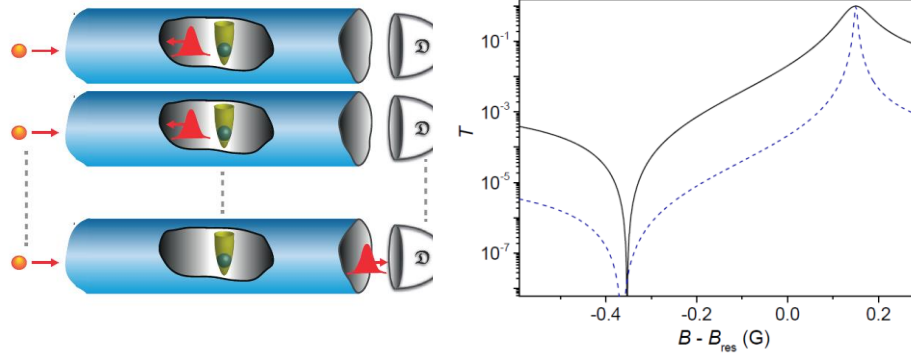


Figure 1. Comparison of single qubit-based sensor protocols. **Left:** *Jachymski - Wasak - Idziaszek measurement protocol*. **Right:** Transmission coefficient T as a function of the magnetic field B for Cs atoms in a static harmonic trap with $\Delta = 0.15$ G. The dashed line shows corresponds to very low longitudinal momentum (about 0.1 nK), the solid line corresponds to 15 nK [7].

On Fig.1a N atoms (red spheres on the left) are sent through N quasi-one dimensional waveguides (the tubes in the picture). In each waveguide a tightly confined impurity atom (green sphere) is placed. The colliding atoms (red wavepackets) can be either transmitted or reflected with probability depending on the total external field strength.

The trapped atoms in JWI approach have been scattered in quasi-1D geometry, while the impurity atoms with the mass m were pinned by the trap. The system has been described by the Schrodinger equation [7]:

$$\left[-\frac{\hbar^2}{2m} \nabla^2 + U(\mathbf{r}) + V_{\text{tr}}(\mathbf{r}) \right] \Psi(\mathbf{r}) = E\Psi(\mathbf{r}), \quad (1)$$

where the potential U stands for the measured field interacting with the qubits together with the inter-qubit interactions (the interparticle interaction was considered to be weak). In [7] the trapping potential V_{tr} was harmonic, such that the Schrodinger Eq. (1) was stationary; we use it here as a control parameter and consider to work with a Lindblad-type equation in the place of (1). The measurement is based on the fact that the energy-depending scattering length a depends on the measured external magnetic field B as $a = a_{\text{bg}} [1 - \Delta / (B - B_{\text{res}})]$, where B_{res} is the Feshbach resonance magnitude, a_{bg} is the background scattering length away from the resonance, and Δ stands for the resonance width. This scattering length a is included into the **transmission coefficient** T , presented on Fig. 1 (right) for the case of a static quasi-1D harmonic trap.

1.2. Algorithms for Quantum Control

Control algorithms applied to quantum systems vary from measurement-based to coherent, and from feedforward (open-loop) to feedback approaches: feedforward control based on off-resonance pulses [8]; linear current-regulating feedback, including delay [9], time-delayed coherent linear feedback control of a two-level atom [10].

The method of **quantum filtering**, that uses the results of continuous weak measurements to control the behavior of quantum mechanical devices via recursive filtering in diffusive quantum stochastic master equations, also demonstrates very high robustness [11]. Quantum filtering algorithm for a non-Markovian single qubit driven by white noise has been developed in [12].



Among all control approaches the *optimal and sub-optimal (locally optimal) control methods* seem to be the most appropriate for tracking sensing qubits. Optimal control in an open dissipative system is the method of choice to govern quantum systems within subspaces of weak relaxation whenever the drift Hamiltonian would otherwise drive the system through fast decaying modes [13]. Optimal control was applied to a model system of interacting two-level particles (e.g., spin-half atomic nuclei or electrons or two-level atoms) to produce high-fidelity quantum gates while simultaneously negating the detrimental effect of decoherence [14]. For one-qubit quantum sensing optimal control has been discussed in [15].

Speed gradient (SG) method has been applied to two-level quantum system (with or without a distinct dissipation) driven by external classical field [16], by the combination of quantum coherent and incoherent control [17] for stabilization.

2. CONTROL MODEL FOR IMPROVING THE MEASUREMENT PROCEDURE

The application of *control methods* to quantum systems has analog with the classical control approach but in the same time possesses some features [18]. Such a correspondence provides a natural basement for the transferring of control algorithms designed for stabilization and tracking in classical systems into the set of quantum problems.

2.1. Basic Model

The *basic model* for the measuring elements considers a qubit, two-level quantum system, attached to a quantum bath [17]. The Lindblad dynamical equation for density operator is given by:

$$\frac{d\rho}{dt} = -i[H_0 + u(t)V, \rho] + \gamma[(n(t) + 1)L_{12}(\rho) + n(t)L_{21}(\rho)], \quad (2)$$

with Einstein coefficient $\gamma > 1$ for the transition between two states 1 ('the ground level') and 2 ('the excited level'); and the Lindblad operators:

$$L_{12}(\rho) = 2\rho_{22}P_1 - P_2\rho - \rho P_2 \quad ; \quad L_{21}(\rho) = 2\rho_{11}P_2 - P_1\rho - \rho P_1 \quad . \quad (3)$$

We consider in (3) control by spectral density of incoherent radiation $n(t)$ (as a non-negative function) and the coherent part $u(t)$. The coherent part includes the interaction with the measured external field.

2.2. Feedback Control Methods

Among the wide spectrum of control algorithms (quantum filtering, spectral zone control, differential evolution and others) we chose here the family of Pontryagin-type sub-optimal (locally optimal) Fradkov's *speed gradient (SG)* [19] and Kolesnikov's *target attractor (TA)* feedback [20].

Speed gradient (SG) algorithm is based on the definition of the scalar *goal (target) function* [19], that for the case of an arbitrary dynamical control parameter $F(t)$ can be presented in the form:

$$G = \frac{1}{2}[F(t) - F_*(t)]^2. \quad (4)$$

Here $F(t)$ is the actual parameter, and $F_*(t)$ is the target that has a shape of smooth differentiable function. The goal of feedback control is achieved when the target function G tends to zero. The specific target (4) observing the goal membrane potential F_* as a time-dependent function is called *tracking*.

Let's take now the time derivative of (4):

$$\Omega = \frac{dG}{dt} = (F - F_*) \left[\frac{dF}{dt} - \frac{dF_*}{dt} \right]. \quad (5)$$

The derivative dF/dt contains the control signals through the dynamical equations of the corresponding system (3):

$$\frac{d}{dt} [u + \Psi(u)] = -\Gamma \nabla_u \Omega \quad . \quad (6)$$



Here Γ is a positive constant, and the function $\Psi(u)$ satisfies the pseudogradient condition:

$$\Psi(u) \cdot \nabla_u \Omega \geq 0. \quad (7)$$

Target attractor (TA) algorithm (“synergetic control” in author’s terminology) is based on the “directed self-organization of the dynamical system” [20]. The m -parametric attracting invariant manifold (the subset referring the control target)

$$G_s(x_1, \dots, x_n) = 0; \quad s = 1..m \quad (8)$$

is defined as a functions of the state variables x_1, \dots, x_n . Eqs (8) provide the asymptotic stability of the system dynamics with respect to the control goal. To do it, let’s require:

$$T_s \frac{dG_s(t)}{dt} + G_s(t) = 0. \quad (9)$$

where T_s are positive constants, i.e. time scales. Tending to zeros exponentially, the goal functions (8) lead the dynamical evolution of the system to the target attractor. For the tracking we consider these functions in the form:

$$G(t) = F(t) - F_*(t). \quad (10)$$

2.3. Multi-Goal Dynamical Formulation of the Algorithm

Our **complex algorithmic approach** for the improvement of the quantum sensor efficiency can be presented as two basic stages:

- 1) **The preparation of the sensor.** This stage includes both the control over the qubit energies (cooling) and over the qubit locations (trapping). This control is performed via the appropriate design of the external field which traps the elements of the sensor and in the same time manages their interaction with the environment.
- 2) **Measuring protocol of the sensor.** At this stage the additional dynamical control field serves for improving the sensitivity of the sensor and additionally it must consider an algorithm of an error corrections coming from impurity of the desired sensing qubit states and from the decay interaction of these elements with the environment during the process of measurement.

The important feature of both algorithms, SG and TA, is that they could be easily extended to **multi-goal formulation**, when the tracking is performing for the dynamical weighted set of few goal functions summed with weights.

$$G(t) = w_1(t)G_1(t) + w_2(t)G_2(t) + \dots; \quad w_1(t) + w_2(t) + \dots = 1. \quad (11)$$

The multi-goal dynamical formulation of the control goal function covering sequent in time the preparation of the sensor measuring qubits and the measurement procedure itself: the goal function must include the control over the qubit energies and their interaction with the noisy environment, their spatial distribution, control over the measuring protocol characteristics and the sensor performance (fidelity, Fisher parameter), with the priorities of the particular control goals changing in time. The weights $w_k(t)$ will specify the stage of the sensor working cycle, switching the priority of the target from the preparation to measuring. Each particular control goal $G_k(t)$ will be chosen in the form (4) for SG or, alternatively, (10) for TA algorithms.

3. PREPARATION OF THE QUBIT-BASED SENSOR

Combining two models for cooling and focusing the measuring qubits, we can prepare the sensor for the measurement of the external field.

3.1. Control over the Qubit Energy

To prepare qubits for the measurement procedure we need to cool them down. Thus, the goal function G_E for this part will be presented via the qubit energy stabilizing at some certain level of cooling.



For SG approach it has been already investigated in [17] for a single qubit without the coherent component. In this case the goal function (4) is defined through the qubit energy E , and the target constant energy E_* must be much below the initial $E(0)$:

$$G_E = \frac{1}{2} [E(t) - E_*]^2. \quad (12)$$

Together with (3) that implies (Pechen, Borisenok, 2015) for the incoherent control field:

$$n = 4\gamma\Gamma(E - E_*) \left(E - \frac{\omega}{2} \right). \quad (13)$$

Here $\omega = E_2 - E_1$, is the energy interval between two quantum levels of the qubit, the Plank constant is chosen to be 1. The result of cooling is represented in dimensionless form on Fig. 2. The set of dimensionless variables is given by: $\tilde{\Gamma} = 4\gamma\Gamma E_*^2$, $r = \omega/2E_*$, and $x = E/E_*$.

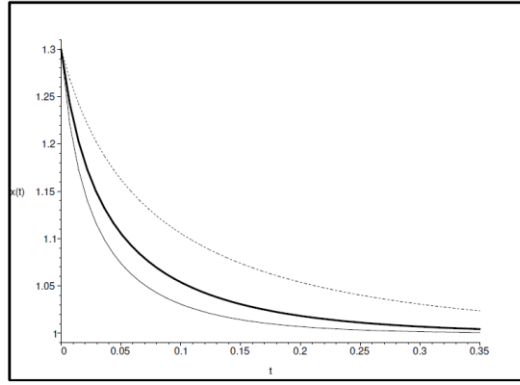


Figure 2. Cooling with the speed gradient algorithm (13) for $\tilde{\Gamma} = 5$ (solid thin line), $\tilde{\Gamma} = 10$ (solid thick line), and $\tilde{\Gamma} = 15$ (dashdot line). Other parameters are: $\gamma = 2$, $r = 2/3$, the initial condition is $x(0) = 1.3$.

3.2. Trapping Spatial Control

This part is based on the statistical approach [21] for an *ensemble* of N particles. In our case they are qubits trapped in the external potential in the frame of JWI protocol. Let's define the *density function* ρ with the condition: $dP = \rho dx$, where dP is the probability to find a particle in the small volume dx of the state vector \mathbb{R}^n -space. The density function is normalized: $\int \rho(x) dx = 1$ (with integration over all the possible x). The average of some space-dependent variable $A(x)$ should be defined in this case as: $\bar{A}(x) \equiv \int A(x) \rho(x) dx$ due to the normalization. For the trapped particles we can involve:

$$\rho(x, t) = \frac{1}{N} \sum_{\alpha=1}^N \delta_{\{n\}}(x(t) - x^{(\alpha)}(t)), \quad (14)$$

$\alpha = 1, \dots, N$ and $x^{(\alpha)} \equiv (x_1^{(\alpha)}, x_2^{(\alpha)}, \dots, x_n^{(\alpha)})^T$ is the vector for the α -th particle. The Dirac n -dimensional delta-function $\delta_{\{n\}}(x)$ is defined as a product of one-dimensional delta-functions $\delta(x_\beta)$:



$$\delta_{\{n\}}(x) \equiv \prod_{\beta=1}^n \delta(x_{\beta}). \quad (15)$$

With ρ_0 we denote the initial distribution function, and with ρ_* - the target one. The SG goal function (4) in such a case can be chosen as:

$$G_T \equiv \frac{1}{2}(\rho - \rho_*)^2 ; \quad \rho(x) = \frac{1}{N} \sum_{\alpha=1}^N \prod_{\beta=1}^n \delta(x_{\beta} - x_{\beta}^{(\alpha)}). \quad (16)$$

The similar approach can be performed for TA algorithm.

4. CONTROLLED MEASURING PROTOCOL FOR THE QUANTUM SENSOR

For improving the measuring protocol of the sensor we plan to control few parameters for each qubit. First of all, the part of the external field defining the effective measurement procedure acts for the given qubit as a set of quantum operators changing their properties in time. For that reason we involve here completely novel object, the universal dynamical quantum gate.

4.1. Control over Fidelity

The external field driven the given qubit can be presented as a dynamical quantum gate, and to increase the sensor efficiency one should improve its *fidelity* [22]; it also must be adopted to the dynamical model of quantum sensors [23]. The average gate fidelity (AGF) is defined through the integration over all pure states in the system as [24]:

$$F_{\text{avg}} = \int d|\psi\rangle\langle\psi| D(|\psi\rangle\langle\psi|) |\psi\rangle, \quad (17)$$

with the channel discrepancy D (that is equal to unity for an ideal channel). By the definition of (17) AGF is bounded by the interval [0,1]. The fidelity also can be expressed via the diamond distance [25]:

$$\eta_{\diamond} = \frac{1}{2} \|D - I\|_{\diamond}, \quad (18)$$

and it is bounded by $\eta_{\diamond}^{\text{Pauli}} \leq \eta_{\diamond} \leq \eta_{\diamond}^{\text{ub}}$, with the Pauli and upper bounds: $\eta_{\diamond}^{\text{Pauli}} = (d+1)(1 - F_{\text{avg}})/d$; $\eta_{\diamond}^{\text{ub}} = \sqrt{d(d+1)(1 - F_{\text{avg}})}$. The dimension of the computational subspace d is equal to: $d = 2^N$, where N stands for the number of qubits.

The diamond distance can be efficiently used as a goal parameter to improve the fidelity of a quantum operation over the driven qubit.

4.2. Control over the Sensor Performance via the Fisher Parameter

The performance of the quantum sensor measurement is based on the quantum analog [26] of the classical Cramér-Rao lower bound (CRLB) theorem. CRLB defines a lower bound of uncertainty of the inferred value ΔB of the measured parameter [26]:

$$(\Delta B)^2 \geq \frac{1}{NF}. \quad (19)$$

Here N stands for the numbers of measuring elements (qubits in our case). The parameter F is the quantum analog of classical Fisher information, for the Jachymski-Wasak-Idziaszek measurement protocol and other similar types of sensors it is given by [7]:

$$F = \sum_s \frac{1}{P(s|B)} \cdot \left(\frac{\partial P(s|B)}{\partial B} \right)^2, \quad (20)$$



where the summation is made over the full set $\{s\}$ of quantum states, and $P(s|B)$ are the probabilities to get the corresponding state s under the action of the external field B . Thus, the maximization of the Fisher parameter F minimizes the lower bound of the uncertainty (19).

Let us show here the example for one sensing qubit driven via Kolesnikov's target attractor (TA) feedback [27]. If we consider again a non-decaying qubit over the Bloch sphere, its inversion $x = \rho_{22} - \rho_{11}$ defines the qubit state, because in the absence of decay: $\rho_{11} + \rho_{22} = 1$ and therefore $\rho_{11} = (1-x)/2$, $\rho_{22} = (1+x)/2$. That implies for Eq.(20):

$$F = \frac{1}{\rho_{11}} \left(\frac{\partial \rho_{11}}{\partial u} \right)^2 + \frac{1}{\rho_{22}} \left(\frac{\partial \rho_{22}}{\partial u} \right)^2 = \frac{1}{1-x^2} \left(\frac{\partial x}{\partial u} \right)^2. \quad (21)$$

(We remind that dimensionless $u(t)$ stands here for the total external field.) The Fisher parameter F becomes infinite under two natural limits: $x = \pm 1$, which correspond to two pure states of the qubit (the pure ground and the pure excited states), where the uncertainty is zero by (19).

Let's demonstrate now Kolesnikov's target attractor algorithm $dG_F / dt = -G_F / T$ to track the control goal to zero:

$$G_F = \left(\frac{\partial u}{\partial x} \right)^2 \rightarrow 0. \quad (22)$$

Let's consider two components of the external field: $u = u_m + u_c$, where u_m is a measured part and u_c is a control signal. Then the tracking algorithm is given by:

$$u_c(t) = u_m(0)e^{-t/2T} - u_m(t). \quad (23)$$

Thus, the TA feedback tracks the measured field $u_m(t)$ as a dynamical function and drives the additional control field $u_c(t)$ to minimize the uncertainty (19).

5. CONCLUSIONS

The improvement of the trapped qubit-base sensor performance at all stages of the measuring protocol demands the development of a novel control algorithmic approach. An efficient model tool for qubit-based quantum measurement will stimulate the development of corresponding experimental approaches for different physical realizations of quantum sensors;

The multi-goal dynamical formulation of the control goal function covers sequentially in time the preparation of the sensor measuring qubits and the measurement procedure itself: the goal function must include the control over the qubit energies and their interaction with the noisy environment, their spatial distribution, control over the measuring protocol characteristics and the sensor performance (fidelity, Fisher parameter), with the priorities of the particular control goals changing in time.

The development and investigation (for each particular control goal) few alternative control algorithms based on speed gradient or target attractor approaches improves the algorithm from the point of their efficiency, robustness and calculability, and as a finalization, development of detailed feedback control algorithms specifically for each particular control goal. The verification of the finalized complex multi-goal control algorithm in the frame of the theoretical model should be provided comparison of the analytical and numerical results with the experimental data described in the literature.

ACKNOWLEDGMENT

The author thanks Prof. Dr. Alexander Fradkov (Russia) for research collaboration, productive discussions and valuable remarks.



REFERENCES

- [1]. C. L. Degen, F. Reinhard, P. Cappellaro, "Quantum Sensing", *Rev. Mod. Phys.*, vol. 89, p. 035002, 2017.
- [2]. P. Sekatski, M. Skotiniotis, W. Dur, "Improved Sensing with a Single Qubit", *Phys. Rev. Lett.*, vol. 118, p. 170801, 2017.
- [3]. S. Danilin, A. V. Lebedev, A. Vepsäläinen, G. B. Lesovik, G. Blatter, G. S. Paraoanu, "Quantum-enhanced Magnetometry by Phase Estimation Algorithms with a Single Artificial Atom", *Quantum Information*, vol. 4, p. 29, 2018.
- [4]. Y. Matsuzaki, S. Benjamin, S. Nakayama, S. Saito, W. J. Munro, "Quantum Metrology Beyond the Classical Limit Under the Effect of Dephasing", *Phys. Rev. Lett.*, vol. 120, p. 140501, 2018.
- [5]. L. M. Norris, D. Lucarelli, V. M. Frey, S. Mavadia, M. J. Biercuk, L. Viola, "Optimally Band-Limited Spectroscopy of Control Noise Using a Qubit Sensor", *Phys. Rev. A*, vol. 98, p. 032315, 2018.
- [6]. A. Morello, "What Would You Do with 1000 Qubits?", *Quantum Sci. Technol.*, vol. 3, p. 030201, 2018.
- [7]. K. Jachymski, T. Wasak, Z. Idziaszek, "Single-Atom Transistor as a Precise Magnetic Field Sensor", *Phys. Rev. Lett.*, vol. 120, p. 013401, 2018.
- [8]. S. Ashhab, S. Matsuo, N. Hatakenaka, F. Nori, "Generalized Switchable Coupling for Superconducting Qubits Using Double Resonance", *Phys. Rev. B*, vol. 74, p. 184504, 2006.
- [9]. T. Brandes, "Feedback Control of Quantum Transport", *Phys. Rev. Lett.*, vol. 105, p. 060602, 2010.
- [10]. A. L. Grimsmo, "Time-Delayed Quantum Feedback Control", *Phys. Rev. Lett.*, vol. 115, p. 060402, 2015.
- [11]. P. Rouchon, J. F. Ralph, "Efficient Quantum Filtering for Quantum Feedback Control", *Phys. Rev. A*, vol. 91, p. 012118, 2015.
- [12]. S. Xue, M. R. James, A. Shabani, V. Ugrinovskii, I. R. Petersen, "Quantum Filter for a Non-Markovian Single Qubit System", in *Proc. 2015 IEEE Conference on Control Applications (CCA)*, 2015, pp. 19-23.
- [13]. T. Schulte-Herbrueggen, A. Spoerl, N. Khaneja, S. J. Glaser, "Optimal Control for Generating Quantum Gates in Open Dissipative Systems", *J. Phys. B*, vol. 44, p. 154013, 2011.
- [14]. M. Grace, C. Brif, H. Rabitz, I. A. Walmsley, R. L. Kosut, D. A. Lidar, "Optimal Control of Quantum Gates and Suppression of Decoherence in a System of Interacting Two-Level Particles", *J. Phys. B*, vol. 40, pp. S103-S125, 2007.
- [15]. F. Poggiali, P. Cappellaro, N. Fabbri, "Optimal Control for One-Qubit Quantum Sensing", *Phys. Rev. X*, vol. 8, p. 021059, 2018.
- [16]. S. Borisenok, A. Fradkov, A. Proskurnikov, "Speed Gradient Control of Qubit State", *Periodic Control Systems*, vol. 4, pp. 81-86, 2010.
- [17]. A. N. Pechen, S. Borisenok, "Energy Transfer in Two-Level Quantum Systems via Speed Gradient-Based Algorithm", *IFAC-PapersOnLine*, vol. 48-11, pp. 446-450, 2015.
- [18]. J. M. Geremia, *An Introduction to Control Theory from Classical to Quantum Applications*, Heidelberg: Ruprecht-Karls-Universität, 2003.
- [19]. A. L. Fradkov, *Cybernetical Physics: From Control of Chaos to Quantum Control*, Berlin, Heidelberg: Springer, 2007.
- [20]. A. Kolesnikov, *Synergetic Control Methods for Complex Systems*, Moscow: URSS Publ., 2012.
- [21]. S. Borisenok, "Statistical Space Control in Non-Linear Systems: Speed Gradient Method", *Journal of Prime Research in Mathematics*, vol. 1, pp. 145-155, 2005.
- [22]. C. A. Fuchs, C. M. Caves, "Ensemble-Dependent Bounds for Accessible Information in Quantum Mechanics", *Phys. Rev. Lett.*, vol. 73, p. 3047, 1994.
- [23]. D. P. L. Aude Craik, N. M. Linke, M. A. Sepiol, T. P. Harty, J. F. Goodwin, C. J. Balance, D. N. Stacey, A. M. Steane, D. M. Lucas, D. T. C. Allcock, "High-Fidelity Spatial and Polarization Addressing of Ca-43 Qubits Using Near-Field Microwave Control", *Phys. Rev. A*, vol. 95, p. 022337, 2017.
- [24]. D. Willsch, M. Nocon, F. Jin, H. De Raedt, K. Michielsen, "Gate-Error Analysis in Simulations of Quantum Computers with Transmon Qubits", *Phys. Rev. A*, vol. 96, p. 062302, 2017.
- [25]. Y. R. Sanders, J. J. Wallman, B. C. Sanders, "Bounding Quantum Gate Error Rate Based on Reported Average Fidelity", *New J. Phys.*, vol. 18, p. 012002, 2016.
- [26]. P. Refregier, *Noise Theory and Application to Physics: From Fluctuations to Information*, New York: Springer Science & Business Media, 2012.
- [27]. S. Borisenok, "Control over Performance of Qubit-Based Sensors", *Cybernetics and Physics*, vol. 7, pp. 93-95, 2018.



Effectiveness of a Cycloidal Pulse Model for Evaluating Isolation Systems of Buildings with LRBs Considering Heating Effects

Zafer Kanbir¹, Seda Oncu-Davas¹, Hatice Gazi¹, Cenk Alhan²

Abstract

Seismic isolation systems which are used to mitigate the harmful effects of earthquakes on structures can protect structural and non-structural elements and even vibration-sensitive contents. However, they are challenged by the pulse-like near-fault earthquakes containing long-period large-velocity pulses which may cause excessive isolator displacements. Furthermore, the lead core heating in lead rubber bearings (LRBs) leads to decrease in the characteristic strength and consequently notable increase in base displacement especially under pulse-like near-fault earthquakes. This phenomenon raised the interest of researchers on the performance of seismically isolated buildings with LRBs under such earthquakes. Because of the scarcity of historical pulse-like near-fault earthquake records, synthetic pulse models that can approximately represent these records have been developed by various researchers for conducting comprehensive parametric studies. Among these, the half-cycle forward cycloidal pulse model, Type-A [N. Makris, "Rigidity-plasticity-viscosity: can electrorheological dampers protect base-isolated structures from near-source ground motions?", *Earthquake Engineering and Structural Dynamics*, vol. 26, pp. 571-592, 1997] is used in various research studies because of its analytical simplicity. In this study, the capability of this model in representing actual pulse-like near-fault earthquake records in terms of the isolation system response is investigated in the context of a benchmark 4-story seismically isolated building subjected to a historical pulse-like near-fault earthquake record and its synthetically generated counterpart Type-A cycloidal pulse model, when lead core heating is considered. Base displacement time histories and force-displacement hysteretic curves of LRBs demonstrate the success of Type-A cycloidal pulse model.

Keywords: Seismic isolation; near-fault earthquake; ground motion pulse model; lead rubber bearing, lead core heating.

1. INTRODUCTION

Seismic isolation systems are used to mitigate the harmful effects of earthquakes on structures. Both structural and non-structural elements and even vibration-sensitive contents can be protected by these systems which are composed of laterally flexible isolation elements that elongate the natural period of the building. By this way, the accelerations sustained by the structure and its contents are reduced significantly. Furthermore, the energy input into the structure is also reduced as the energy input at the foundation level is primarily dissipated at the isolation system level by the damping resulting from the hysteretic behavior of the isolators. These systems have proven to be successful under typical far-fault earthquakes but they are challenged by the near-fault earthquakes containing long-period large-velocity pulses that may cause excessive isolator displacements which may consequently pose a threat on the structural integrity [1], [2]. This issue becomes even more problematic due to the lead core heating in lead rubber bearings (LRBs) which may be particularly high in case of near-fault earthquakes [3] since it leads to decrease in the characteristic strength and consequently notable increase in the base displacement [4], [5]. As a result, the interest in evaluating the seismic performance of seismically isolated buildings which employ LRBs under pulse-like near-fault earthquakes has increased in recent years [6], [7]. In order to conduct parametric studies in this area, a large number of pulse-like earthquake

¹ Istanbul University-Cerrahpaşa, Department of Civil Engineering, 34320, Avcılar/Istanbul, Turkey.
zafirkanbir@istanbul.edu.tr, seda.oncu@istanbul.edu.tr, hgazi@istanbul.edu.tr

² Corresponding author: Istanbul University-Cerrahpaşa, Department of Civil Engineering, 34320, Avcılar/Istanbul, Turkey. cenkalhan@istanbul.edu.tr



records would be needed. However, such records are not easy to find. Because of the scarcity of historical pulse-like near-fault earthquake records, synthetic pulse models that can approximately represent these records have been developed by various researchers [8]- [11]. On the other hand, the accuracy of the results obtained from studies using pulse models depends on how well these models represent the effects of the actual near-fault earthquakes on the structures. This issue was previously investigated in case of seismically isolated buildings [12], [13] and seismically isolated liquid storage tanks [14]. However, none of these studies considered the lead core heating effects. Among the aforementioned pulse models, the cycloidal Type-A pulse model proposed by Makris [8] is used in previous research studies as it possesses a simple analytical representation. In this study, the capability of this model in representing actual pulse-like near-fault earthquake records in terms of the isolation system response of seismically isolated buildings is investigated when lead core heating in LRBs is taken into account. For this purpose, the nonlinear time-history analyses of a benchmark 4-story seismically isolated building are conducted under a representative historical pulse-like earthquake record and its synthetically generated counterpart Type-A cycloidal pulse model [8] via OpenSees Program [15] and base displacement time histories and force-displacement hysteretic curves of LRBs are presented in a comparative fashion.

2. NUMERICAL MODELING

2.1. Structural Model

The superstructure considered here is a 4-story benchmark base-isolated building which consists of moment resisting reinforced concrete frames [16]. In each direction, there are four bays with a bay width of 5.00 m. Columns and beams have 30×50 cm and 45×45 cm rectangular cross-sections, respectively. The floor heights are 3.00 m and the total height of the building is 12.00 m. The total mass of the building, including the isolation basement, is 2000 tons and the mass of each floor is assumed to be lumped at the center of gravity. The lumped-mass model of the subject base-isolated building is given in Fig. 1. The isolation system consists of 25 identical bearings which are connected to each other with a rigid base [3]. In order to model the building considering lead core heating, the bearings have to be defined with their geometric dimensions and material properties. The detailed information about the LRBs designed with physical and material properties can be found in Kanbir et. al. [3].

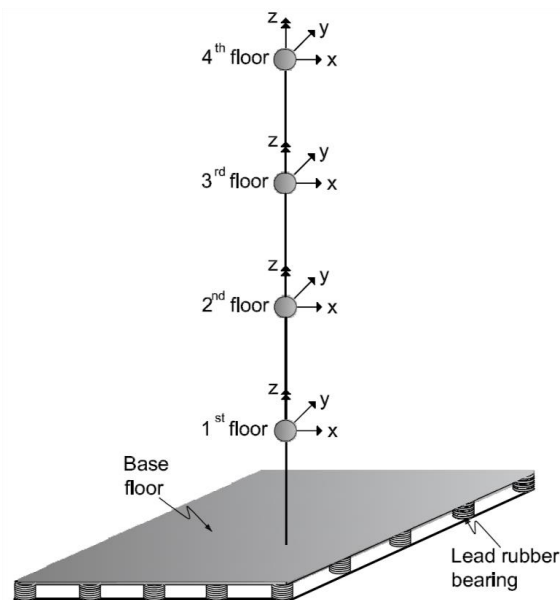


Figure 1. Lumped-mass model of the structure



According to the mathematical model proposed by Kalpakidis and Constantinou [4], which is utilized in this study to consider the temperature-dependent behavior of LRBs, the yield stress of lead, σ_{YL} degrades as the temperature of the lead core increases. The instantaneous yield stress is defined as $\sigma_{YL} = \sigma_{YL0} \exp(-E_2 \times T_L)$ where σ_{YL0} is the initial yield stress of lead which is 10 MPa. E_2 is a constant which is given as $0.0069/^\circ\text{C}$ and T_L is the increase in the lead core temperature with respect to the initial temperature. T_L is found in Kalpakidis and Constantinou [4] which accepts input parameters including the radius of lead, the height of lead core, the time since the beginning of the motion, the dimensionless time, and the material properties including the density of lead = 11200 kg/m^3 , the specific heat of lead = $130 \text{ J/(kg}^\circ\text{C)}$, the thermal conductivity of steel = $50 \text{ W/(m}^\circ\text{C)}$, and the thermal diffusivity of steel = $1.41 \times 10^{-5} \text{ m}^2/\text{s}$.

2.2. Earthquake Record - Cycloidal Pulse Model

Rupture directivity effects of stress waves propagating in the same direction as the fault rupture at a velocity close to the shear wave velocity cause pulse motions in the direction normal to the fault [8]. Therefore, the ground motions recorded in close proximity to the fault rupture (0 – 20 km), namely near-fault ground motions, generally contain long period velocity pulses with high amplitudes and permanent ground displacements [17]. Thanks to those pulses, near-fault ground motions with rupture directivity effects generally have simple geometric structure and can be simulated synthetically by simple pulse models [18]. Several pulse models were proposed in the literature [8]- [11]. Among these, half-cycle forward velocity pulse model, which is denoted as Type-A, is developed by Makris [8] and is used in this study. The velocity time history function, $\dot{u}(t)$, of this pulse model is given in Eq. 1. It is valid for the time interval $0 \leq t \leq T_p$ and V_p and T_p are the velocity and the period of the pulse, respectively.

$$\dot{u}(t) = (V_p/2) - (V_p/2) \cos\left((2\pi/T_p)t\right) \quad (1)$$

In this study, the RRS228 component of the 1994 Northridge Earthquake recorded at the Rinaldi Receiving Station located at a distance of 7.10 km from the fault line is used as the representative recorded near-fault ground motion with long-period and large-velocity pulses. The velocity time history of the recorded ground motion is obtained from PEER Strong Ground Motion Database [19] and is given in Fig. 2 in a comparative fashion with its synthetic counterpart which is generated using Makris Type-A pulse model [8]. As given in this figure, the peak ground velocity of RRS228 is 166.10 cm/s. The peak ground acceleration and the peak ground displacement are equal to, 0.838g and 28.20 cm, respectively. The synthetic pulse model parameters, i.e. the pulse period and the pulse velocity, are obtained from Makris and Chang [9] as $T_p = 0.8 \text{ s}$ and $V_p = 175 \text{ cm/s}$.

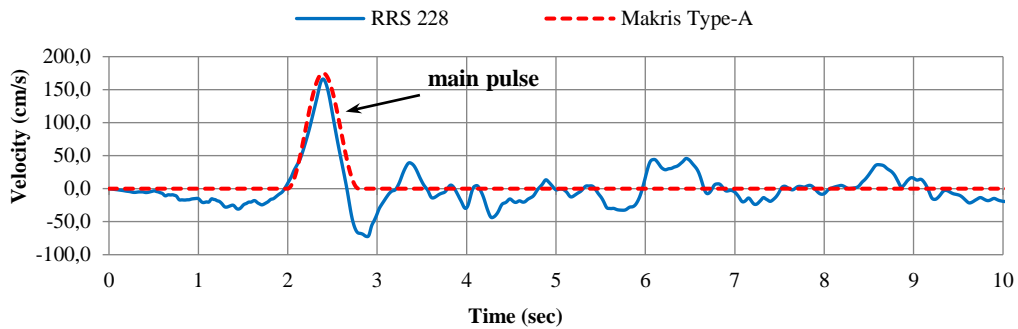


Figure 2. Velocity time histories of RRS 228 record and its counterpart Makris Type-A [8] cycloidal pulse model

3. DISCUSSION OF RESULTS

The base-isolated reinforced concrete building described in Section 2.1 is modeled in OpenSees Program [15] considering the temperature-dependent behavior of LRBs and nonlinear time history analyses are carried out under RRS228 record and its synthetic counterpart Type-A pulse model. In order to demonstrate the capability of Type-A cycloidal pulse model in representing the near-fault pulse-like RRS228 record in terms of the



isolation system response when lead core heating in LRBs is of concern, the base displacement time history plots and force-displacement hysteretic curves of LRBs are reported in a comparative manner in this section.

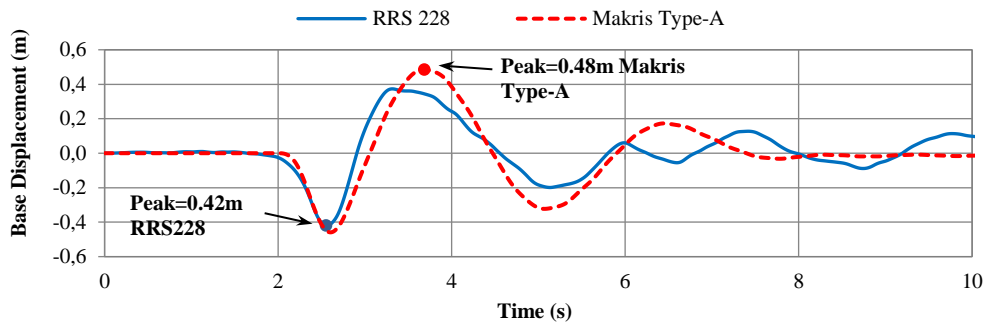


Figure 3. Base displacement response histories

It can be seen in base displacement time histories presented in Fig. 3 that Type-A cycloidal pulse model captures the overall seismic behavior except for some discrepancies observed in particular out of the main pulse region. The observed peak displacements are 0.42 m and 0.48 m for RRS record and Type-A cycloidal pulse model, respectively and the difference between two cases is about 14%. The discrepancies are compatible with the matching levels of the cycloidal pulse model to the recorded ground motion velocity history presented in Fig. 2 where it is seen that Type-A cycloidal pulse model can successfully capture the main pulse of the original velocity record but it differs from the original record after $t = 3$ s.

According to the force-displacement hysteretic curves (Fig. 4), similar to the base displacements, the peak shear forces of LRBs obtained from RRS228 record and Type-A pulse model are close to each other. The difference between two cases is about 10%, where the peak shear forces are 209.90 kN and 230.32 kN under RRS228 record and Type-A pulse model, respectively.

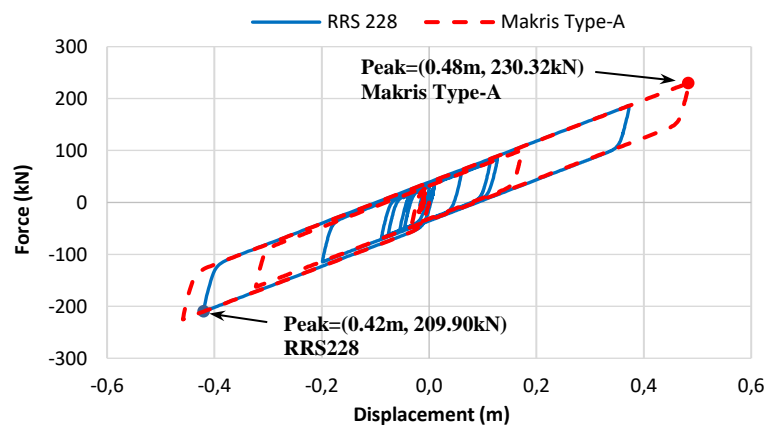


Figure 4. Force-displacement hysteresis of LRBs

4. CONCLUSIONS

In order to investigate the capability of Type-A pulse model in representing the actual pulse-like earthquake records in terms of the isolation system response of seismically isolated buildings considering lead core heating, the base displacement time histories and force-displacement hysteretic curves of LRBs of a benchmark seismically isolated building obtained under RRS228 earthquake record and its approximate counterpart Makris



Type-A cycloidal pulse model [8] is compared. Via the nonlinear time history analyses which consider lead core heating, it is shown that Type-A cycloidal pulse model can capture the overall behavior in terms of both base displacements and lead rubber bearing shear forces although deviations to some extent may be observed. Based on the results obtained here, the cycloidal pulse models can be regarded as effective considering that a complex historical ground motion record is being represented by a simple cycloidal pulse model. However, this finding should be further investigated with various isolation system parameters under different earthquake records. Such an investigation is currently being conducted by the authors of the present study as a part of the ongoing research efforts on this topic.

ACKNOWLEDGMENT

This work was supported by the Scientific Research Projects Coordination Unit of Istanbul University-Cerrahpasa. Project number BYP-2018-28620.

REFERENCES

- [1]. T.H. Heaton, J.F. Hall, D.J. Wald and M.W. Halling, "Response of high-rise and base-isolated buildings to a hypothetical Mw 7.0 blind thrust earthquake", *Science*, vol. 267, pp. 206-211, 1995.
- [2]. C. Alhan, S. and Oncu-Davas, "Performance limits of seismically isolated buildings under near-field earthquakes", *Engineering Structures*, vol. 116, pp. 83-94, 2016.
- [3]. Z. Kanbir, G. Ozdemir, and C. Alhan, "Modeling of Lead Rubber Bearings via 3D-BASIS, SAP2000, and OpenSees Considering Lead Core Heating Modeling Capabilities," *International Journal of Structural and Civil Engineering Research*, vol. 7, no. 4, pp. 294-301, Nov. 2018.
- [4]. I. V. Kalpakidis and M. C. Constantinou, "Effects of heating on the behavior of lead-rubber bearings. I: Theory," *Journal of Structural Engineering*, vol. 135, no.12, pp. 1440-1449, 2009.
- [5]. G. Ozdemir and M. Dicleli, "Effect of lead core heating on the seismic performance of bridges isolated with LRB in near-fault zones", *Earthquake Engineering and Structural Dynamics*, vol. 41, pp.1989-2007, 2012.
- [6]. I. V. Kalpakidis, M. C. Constantinou, and A. S. Whittaker, "Modeling strength degradation in lead-rubber bearings under earthquake shaking," *Earthquake Engineering and Structural Dynamics*, vol. 39, no. 13, pp. 1533-1549, 2010.
- [7]. Z. Kanbir, "Effect of Lead Core Heating on the Behavior of Seismically Isolated Structures", Ph.D. dissertation, Dept. Civil Eng., Istanbul Univ., Istanbul, Turkey, (unpublished).
- [8]. N. Makris, "Rigidity-plasticity-viscosity: can electrorheological dampers protect base-isolated structures from near-source ground motions?", *Earthquake Engineering and Structural Dynamics*, vol. 26, pp. 571-592, 1997.
- [9]. N. Makris and S.P. Chang, "Effect of viscous, viscoplastic and friction damping on the response of seismic isolated structures", *Earthquake Engineering & Structural Dynamics*, vol. 29, pp. 85-107, 2000.
- [10]. B. Alavi and H. Krawinkler, "Consideration of near-fault ground motion effects in seismic design", in *Proc. 12th World Conference on Earthquake Engineering*, 2000, pp. 8.
- [11]. W.L. He and A.K. Agrawal, "Analytical model of ground motion pulses for the design and assessment of seismic protective systems", *J Struct Eng-ASCE*, vol. 134, pp. 1177-1188, 2008.
- [12]. S. Oncu-Davas, H. Gazi and C. Alhan, *Comparison of Ground Motion Pulse Models for the Acceleration Response of Seismically Isolated Buildings*, Architecture Anthology I: Architectural Construction, Materials and Building Technologies, Khatip, J.M., Eds., Athens Institute for Education and Research, pp.229-240, 2015.
- [13]. H. Gazi, S. Oncu-Davas and C. Alhan, *Comparison of Ground Motion Pulse Models for the Drift Response of Seismically Isolated Buildings*, Urban Planning and Civil Engineering, Sisiopiku V.P., Ramadan O. E., Eds., Athens Institute for Education and Research, pp.321-332, 2015.
- [14]. S. Oncu-Davas, H. Gazi, E. Guler and C. Alhan, *Comparison of Ground Motion Pulse Models for the Acceleration Response of Seismically Isolated Liquid Storage Tanks*, Earthquake Engineering and Structural Dynamics in Memory of Ragnar Sigbjornsson, Rupakhety R., Olafsson, S., Eds., Springer, Cham, pp.143-157, 2018.
- [15]. F. McKenna, G. Fenves, and M. Scott, "OpenSees: Open System for Earthquake Engineering Simulation," Pacific Earthquake Engineering Research Center, University of California, Berkeley, CA. Available: <http://opensees.berkeley.edu/>.
- [16]. C. Alhan and M. Surmeli, "Shear building representations of seismically isolated buildings," *Bulletin of Earthquake Engineering*, vol. 9, no. 5, pp. 1643-1671, 2011.
- [17]. P. G. Somerville, "Characterizing near-fault ground motion for the design and evaluation of bridges," in *Third national conference and workshop on bridges and highways*, 29 April-1 May 2002, Portland, Oregon.
- [18]. P. G. Somerville, "Engineering characterization of near-fault ground motions," in *Proc. NZSEE, 2005*, 11-13 March 2005, Taupo, New Zealand.
- [19]. PEER (2005) Pacific earthquake engineering resource center: NGA database. Berkeley: University of California. Available: <http://peer.berkeley.edu/nga/>.



Effect of Accidental Eccentricity on the Isolation System Responses of Cylindrical Liquid Storage Tanks

Elif Guler¹, Cenk Alhan²

Abstract

Liquid storage tanks may be used for storing water, chemicals, petroleum products, toxic or flammable liquids, etc. which makes them strategically and even vitally important structural systems. In recent years, the protection of liquid storage tanks from detrimental effects of earthquakes by introducing isolation systems at the base of these structures has been proposed and different aspects of these systems are evaluated by various researchers. One aspect that is less treated by others is the accidental eccentricity that may come into scene in the isolation system due to various reasons such as errors in the production of isolators, non-uniform variation of the mechanical properties of isolators in time throughout the isolation system plan, etc. And accidental eccentricity may cause significant amplifications particularly in the isolation system responses compared to the completely symmetric case, which could have considerable impact in the design of base-isolated liquid storage tanks. In order to examine this issue, base displacement and isolator shear forces of a benchmark cylindrical liquid storage tank are comparatively examined for different isolation system accidental eccentricities ($e = 0\%$, 5% , and 15%) under a representative near-field and a representative far-field earthquake record. The nonlinear time history analyses are performed with 3D-BASIS-ME academic software which allows for modeling of base-isolated liquid storage tanks through a special modeling approach that combines single-degree-of-freedom systems representing fluid-tank interaction, fluid sloshing, and rigid-convective modes on a common base-mat. Results show that the isolation system responses increase as accidental eccentricity increases.

Keywords: Cylindrical liquid storage tank; isolation system eccentricity; isolation system response; seismic isolation.

1. INTRODUCTION

Protection of liquid storage tanks against detrimental effects of the earthquakes is very important since they typically contain vital, economic and/or strategically important substances [1], [2]. In recent years, the dynamic behavior of liquid storage tanks that are placed on base isolation systems for effective protection of such structures against earthquakes has been investigated and different aspects of these systems are evaluated by various researchers (e.g. [2]-[8]). One aspect that is less treated by others is the accidental eccentricity that may come into scene in the isolation system due to various reasons such as errors in the production of isolators, non-uniform variation of the mechanical properties of isolators in time throughout the isolation system plan, etc. And accidental eccentricity may cause significant amplifications particularly in the isolation system responses compared to the completely symmetric case, which could have considerable impact in the design of base-isolated liquid storage tanks.

In the literature, there exist studies which examine the superstructure or the isolation system eccentricity cases of base-isolated building type structures with different aspects. For example, Gasparini et al. [9] proposed to estimate maximum rotational responses of one-story eccentric systems exposed to dynamic effects by a simplified approach. Tena-Colunga and Zambrana-Rojas [10] conducted nonlinear dynamic analyses under unidirectional and bidirectional records in order to investigate the dynamic torsional response of base-isolated structures with an eccentric isolation system and showed that the maximum isolator displacement of the

¹ Istanbul University-Cerrahpaşa, Department of Civil Engineering, 34320, Avcılar/İstanbul, Turkey. guler.elif@gmail.com

² Corresponding author: Istanbul University-Cerrahpaşa, Department of Civil Engineering, 34320, Avcılar/İstanbul, Turkey. cenkalhan@istanbul.edu.tr



unsymmetric system with respect to the symmetric one increases as the eccentricity increases. Matsagar and Jangid [11] investigated the behavior of a single story asymmetric structure supported on various base isolation systems during the impact with adjacent structures. They showed that the lateral-torsional response of the base-isolated structure creates adverse effects when impact takes place with the adjacent structures. Khoshnoudian and Azad [12] compared the behavior of asymmetric and symmetric structure responses under bidirectional earthquakes and showed that the asymmetry in the superstructure or the isolation system could have a significant effect on the torsional behavior.

However, investigating the accidental eccentricity of the isolation system of base-isolated liquid storage tanks are also very important. In order to contribute to the literature regarding this issue, in this study we examine base displacement and isolator shear forces of a benchmark cylindrical liquid storage tank comparatively for different isolation system accidental eccentricities ($e = 0\%$, 5% , and 15%) under a representative near-field and a representative far-field earthquake record. The nonlinear time history analyses are performed with 3D-BASIS-ME academic software which allows for modeling of base-isolated liquid storage tanks through a simplified approach that combines single-degree-of-freedom systems representing fluid-tank interaction, fluid sloshing, and rigid-convective modes on a common base-mat. In the context of this study, the tank is considered to be full with water and unidirectional time history analyses are considered.

2. MATERIALS AND METHODS

2.1. Cylindrical Liquid Storage Tank

In this study, the cylindrical liquid storage tank model previously presented by [13] is used. The radius, height, and thickness of the cylindrical tank consisting of a steel wall and a concave-down steel roof are 18.29 m, 12.80 m and 2.54 cm, respectively. The tank is supported by a rigid concrete base-mat and is considered to be filled with water up to a height of 12.19 m. The radius and thickness of the concrete base-mat are 18.59 m and 45.72 cm, respectively. The total physical weight above the isolation system that consists of the weights of the steel tank, the water inside, and the concrete base-mat is 142970.29 kN.

2.2. Seismic Isolation System

Here, a nonlinear isolation system consisting of 52 identical elastomeric bearing is modeled underneath the rigid concrete base-mat. The layout of the isolation system for completely symmetric case, which is given in Figure 1, is obtained from [13].

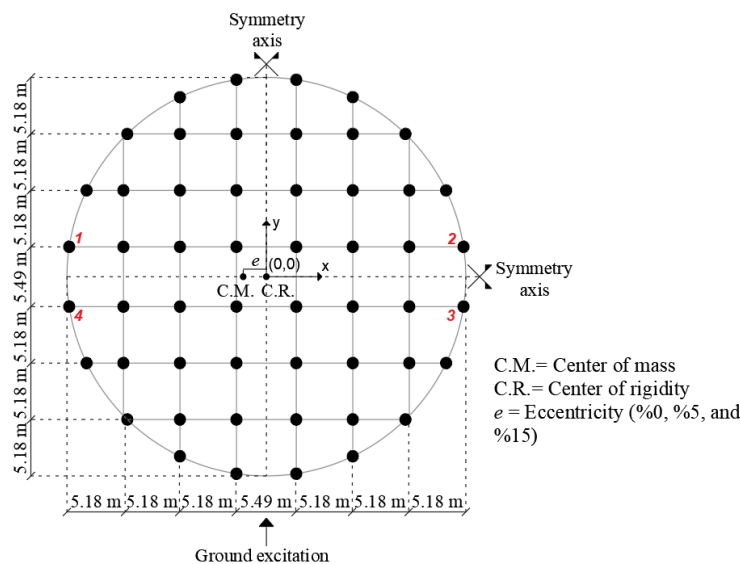


Figure 5. Isolation system plan (modified from Tsopelas et al. [13])



Nonlinear behavior and hysteretic energy dissipation characteristics of these elastomeric bearings are represented by a smooth bi-linear force-displacement relationship which is based on the Bouc-Wen hysteretic model [14]. The rigid-mode isolation period (T_0), the characteristic strength ratio (Q/W), and the yield displacement (D_y) values of the isolation system are considered to be 4 s, 10% and 1.5 cm, respectively. As the effective mass of the tank (M), obtained by subtracting the sloshing mode mass from the total physical mass, is 7178.45 kNs²/m, the post-yield stiffness (K_2) parameter of the isolation system is calculated as 17710.13 kN/m via the relationship $T_0 = 2 \times \pi \times (M / K_2)^{1/2}$. The pre-yield stiffness (K_1) of the isolation system is obtained to be 487405.90 kN/m using the relationship $Q = (K_1 - K_2) \times D_y$ [15]. Finally, the yield force (F_y) and the post-yield to pre-yield stiffness ratio (α) are calculated as 7304.27 kN and 0.036 using the relations $F_y = K_1 \times D_y$ and $\alpha = K_2 / K_1$, respectively.

Different accidental eccentricity cases are generated by shifting the mass along the x-direction with respect to the completely symmetric ($e = 0\%$) case (Figure 1). Base displacement and isolator shear force responses of the base isolated liquid storage tank are investigated for $e = 0\%$ (i.e. no eccentricity), 5% of the diameter (i.e. $36.58 \text{ m} \times 0.05 = 1.83 \text{ m}$), and 15% of the diameter (i.e. $36.58 \times 0.15 = 5.49 \text{ m}$) mass eccentricity cases. Unidirectional earthquake records are applied in y-direction. In order to demonstrate the eccentricity effects in terms of the aforementioned seismic responses clearly, representative isolators which are numbered from 1 to 4 (see Figure 1) are selected.

2.3. Characteristics of the Ground Motion Data

In this section, information on two historical earthquake records obtained from the ground motion database of the Pacific Earthquake Engineering Research Center [16] for use in this study is presented. LGP000 and CAP000 components of the 1989 Loma Prieta earthquake ($M_w = 6.9$, where M_w is the earthquake magnitude) recorded at the LGPC and Capitola stations, respectively are selected as representatives of near-field and far-field earthquake records, respectively. The closest distance to the fault, the peak ground acceleration, and the peak ground velocity values of the LGP000 component are 6.10 km, 0.563 g, and 94.8 cm/s, respectively, while they are 14.50 km, 0.529 g, and 36.5 cm/s for CAP000 component, respectively.

Figures 2 (a) and (b) present the 10% damped acceleration and displacement response spectra of the LGP000 and CAP000 components, respectively. Note that the spectral displacements particularly at long periods (that would be coincident with the isolation period) attain much higher values for the near-field LGP000 component compared to the far-field CAP000 component.

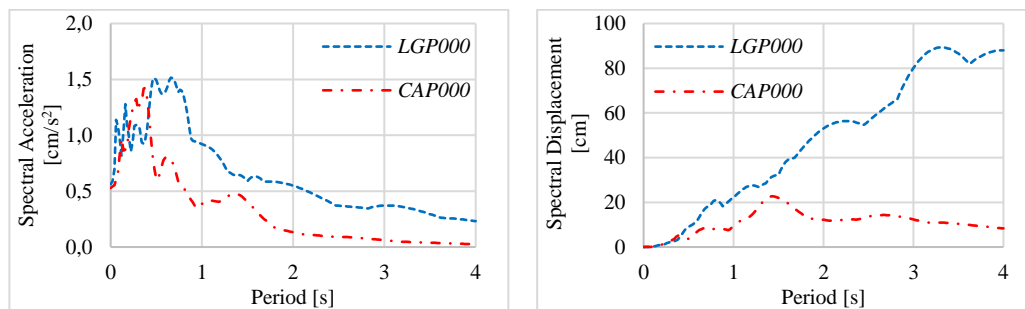


Figure 6. (a) Acceleration response spectra, 10% damped

(b) Displacement response spectra, 10% damped

2.4. Numerical Modeling

Numerical modeling and nonlinear time history analyses are conducted in 3D-BASIS-ME [13] academic software which allows for modeling of base-isolated liquid storage tanks through Haroun and Housner's [17] modeling approach that combines single-degree-of-freedom systems representing fluid-tank interaction, fluid sloshing, and rigid-convective modes on a common base-mat. Using the design charts provided by [17], fluid-tank and fluid sloshing mode weights are obtained to be 53378.66 kN and 72581.63 kN, respectively. The critical damping ratios for the abovementioned modes are assumed as 0.5% and 2.0%, respectively. And the total rigid weight consists of the convective fluid and the concrete base-mat weight is 17010.10 kN.



3. RESULTS AND DISCUSSION

In this section, in order to investigate the effects of the different isolation system accidental eccentricities ($e = 0\%$, 5% , and 15%) on the isolation system responses of the benchmark cylindrical liquid storage tank, unidirectional nonlinear time history analyses are carried out. The analysis results in terms of peak values of base displacement and isolator shear force responses obtained under near-field LGP000 and far-field CAP000 earthquake records are listed in Table 1 and Table 2, respectively. In these tables, while D_x and D_y represent the isolator displacements along x and y directions, shear forces of the isolators are symbolized with F_x and F_y along x and y-directions, respectively.

Table 1. Peak isolator displacements under near-field LGP000 and far-field CAP000 earthquake records.

Isolator No	Peak Isolator Displacement [cm]						
	$e = 0\%$		$e = 5\%$		$e = 15\%$		
	D_x	D_y	D_x	D_y	D_x	D_y	
LGP000	1	0.00	24.72	0.81	29.79	2.19	37.87
	2	0.00	24.72	0.81	19.17	2.19	9.61
	3	0.00	24.72	0.81	19.17	2.19	9.61
	4	0.00	24.72	0.81	29.79	2.19	37.87
CAP000	1	0.00	11.36	0.42	14.00	1.11	17.96
	2	0.00	11.36	0.42	8.45	1.11	3.41
	3	0.00	11.36	0.42	8.45	1.11	3.41
	4	0.00	11.36	0.42	14.00	1.11	17.96

As it can be seen from Table 1 and Table 2, for $e = 0\%$ (no-eccentricity case), there is equal amount of displacement and shear force for all considered isolators in y-direction, which is the direction of earthquake and there is no isolation system response in the x-direction, as expected. On the other hand, as the accidental eccentricity increases, y-direction peak responses of Isolator 1 and Isolator 4, which are close to the center of mass (C.M) increase with respect to $e = 0\%$ case while isolators on the other side (Isolator 2 and Isolator 3) display a reverse behavior. For example, for $e = 15\%$, the large eccentricity case, peak isolator displacement responses of Isolator 1 and Isolator 4 are 1.53 times of the case $e = 0\%$ under LGP000 along y-direction. Additionally, it is noticed that the peak isolation system responses for all considered isolators increase with the increasing eccentricity along x-direction. For example, peak isolator displacement responses for Isolator 1-4 reaches 2.19 cm under LGP000.

Table 2. Peak isolator shear forces under near-field LGP000 and far-field CAP000 earthquake records.

Isolator No	Peak Isolator Shear Force [kN]						
	$e = 0\%$		$e = 5\%$		$e = 15\%$		
	F_x	F_y	F_x	F_y	F_x	F_y	
LGP000	1	0.00	219.52	9.29	236.69	16.03	264.05
	2	0.00	219.52	18.51	200.53	60.67	164.76
	3	0.00	219.52	18.51	200.53	60.67	164.76
	4	0.00	219.52	9.29	236.69	16.03	264.05
CAP000	1	0.00	174.06	6.66	182.96	12.37	196.26
	2	0.00	174.06	12.14	163.96	49.82	137.85
	3	0.00	174.06	12.14	163.96	49.82	137.85
	4	0.00	174.06	6.66	182.96	12.37	196.26

In addition to the peak responses presented above, isolator displacement-time and isolator shear force-displacement histories under representative LGP000 earthquake record are presented in Figures 3 and 4, respectively. While Figures 3 (a) and (b) present the isolator displacement responses of Isolator 1 for all considered accidental eccentricity cases in x and y-directions, respectively, Figures 3 (c) and (d) compare the isolator displacement response of Isolator 1 with the Isolator 4 along the x-direction and Isolator 1 with Isolator



2 along the y-direction, respectively for $e = 15\%$ case. Figures 4 (a) and (b) present the shear force-displacement history of Isolator 1 for all accidental eccentricity cases in x and y-directions, respectively.

Figures 3 (a) and (b) show that displacement responses of Isolator 1 are amplified along both x and y-directions throughout the whole time history as the eccentricity increases. As seen from Figure 3 (c), the x-direction displacement responses of Isolator 1 and Isolator 4, which are placed on opposite sides of the symmetry axis along x-direction, are out-of-phase and small, as expected. The displacement responses of Isolator 2, which is located on the opposite far-end side of the symmetry axis along y-direction compared to the location of Isolator 1, attain much smaller values and they are in-phase. Finally, as it can be clearly seen from Figures 4 (a) and 4 (b), the shear force responses of Isolator 1 increase for both in x and y-direction as the accidental eccentricity increases. F_y and D_y responses are larger than the F_x and D_x ones since earthquake acts in y-direction.

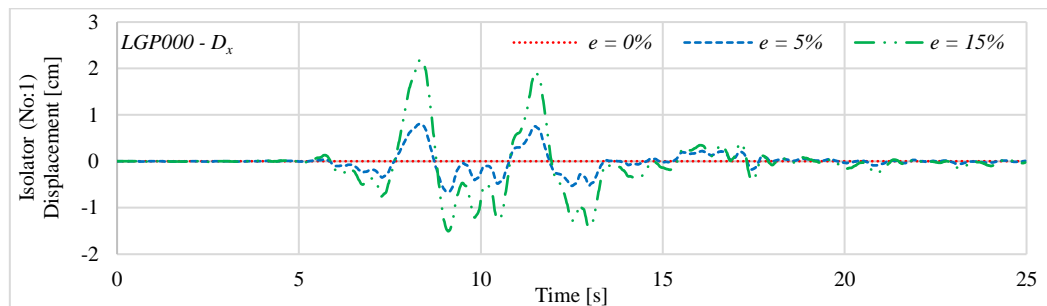
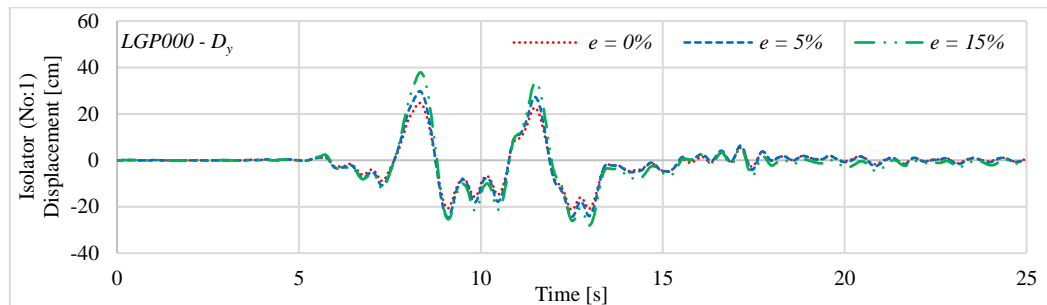
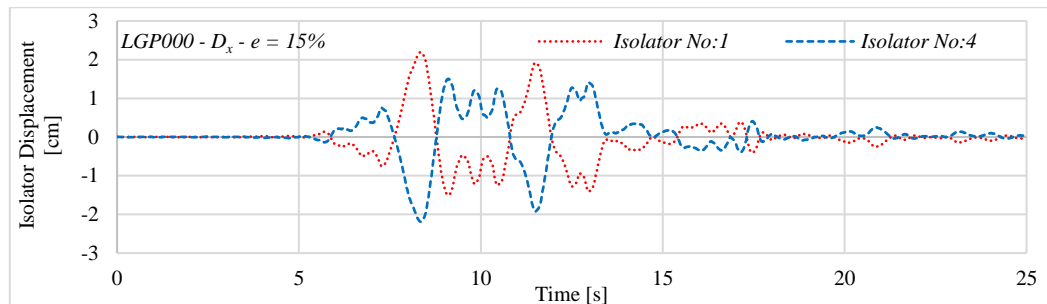


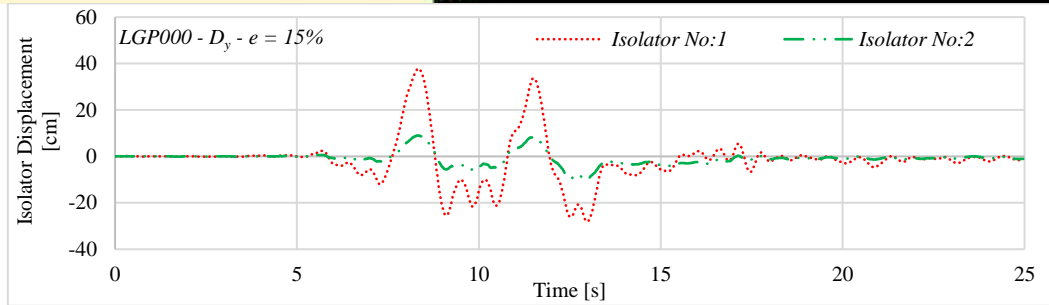
Figure 7. (a) Displacement-time histories of Isolator 1 along x-direction under LGP000 earthquake record



(b) Displacement-time histories of Isolator 1 along y-direction under LGP000 earthquake record



(c) Displacement-time histories of Isolator 1 and 4 along x-direction under LGP000 earthquake record ($e = 15\%$)



(d) Displacement-time histories of Isolator 1 and 2 along y-direction under LGP000 earthquake record ($e = 15\%$)

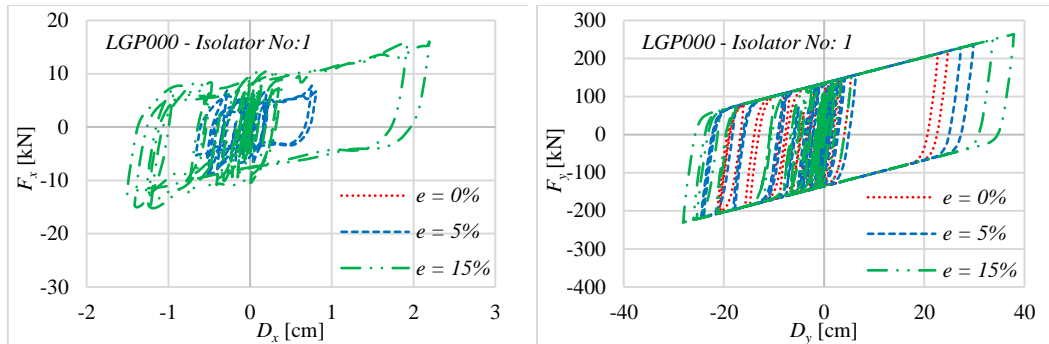


Figure 8. (a) Force-displacement histories of Isolator 1 along x-direction under LGP000 earthquake record

(b) Force-displacement histories of Isolator 1 along y-direction under LGP000 earthquake record

4. CONCLUSIONS

In this study, nonlinear time history analyses of a benchmark cylindrical liquid storage tank placed on isolation systems with different accidental eccentricities ($e = 0\%$, 5% , and 15%) are conducted under the unidirectional near-field LGP000 and far-field CAP000 earthquake records. Analyses results are evaluated in terms of the isolation system responses including isolator displacements and isolator shear forces.

It is shown that both the peak isolator displacements and the peak isolator shear forces may increase or decrease in both orthogonal directions as the accidental eccentricity increases depending on the location of the isolators with respect to the center of mass. Based on the results obtained here, it is concluded that the influence of the isolation system accidental eccentricity on the seismic responses may be rather significant. Amplified isolator displacements and isolator shear forces should be taken into account during design phase as rupture or buckling of isolators may be faced otherwise.

As part of the ongoing studies related to the investigation of the effect of accidental eccentricity on the seismic responses of base-isolated cylindrical liquid storage tanks, this study is being expanded by the authors considering other seismic response parameters, different isolation system properties and different earthquake records.

ACKNOWLEDGMENT

This work was supported by the Scientific Research Projects Coordination Unit of Istanbul University-Cerrahpasa. Project number BYP-2018-28620.



REFERENCES

- [1]. O. R. Jaiswal, D. C. Rai and S. K. Jain, "Review of seismic codes on liquid-containing tanks," *Earthquake Spectra*, vol. 23, pp. 239-260, February 2007.
- [2]. E. Guler, C. Alhan and H. Gazi, "Liquid storage tanks with linear isolation systems: sensitivity of seismic performance to deviations in effective stiffness and damping," in *Proc. ICOCEE*, 2017, p. 620-629.
- [3]. V. R. Panchal and R. S. Jangid, "Variable friction pendulum system for seismic isolation of liquid storage tanks," *Nuclear Engineering and Design*, vol. 238, pp. 1304-1315, 2008.
- [4]. P. B. Waghmare, P. S. Pajgade and N. M. Kanhe, "Seismic response of isolated liquid storage tanks with elastomeric bearings", *International Journal of Application or Innovation in Engineering and Management*, vol. 2, pp. 82-87, February 2013.
- [5]. E. Guler, C. Alhan and H. Gazi, "Sensitivity of the seismic performance of liquid storage tanks with nonlinear isolation systems to deviations in mechanical characteristics of the seismic isolators," in *Proc. 6th ECCOMAS*, 2017, p. C18237.
- [6]. M. E. Kalogerakou, C. A. Maniatakis, C. C. Spyarakos and P. N. Psarropoulos, "Seismic response of liquid-containing tanks with emphasis on the hydrodynamic response and near-fault phenomena," *Engineering Structures*, vol. 153, pp. 383-403, 2017.
- [7]. C. Alhan, H. Gazi and E. Guler, "Influence of isolation system characteristic strength on the earthquake behavior of base-isolated liquid storage tanks," *Indian Journal of Engineering and Material Sciences*, vol. 25, pp. 346-352, 2018.
- [8]. S. Oncu-Davas, H. Gazi, E. Guler and C. Alhan, Chapter 7: *Comparison of Ground Motion Pulse Models for the Seismic Response of Seismically Isolated Liquid Storage Tanks*, eds. R. Rupakhety and S. Olafsson, Iceland, Springer International Publishing, 2018.
- [9]. G. Gasparini, S. Silvestri and T. Trombetti, "A simplified approach to the Analysis of torsional effects in eccentric systems: the Alpha method," in *Proc. 13 WCEE*, 2004, paper 451.
- [10]. A. Tena-Colunga and C. Zambrana-Rojas, "Dynamic torsional amplifications of base-isolated structures with an eccentric isolation system," *Engineering Structures*, vol. 28, pp. 72-83, 2006.
- [11]. V. A. Matsagar and R.S. Jangid, "Impact response of torsionally coupled base-isolated structures," *Journal of Vibration and Control*, vol. 16, pp. 1623-1649, 2010.
- [12]. F. Khoshnoudian and A. I. Azad, "Effect of two horizontal components of earthquake on nonlinear response of torsionally coupled base isolated structures," *The Structural Design of Tall and Special Buildings*, vol. 20, pp. 986-1018, April 2011.
- [13]. P. C. Tsopelas, M. C. Constantinou, and A.M. Reinhorn, "3D-BASIS-ME: Computer program for nonlinear dynamic analysis of seismically isolated single and multiple structures and liquid storage tanks," State Univ. of New York, Buffalo, NY, Tech. Rep. NCEER -94-0010, 1994.
- [14]. Y. K. Wen, "Method for random vibration of hysteretic systems," *Journal of the Engineering Mechanics Division (ASCE)*, vol. 102, pp. 249-263, 1976.
- [15]. F. Naeim and J. M. Kelly, *Design of Seismic Isolated Structures: From Theory to Practice*, New York: John Wiley and Sons, 1999.
- [16]. (2013) Pacific earthquake engineering resource center: NGA-West2 Database. Berkeley University of California. [Online]. Available: <http://ngawest2.berkeley.edu/site>
- [17]. M. A. Haroun, and G. W. Housner, "Seismic design of liquid storage tanks," *Journal of the Technical Councils of ASCE*, vol. 107, pp. 191-207, April 1981.



The Benefits and Challenges of On-Site 3D-Printed Construction: A Case Study

Jeneé A. Jagoda¹, Michael P. Case², Brandy N. Diggs-McGee², Eric L. Kreiger², Megan A. Kreiger², Steven J. Schuldt³

Abstract

In 2018, U.S. Marines, Navy, Air Force, and Army Corps personnel demonstrated the capability of 3D-printed construction in an expeditionary environment at Camp Pendleton, California. The tri-service exercise culminated in the construction of a 10-meter concrete bridge – the first of its kind to be both printed and placed in a field environment. In this exercise, the 3D printer was transported from Champaign, Illinois to Camp Pendleton, where a team of Marines assembled it close to where the bridge would be placed. The Marines performed initial beam and pier design; the Army Corps completed the structural design, steel reinforcement, and coding. The concrete ingredients were measured and mixed using a volumetric mixer and skid steer. After mixing, the concrete was pumped through a hose to the printer nozzle. Each beam was printed sequentially; the piers were printed concurrently. Reinforcement and forklift pockets were laid manually during pauses between print layers. As printing progressed, the finished members were covered and allowed to cure for two to five days before placement. Despite challenges with weather, materials, hardware, and power, the U.S. military successfully demonstrated the potential of 3D-printed construction in the expeditionary environment by proving it is possible to print and place a bridge on-site using locally sourced materials. The U.S. military also exhibited the potential of 3D printing to reduce the labor, materials, and logistics required for military construction. Furthermore, the exercise revealed additional, future opportunities to automate the 3D printing process and lessen the manpower demand.

Keywords: 3D-printed construction, 3D printer, bridge, concrete, military

1. INTRODUCTION

In December 2018, U.S. Marines from the 7th Engineering Support Battalion (7th ESB), Navy Seabees from Naval Mobile Construction Battalion FIVE (NMCB 5), an Air Force officer from the Air Force Institute of Technology, and researchers from the Army Engineer Research and Development Center - Construction Engineering Research Laboratory (ERDC-CERL) demonstrated the capability of three-dimensional (3D) printed construction in an expeditionary environment at Marine Corps Base Camp Pendleton, California. The demonstration was part of Exercise Steel Knight, a Marine-led exercise spanning the western United States that focused on military skills, tactics, and capabilities utilized in the expeditionary environment. The exercise's 3D-printing component had three primary goals: to train the 7th ESB in the printer assembly and construction process; to integrate NMCB 5's volumetric mixer, the "CreteMobile," into the material preparation process; and to construct the first 3D-printed bridge in a field setting in the Americas. Furthermore, the bridge was designed to support a team of Marines crossing in full gear shortly after placement. While this proof-of-concept was the first time four branches of the military collaborated on a single 3D printing effort, it is one of a series of advancements to military 3D printing efforts achieved by ERDC-CERL in recent years.

¹ Corresponding author: Air Force Institute of Technology, Graduate School of Engineering Management, 2950 Hobson Way, Wright Patterson AFB, OH 45431. jenee.jagoda@afit.edu

² Construction Engineering Research Laboratory, United States Army Corps of Engineers Engineer Research and Development Center, 2902 Newmark Dr., Champaign, IL 61822.

³ Air Force Institute of Technology, Graduate School of Engineering Management, 2950 Hobson Way, Wright Patterson AFB, OH 45431.



1.1. 3D Printing

3D printing is an advanced additive manufacturing process capable of producing a range of complex structures and components without formwork using a layer-by-layer material deposition approach [1]–[3]. Charles Hull developed the first 3D printer in 1986 using stereolithography; soon after, the manufacturing sector adopted the technique [3], [4]. 3D printing was not applied to the building and construction industry until 1997, when Joseph Pegna made the first attempt at cement-based additive manufacturing [5]. The following year, Behrokh Khoshnevis, a professor at the University of Southern California, invented the contour crafting method, which uses a trowel to create smooth and accurate edges and surfaces [6]. Currently, over thirty groups are researching and developing 3D-printed construction technology around the world [7].

While still in the early stages of research and development, 3D-printed construction has the potential to outperform conventional construction due to its ability to lower total costs, decrease labor requirements, eliminate the need for formwork, reduce material utilization, shorten construction duration, increase customization, and enhance sustainability [1], [3], [8]–[10]. In addition to these benefits, 3D-printed construction is capable of greater strength than its conventionally cast counterparts and, thanks to the elimination of formwork, can be used in more complex structural applications [4], [7].

1.2. ACES Program History

ERDC-CERL established the Automated Construction of Expeditionary Structures (ACES) program in 2015 to develop the capability to print custom-designed expeditionary structures in the field, on demand, using locally available materials [11]. The goals of the ACES program include minimizing manpower requirements, decreasing material usage, reducing the logistical demand and supply train in the expeditionary environment, and building stronger, more durable structures. In 2017, the ACES team printed a 4.9m x 9.75m x 2.4m (16ft x 32ft x 8ft) concrete building in Champaign, Illinois: the first full-scale, 3D-printed concrete building in the United States [12]. This was quickly followed by the first military demonstration of 3D-printed concrete with the U.S. Marine Wing Support Squadron 372 (MWSS 372), which produced unique wall sections for testing utilizing the 3D printer known as ACES Lite (Figure 1). ACES Lite is a prototype deployable 3D printing system designed and built under a cooperative research and development agreement between Caterpillar and ERDC-CERL. The printer was designed to be highly transportable, easy to assemble, and operable by minimum personnel. It is currently ERDC-CERL’s most efficient and highly utilized printer in the field.

Due to its transportability, ACES Lite is involved in many on-site and off-site demonstrations. In April 2018, the ACES Lite team helped train Army personnel at the Maneuver Support, Sustainment, Protection, Integration Experiment at Fort Leonard Wood, Missouri during the first field-tested, 3D-printed concrete experiment in the world. In August 2018, the team collaborated with Marines from the 7th ESB and MWSS 372 to continuously print a second building in Champaign [13]. After the success of the completed structure, the 7th ESB requested a demonstration of 3D printing capabilities at Camp Pendleton as part of Exercise Steel Knight to create a 3D-printed concrete bridge.



Figure 9. ACES Lite assembled on-site at Camp Pendleton, CA



2. MATERIALS AND METHODS

The 3D printing process can be broken into four main steps: printer transportation and assembly; structural design and programming; material preparation; and printing, curing, and placement.

2.1. Transportation & Assembly

Currently, only three ACES printers have been developed and tested, and all are based at ERDC-CERL in Champaign. In order to transport ACES Lite to Camp Pendleton, the printer was disassembled, organized, and packed for the first time ever into a 6m x 2.1m x 3m (20ft x 7ft x 1ft) shipping container by a team of four people in two hours. Supplies and supporting equipment, such as toolboxes, a power washer, and a tent to protect the computer from the elements were also packed into the shipping container. The container was subsequently loaded onto a semi-truck, where it began its 3-day, 3,250km (2020mi) journey across the U.S.

Upon arrival at Camp Pendleton, a team of seven Marines, previously untrained on the equipment or setup, assembled the printer in 58 minutes under the supervision and instruction of the ERDC-CERL personnel. The frame required 21 minutes to assemble, the bridge required 4 minutes, the ballasts required 10 minutes, and the remaining components of the printer (e.g. hose, nozzle, etc.) required 23 minutes. The printer assembly process is facilitated by lightweight, labeled components; simple connections; the requirement for only simple tools; and the opportunity to assemble some sections, such as the bridge, on the ground before lifting them into place. After the demonstration was complete, the printer was disassembled and packed into the same shipping container in 25 minutes for its return trip to Champaign.

2.2. Structural Design & Programming

The temporary bridge structure was comprised of beams and piers. The initial beam and pier design was conducted by the Marines and modeled using AutoCAD before being sent to ERDC-CERL for determination of reinforcement locations and conversion to Linux computer numerical control (CNC) G-code. The bridge was designed to span a 9.75m (32ft) dry culvert located 0.2km (0.1mi) from the print site on Camp Pendleton. It consisted of three 3.35m (11ft) long beams and two 2.1m (7ft) tall piers with 2.1m x 0.91m (7ft x 3ft) bases. Each beam is a Double-T type beam consisting of one 0.91m (3ft) wide, 0.1m (0.33ft) deep flange and two 0.36m (1.2ft) wide, 0.25m (0.83ft) deep webs (Figure 2). The concrete mix incorporated polyolefin monofilament fibers for increased toughness and resistance to temperature changes and shrinkage. The flange was reinforced with weld wire fabric; the beams were constructed with top and bottom steel reinforcing bars. Since the design was intended to be temporary, the piers were only designed to take vertical compression loads. Therefore, in this instance, the pier was only reinforced every five layers with reinforcing mesh and relied primarily on the concrete to take the temporary loads.

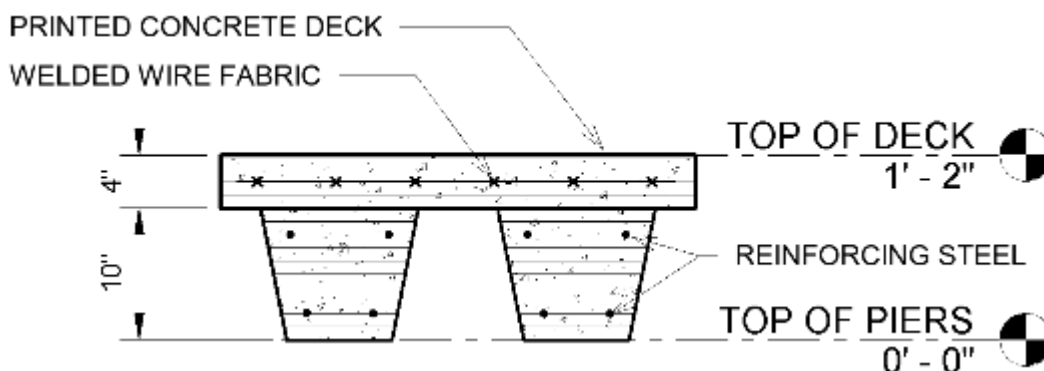


Figure 10. Beam cross-section

Prior to printing, the printer was manually leveled and calibrated by moving the nozzle to one corner of the frame, which acted as a reference point from which the rest of the printer could be leveled. While the print path was pre-programmed into the computer, the print speed and pump flow rate were both adjusted manually using a CNC controller and variable frequency drive (VFD) pump controller, respectively. Due to variation in concrete batches, both the print speed and pump flow rate required adjustments to attempt to maintain a constant rate of material deposition.



2.3. Material Preparation

The concrete mix used for the print was comprised of cement, fine aggregate, coarse aggregate, short polyolefin monofilament fibers, water, and rheology-controlling admixtures. In past printing demonstrations by ERDC-CERL and the 7th ESB, concrete was measured and mixed manually in small batches [14], [15]. Although these demonstrations proved that 3D printing could be expedient and cost-effective in comparison to conventional construction methods, the material measurement process was time-consuming, labor-intensive, and impractical for the expeditious environment. In an effort to better simulate the methods and equipment available on military deployments, Exercise Steel Knight leveraged the use of the Navy Seabees’ CreteMobile, a volumetric mixer manufactured by Brothers. After manually loading each ingredient into its respective hopper within the CreteMobile, the mixer was calibrated to ensure accurate mix proportions.

Once fully calibrated, the CreteMobile produced a test batch of concrete. Concerns quickly arose regarding the effect of the previous days’ rain on the CreteMobile’s ability to mix the batches accurately. After repeated test batches, visual inspection of the prepared concrete determined that the mixture produced by this method could not be utilized due to the moisture content of the fine aggregate. Rain had left the sand wet, causing it to clump and preventing the CreteMobile from precisely dispensing the required proportion of fine aggregate. An additional Cementech mixer located on-site experienced the same issues. The decision was made to use the CreteMobile to efficiently measure out the required proportions of other ingredients (cement, coarse aggregate, and fibers) and dispense them into a small concrete batch mixer attached to a skid steer. The fine aggregate and water were measured manually and added to the skid steer attachment for mixing. Once mixed, each batch was transferred to the concrete pump with VFD modification for immediate use by the printer and vibrated by a Navy Seabee to liquefy the mixture, reduce internal friction, eliminate the air voids, and push the concrete through the pump.

2.4. Printing, Curing, & Placement

After assembly, programming, calibration, and material preparation were complete, printing began. A plastic tarp was laid down on the print surface to prevent the printed concrete from adhering to the existing pavement. The beams were printed first due to their simpler design, followed by the piers. On 7 December, Beams 1 and 2 were printed; beams 3 and 4 were completed on 8 December. Each beam was printed sequentially; a fourth beam was printed in the event that one of the other three beams was damaged during transportation and on-site placement. Given the design of the bridge, each beam was printed upside-down: the bridge deck was printed first (Figure 3 (a)), while the two girders supporting the deck and transferring force to the piers were printed afterward. ACES Lite does not yet have the capability to automate the placement of reinforcement; therefore, the computer operator followed construction plans with detailed layer-by-layer reinforcement instructions and manually paused the print to allow for the insertion of rebar or wire mesh reinforcement (Figure 3 (b)). Rebar loops were placed using the same method to facilitate the beams’ transportation to their final location. At the conclusion of printing, all of the beams were covered with plastic tarps and allowed to cure. Beams 1 and 2 cured for five days; beams 3 and 4 cured for four days.



Figure 11. (a) Printing beam 1



(b) Placing rebar on beam 1

Printing of the two piers began on 8 December and continued through 10 December. Due to their height and number of layers, the piers were printed concurrently; however, each printed as a separate program. Consequently, after printing several layers of one pier, the print was paused and the nozzle was manually calibrated to pick up where printing left off on the other pier – this pattern continued until the completion of



the two piers. As with the bridge beams, steel reinforcement was manually placed into the piers at the appropriate points in the print. However, due to the size and dimensions of the piers, each pier was also constructed with both rebar loops and two forklift pockets to facilitate transportation. These pockets were not programmed into the design; therefore, after a certain layer height was reached, the pocket locations were marked, printed concrete was removed by hand, and coated foam molds were placed to create voids in the finished components. Due to the size of the piers and the need to print both concurrently, the piers required multiple days to complete. When printing stopped for the night, the print surface of each pier was texturized to minimize the adverse effects of cold joints and promote bonding between the hardened and fresh concrete when the print resumed. The completed piers were covered with wet textiles and cured for two days.

With the exception of the ends of each bridge beam, which were hand-trowelled to facilitate a smooth connection between beams; and the edges of both piers, which were hand-trowelled to ensure proper material compaction and prevent collapse, the surfaces of the components were not finished. This was done in order to highlight the 3D-printed nature and layered appearance of the completed bridge.

On 12 December, the completed bridge components were lifted onto a flatbed truck using a 7-ton crane, transported from the print site to the dry culvert, and placed in their final location by crane. The two piers were placed first, followed by the outer bridge beams and finally the center bridge beam. The fourth bridge beam printed in the event of damage was not required. The entire placement process took three hours, and the completed bridge supported twenty people simultaneously.

3. RESULTS AND DISCUSSION

Ultimately, Exercise Steel Knight achieved all three of the Marines' objectives: to train the 7th ESB, utilize the CreteMobile (albeit in a modified capacity), and construct a bridge. The Camp Pendleton bridge is the first 3D-printed bridge in North America and the first 3D-printed bridge in the world to be printed in a field environment. While the proof-of-concept was successful, several challenges encountered over the course of the demonstration provide opportunities to improve the technology and process.

3.1. Weather

Shortly after completing the printer assembly and site set-up, Camp Pendleton experienced inclement weather, necessitating the cancellation of 1.5 days of printing. As a result of this lost time, the bridge was completed later than expected and other planned elements of the exercise had to be cancelled. Additionally, the heavy rain altered the moisture content of the fine aggregate, which resulted in subsequent material issues as discussed in section 2.3. Inability to control the weather is one of the biggest challenges and unknowns of on-site or near-site 3D printing and will need to be accounted for in future 3D printing developments.

3.2. Hose & Nozzle Clogging

As a general rule of thumb, coarse aggregate diameter should not exceed one-third of the diameter of the nozzle in order to reduce the chances of clogging. The aggregates delivered to the site had a high level of variation from the initial sampling of aggregates, including dissimilar materials delivered by the same supplier between loads, which led to complexities associated with variations in the mix. The varying aggregate size (often exceeding 1cm (0.4in) in a 3.2cm (1.25in) nozzle), coupled with the addition of polyolefin monofilament fibers, caused clogs in the hose and nozzle. Each time the team encountered a clog that could not be eliminated by placing more concrete in the pump (and therefore more pressure in the hose), the hose had to be disassembled into sections and flushed out with water and a foam ball. If flushing was not immediately possible, the hose was pounded with sledgehammers to prevent the concrete from setting prematurely in the hose. If the flushing process took more than a few minutes to complete, the concrete left in the pump often stiffened to the point that it had to be shoveled out and replaced with a fresh batch.

In an effort to reduce the frequency of clogging, the 3.2cm (1.25in) nozzle (Figure 4 (a)) was removed and replaced with a new, 5.1cm (2in) nozzle (Figure 4 (c)) to allow for a larger filament size and smoother flow. In the interim between nozzles, there was a brief period of time in which the component was printed without any nozzle (Figure 4 (b)), resulting in lower print resolution and less control over the material flow. Once the new nozzle was attached, the team found it did reduce the instances of clogging in the printing process. Figure 4 depicts the effect of each nozzle on the print filament.



Figure 12. (a) Original 3.2cm nozzle (b) No nozzle (c) New 5.1cm nozzle

The clogging issues can be mitigated in future prints by modifying the G-code to reduce delays; controlling the concentration of fibers; using less large aggregate or reducing the size of the small aggregate; employing a larger and more powerful pump, hose, and nozzle (which would decrease the amount of time needed to print a component, while also reducing the print resolution); adding a “purge point” to the hose (so the hose sections do not need to be removed and separated in order to flush out stiff concrete); and having additional spare hoses and nozzles on hand (to expedite the flushing process in the event that a clog does occur).

3.3. Generator Failure

In order to simulate the conditions experienced on military deployment, in lieu of traditional power, a multi-outfitted generator supplied power to the 3D printer. A Marine power production technician was assigned to monitor and maintain the printer for the duration of the print. Despite this precaution, on 9 December, the generator failed in the early afternoon, midway through printing the two piers. Without the generator, the print was paused with concrete suspended in the pump, hose, and nozzle, unable to be cleared until power was restored. The team again used sledgehammers to pound the hose and prevent the concrete from setting.

It took approximately 45 minutes for the Marine technician to get the generator back online. Once it was back online, the hose and nozzle were both flushed out, the concrete in the pump had to be disposed of and replaced with a fresh batch, and the computer had to be manually recalibrated to recognize where the print path left off. The interruptions in printing and ultimate generator failure were attributed to unidentified power surges and a need to service the generator.

3.4. Material Collapse

Despite the popularity of concrete in 3D-printed construction, research on its printed properties is limited and designs constructed of different materials under varying conditions still need to be assessed for overall material and structural quality [16], [17]. Prior to starting the exercise, the team lead acknowledged that materials are the biggest risk and unknown of the 3D printing process because of uncertain and varying material quality and performance. The team did not encounter any material collapse issues while constructing the four beams; however, collapse under self-weight did become an issue while printing the piers, which were substantially larger, taller, and had more layers. In order to allow sufficient time for early strength to develop to support subsequent layers, only 7-10 consecutive layers could be printed at a time before pausing the print to work on the other pier. Even with this practice in place, at several points, wet concrete sheared off of the sides of the pier as a result of inconsistent concrete flow from layer to layer near the edges of the pier, as seen in Figure 4. Communication challenges between the CNC controller and VFD pump controller also led to material collapse: at one point, the print path was paused to resolve an issue, but the pump continued to transport concrete through the hose to the nozzle, resulting in the rapid deposit of excess material to one edge of the pier and a subsequent collapse. Each time a small section of the pier collapsed, it was manually repaired before continuing the print.



Figure 13. Material collapse under self-weight

The possibility of material collapse can be reduced by implementing best practices for print design, limiting the number of consecutive layers printed at a time, printing tall components concurrently to increase initial curing time and early strength, designing the geometry of the print to be self-stable under its own weight, troweling the surface and edges of the component during printing, incorporating accelerators into the concrete mix, and synchronizing the VFD and CNC controls to avoid miscommunication between individuals.

3.5. Labor Considerations

As construction becomes increasingly automated, the quantity of laborers needed – and the associated number of injuries and hazards incurred – is expected to decrease, helping to eliminate risk and reduce the costs associated with both the labor itself and the potential injury or fatality [1], [2], [18]. However, the current printing process used in Exercise Steel Knight is still fairly labor-intensive. It required a small team of individuals to prepare and mix the concrete (a minimum of two: one to measure the ingredients and one to operate the skid steer), one individual to vibrate the concrete, one individual to monitor and control the pump flow rate, and one individual to monitor and control the print speed using the computer. These individuals also placed the reinforcement and manually repaired the piers as needed during pauses between print layers. During tasks such as initial set-up, end of day clean-up, and flushing out the clogged hose, it was helpful to have additional laborers on hand to expedite the work.

As development and testing of ACES Lite continues, these tasks will become increasingly automated, reducing the manpower required on the print site. Replacing the current concrete pump with a self-vibrating model, synchronizing the VFD and CNC controls with the main computer, automating the placement of reinforcement, and utilizing trowels to finish the print surface (as the ERDC-CERL team did on the first full-scale 3D-printed concrete building in the U.S.) could reduce the printing labor requirement by up to 40%.

4. CONCLUSIONS

Despite challenges with weather, materials, hardware, and power, the U.S. military successfully demonstrated the potential of 3D-printed construction in the expeditionary environment by proving it is possible to print and place a bridge on-site using locally sourced materials, resulting in the first 3D-printed bridge in the world to be printed in a field environment in 12 hours of total print time (Figure 6). Additionally, the exercise accomplished the two additional Marine goals of training their personnel and incorporating the Seabees' volumetric mixer into their printing efforts and achieved continued progress towards CERL's overarching goals of reducing the manpower, materials, and logistics required for construction. Furthermore, the exercise revealed additional, future opportunities to automate the 3D printing process and lessen the manpower demand by upgrading the pump, synchronizing the VFD and CNC controls with the main computer, developing methods of automating the placement of reinforcement, and streamlining the set-up and clean-up process through continuous printing operations.



Figure 14. Completed bridge

An in-depth analysis of time, labor, and material requirements is necessary to determine whether the current state of development of 3D-printed construction outperforms conventional construction in the field environment. However, this proof-of-concept is evidence that 3D printing in the military expeditionary environment is possible and holds great potential, and developments are on track for it to become a standard element of military construction in the future.

ACKNOWLEDGEMENTS

The views expressed in this paper are those of the authors and do not reflect the official policy or position of the United States Air Force, Department of Defense, or the United States government.

The ACES Lite printer used for this research and proof-of concept was developed by ERDC-CERL and Caterpillar, Inc. under a cooperative research and development agreement. The authors would like to thank Caterpillar, Inc. for their role in the design and construction of the printer and Dan Sergison, a Caterpillar engineer, for providing on-site support during Exercise Steel Knight.

REFERENCES

- [1] J. J. Biernacki *et al.*, "Cements in the 21st century: Challenges, perspectives, and opportunities," *Journal of the American Ceramic Society*, vol. 100, no. 7, pp. 2746–2773, 2017.
- [2] Y. W. D. Tay, B. Panda, S. C. Paul, N. A. Noor Mohamed, M. J. Tan, and K. F. Leong, "3D printing trends in building and construction industry: a review," *Virtual and Physical Prototyping*, vol. 12, no. 3, pp. 261–276, Jul. 2017.
- [3] P. Wu, J. Wang, and X. Wang, "A critical review of the use of 3-D printing in the construction industry," *Automation in Construction*, vol. 68, pp. 21–31, Aug. 2016.
- [4] G. Ma, L. Wang, and Y. Ju, "State-of-the-art of 3D printing technology of cementitious material—An emerging technique for construction," *Science China Technological Sciences*, vol. 61, no. 4, pp. 475–495, Apr. 2018.
- [5] J. Pegna, "Exploratory investigation of solid freeform construction," *Automation in Construction*, vol. 5, no. 5, pp. 427–437, Feb. 1997.
- [6] B. Khoshnevis and R. Dutton, "Innovative Rapid Prototyping Process Makes Large Sized, Smooth Surfaced Complex Shapes in a Wide Variety of Materials," *Materials Technology*, vol. 13, no. 2, pp. 53–56, Jan. 1998.
- [7] R. A. Buswell, W. R. Leal de Silva, S. Z. Jones, and J. Dirrenberger, "3D printing using concrete extrusion: A roadmap for research," *Cement and Concrete Research*, vol. 112, pp. 37–49, Oct. 2018.
- [8] M. A. Kreiger, B. A. MacAllister, J. M. Wilhoit, and M. P. Case, "The Current State of 3D Printing for Use in Construction," in *Proceedings of the 2015 Conference on Autonomous and Robotic Construction of Infrastructure*, Ames, Iowa, 2015, pp. 149–158.



- [9] T. D. Ngo, A. Kashani, G. Imbalzano, K. T. Q. Nguyen, and D. Hui, "Additive manufacturing (3D printing): A review of materials, methods, applications and challenges," *Composites Part B: Engineering*, vol. 143, pp. 172–196, Jun. 2018.
- [10] P. Wu, X. Zhao, J. H. Baller, and X. Wang, "Developing a conceptual framework to improve the implementation of 3D printing technology in the construction industry," *Architectural Science Review*, vol. 61, no. 3, pp. 133–142, May 2018.
- [11] "Automated Construction of Expeditionary Structures (ACES)," *Engineer Research and Development Center*. [Online]. Available: <http://www.erd.usace.army.mil/Media/FactSheets/FactSheetArticleView/tabid/9254/Article/1290247/automated-construction-of-expeditionary-structures-aces.aspx>. [Accessed: 29-Apr-2019].
- [12] M. Jazdyk, "3-D printing a building," *Engineer Research and Development Center*, 22-Aug-2017. [Online]. Available: <http://www.erd.usace.army.mil/Media/NewsStories/tabid/9219/Article/1281737/3-d-printing-a-building.aspx>. [Accessed: 05-Mar-2019].
- [13] J. Rogers, "Marines 3D-print concrete barracks in just 40 hours," *Fox News*, 29-Aug-2018. [Online]. Available: <https://www.foxnews.com/tech/marines-3d-print-concrete-barracks-in-just-40-hours>. [Accessed: 29-Apr-2019].
- [14] E. L. Kreiger, M. A. Kreiger, and M. P. Case, "Development of the construction processes for reinforced additively constructed concrete," *Additive Manufacturing*, vol. 28, pp. 39–49, Aug. 2019.
- [15] B. Diggs-McGee, E. Kreiger, M. Kreiger, and M. Case, "Print time vs. elapsed time: A temporal analysis of a continuous printing operation for additive constructed concrete," *Additive Manufacturing*, Apr. 2019.
- [16] N. Ashrafi, J. P. Duarte, S. Nazarian, and N. A. Meisel, "Evaluating the relationship between deposition and layer quality in large-scale additive manufacturing of concrete," *Virtual and Physical Prototyping*, vol. 14, no. 2, pp. 135–140, Apr. 2019.
- [17] F. Bos, R. Wolfs, Z. Ahmed, and T. Salet, "Additive manufacturing of concrete in construction: potentials and challenges of 3D concrete printing," *Virtual and Physical Prototyping*, vol. 11, no. 3, pp. 209–225, Jul. 2016.
- [18] I. Perkins and M. Skitmore, "Three-dimensional printing in the construction industry: A review," *International Journal of Construction Management*, vol. 15, no. 1, pp. 1–9, Jan. 2015.

BIOGRAPHY

Jeneé A. Jagoda is a Master's Degree candidate at the Air Force Institute of Technology at Wright-Patterson Air Force Base, Ohio. She graduated from Purdue University in West Lafayette, Indiana in 2015 with a Bachelor of Science in Civil Engineering and commissioned as a Second Lieutenant in the United States Air Force, where she garnered three years of civil engineering work experience before returning to school. She is currently studying Engineering Management with a focus on Construction Management. Her thesis research investigates the viability of 3D-printed construction as an alternative to conventional construction methods.



Earing Prediction of a Cup Drawing Process Based on the Quadratic Hill Yield Function

Toros Arda Aksen¹, Bora Sener², Emre Esener³, Mehmet Firat¹

Abstract

Quadratic Hill yield function is based on the changing of the material's basic parameters depending on the directions. During the rolling operations, Texture effect and plastic anisotropy are appeared on material. Hence, in sheet metal forming processes such as deep drawing, implementing of finite element method according to anisotropic material properties is crucial for accurate solutions.

In this work, after a deep drawing process, thickness strain distributions and the cup height profile were probed using finite element method. Material of the sheet metal was determined as Al2090-T3. MSC.Marc commercial software was used for FEM analyses and shell element type was used for modeling the circular sheet metal blank. In addition, effect of the element density was regarded for simulations. Because of the anisotropy, thickness strain distributions after forming were obtained depending on the rolling direction and transversal direction separately. Cup height profile was also generated after forming process. Results were compared with the experimental results and compatible correlations were obtained.

Keywords: Cup drawing, deep drawing, quadratic Hill yield function, earing profile

1. INTRODUCTION

Deep drawing is a sheet metal forming process which the sheet metals turn into three dimensional products. Especially in automotive industries, deep drawing is a widely used metal forming technique. Currently, developments in computer science and technology, deep drawing and the other sheet metal forming processes can be simulated using FEM. In metal forming technology, anisotropy has an important role in shape design after forming. To perform accurate analysis in FEM, it is important to define the anisotropy and other plasticity parameters.

Yoon et al. [1] investigated thickness strain distribution and cup height profile of 2090-T3 alloy after deep drawing process using non-quadratic Barlat yield functions Yld91 and Yld96. Suitable results were obtained when yield surface translation was taken into account and earing profile was forecasted accurately. Also Yoon et al. [2] in order to obtain more than four ears, investigated the effect of CPB06ex2 and Yld2000-2D yield functions for cup drawing processes. When the evolution of anisotropy was ignored, solutions based on CPB06ex2 yield surface predicted eight ears as obtained according to the experiments. Variety of cup height was better captured when the evolution of anisotropy was taken into account. Also, for AA6011_T4 alloy, it was recorded that the solutions based on Yld2000-2D yield function captured earing shape and ear numbers according to isotropic hardening rule assumption. For AA5042-H2 alloy, solutions based on Yld2000-2D yield function could not estimate the correct ear numbers. Shi et al. [3] proposed finite element model based on the crystal plasticity so as to forecast the earing after deep drawing process for AA3104-H19 alloy. It was recorded that earing was initiated at low strain values and sheet anisotropy was dominated by the plastic deformation on flange.

¹ Sakarya University, Department of Mechanical Engineering, 54187, Esentepe/Sakarya, Turkey.
ardaaksen@sakarya.edu.tr, firot@sakarya.edu.tr

² Yıldız Technical University, Faculty of Mechanical Engineering, 34349, Beşiktaş/İstanbul, Turkey.
borasener84@gmail.com

³ Bilecik Seyh Edebali University, Department of Mechanical Engineering 11210, Gölümbe/Bilecik Turkey.
emre.esener@bilecik.edu.tr

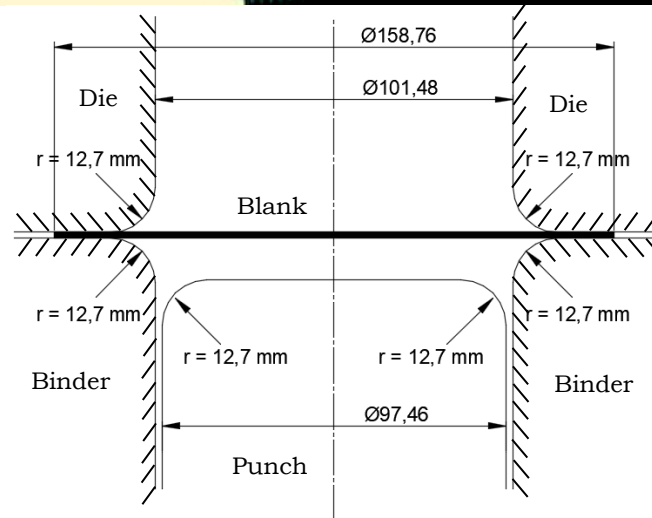


Figure 1. Dimensions of the cup drawing process [1], [4]

The main purpose of this study is to investigate the earing profile and thickness strain distribution during deep drawing process for 2090-T3 alloy. Dimensions of the deep drawing process can be seen in Fig. 1. Mesh structure was generated in Marc commercial program which is a finite element software. To decrease the solution time, quarter model was modeled and element type was determined as reduced integrated shell elements. Anisotropy parameters were obtained from literature studies [1]. To describe the flow curve, Swift's power law was used and flow curve parameters also procured from the literature for 2090-T3 alloy. Element numbers were increased for finer mesh structure and three different mesh structure was generated in order to observe the thickness strain distribution and earing profile. Results were compared with the experimental outcomes obtained also from literature studies.

2. MATERIALS AND METHODS

2.1. Material Characteristics of AA 2090-T3

True stress beyond the yield stress may be expressed as Eq(1) [1].

$$\sigma_{\text{True}} = C \cdot (\varepsilon_0 + \varepsilon_p)^p \quad (1)$$

In expression above, C, p, ε_0 , ε_p are the strength coefficient, hardening exponent, strain value at yielding point and the true plastic strain respectively. ε_p can be calculated according to following equation.

$$\varepsilon_p = \varepsilon_T - \frac{\sigma_{\text{True}}}{E} \quad (2)$$

Mechanical properties of 2090-T3 alloy are obtained from the literature studies and can be seen in Table 1.

Table 1. Mechanical properties of AA 2090-T3 [4], [1]

Parameter	Value
Elasticity Modulus [MPa]	69000
Poisson Ratio	0,33
Strain value at Yield Stress	0,025
Swift Strength Coefficient [MPa]	646
Swift Hardening Exponent	0,227



Parameters in Table 1 are adequate for describing the elastic properties and flow curve of AA 2090-T3 alloy for isotropic material assumption. However, sheet metals exhibit anisotropic behavior. To regard the anisotropy, quadratic Hill yield function was implemented in this study and can be expressed as Eq (3).

$$\varphi^2 = F(\sigma_{yy} - \sigma_{zz})^2 + G(\sigma_{zz} - \sigma_{xx})^2 + H(\sigma_{xx} - \sigma_{yy})^2 + 2L\tau_{yz}^2 + 2M\tau_{zx}^2 + 2N\tau_{xy}^2 - 1 \quad (3)$$

Here F, G, H, L, M, N are the anisotropy constants [5] and can be obtained from the uniaxial tensile tests conducted for rolling, diagonal and transverse directions [6]. Under plane stress conditions, Hill's yield function can be expressed as Eq. (4) [6], [7].

$$\varphi^2 = (G + H)\sigma_{xx}^2 - 2H\sigma_{xx}\sigma_{yy} + (F + H)\sigma_{yy}^2 + 2N\sigma_{xy}^2 - 1 \quad (4)$$

In sheet metal forming, the anisotropy coefficient r has an important role for describing the thinning of the sheet metal and can be defined as Eq. (5).

$$r = \frac{\varepsilon_w}{\varepsilon_t} \quad (5)$$

Anisotropy coefficient varies depending on the direction. r values can be expressed as r_0 , r_{45} and r_{90} for rolling direction, diagonal direction and transversal direction respectively and called as Lankford's anisotropy coefficients. F, G, H, N anisotropy constants can be calculated in terms of Lankford's parameters as it seen in Eq (6), Eq (7), Eq(8) and Eq (9) respectively.[6], [7].

$$F = \frac{r_0}{r_{90}(1+r_0)} \quad (6)$$

$$G = \frac{1}{1+r_0} \quad (7)$$

$$H = \frac{r_0}{1+r_0} \quad (8)$$

$$N = \frac{(r_0+r_{90})(1+2r_{45})}{2r_{90}(1+r_0)} \quad (9)$$

Due to the anisotropy, yield stress changes depending on the direction also. To define quadratic Hill yield function, yield stresses at 0° , 45° and 90° from rolling direction and r values should be determined properly. In this study, Lankford's anisotropy coefficients and the yield stresses for 0° , 45° and 90° from rolling direction were obtained from literature studies and can be shown in Table 2.

Table 2. Yield stress ratios and Lankford's anisotropy parameters of AA 2090-T3 alloy [1], [4], [8]

	σ_0/σ_0	σ_{45}/σ_0	σ_{90}/σ_0	r_0	r_{45}	r_{90}
AA 2090-T3	1	0,811	0,910	0,21	1,58	0,69

Utilizing the normality rule, the associated plastic strain increment can be calculated according to the following expression [1].

$$\Delta\varepsilon_{ij}^p = \gamma \frac{\partial \varphi}{\partial \sigma_{ij}} \quad (10)$$

Here γ is the plastic multiplier and φ is the plastic potential.

2.2. Mesh Structure and Boundary Conditions

In this work, circular blank model was created in Marc software. So as to minimize the solution time, quarter model was generated in Marc software. Model consists of shell reduced integrated elements. Linear reduced integrated shell elements contain 4 nodes at the corners and integration point at the centroid as it shown in Fig. 2.

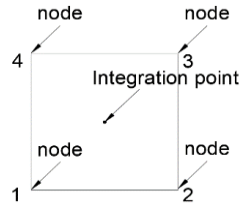


Figure 2. Reduced integrated element in two dimension

Three different mesh structures were generated for capturing the effect of the mesh density. First, the model containing 20 elements in circumferential direction was generated as it seen in Fig. 3, then the element numbers were updated in circumferential direction as 30 and 40 elements respectively. Thickness was assigned as 1,6 mm.

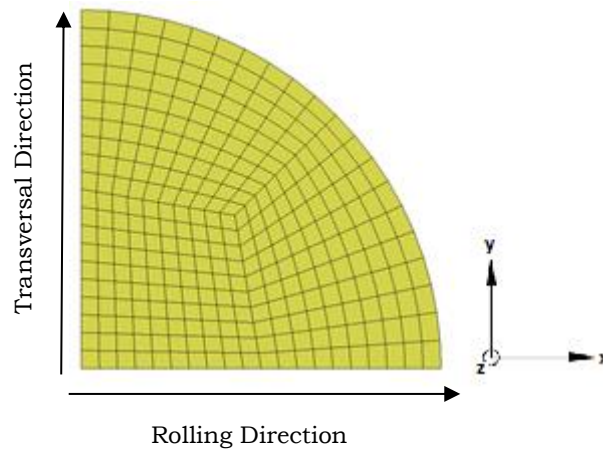


Figure 3. Mesh structure of the quarter model of the circular blank model (20 elements in circumferential direction)

Binder force was applied on quarter blank as 5,55 kN and friction coefficients are assigned as 0,1 for all contact interactions [1], [8]. Binder, punch and die were modeled as geometric non-deformable surfaces. Symmetry boundary conditions on the quarter model can be seen in Fig. 4.

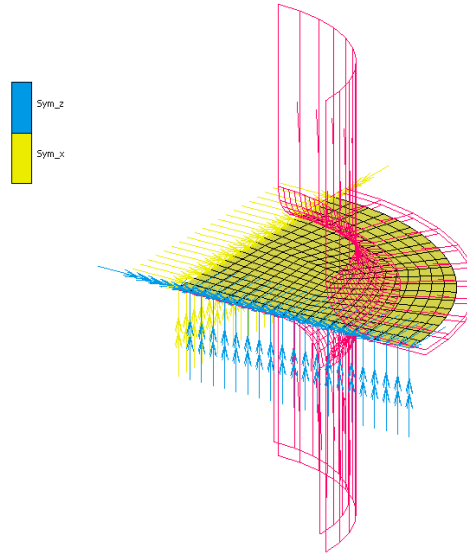


Figure 4. Boundary conditions of quarter model containing 20 elements in circumferential direction

Analyses were fulfilled independent from the rate effect. Thickness strain distributions for rolling direction and transversal direction were obtained after forming simulations. Shell layer numbers were assigned as 5, 7 and 9 respectively and simulations were repeated. For every simulation, cup height profiles were observed. Analysis results were compared with the experimental results.

3. RESULTS AND DISCUSSION

For all simulations, punch motions were realized in z directions. Anisotropy parameters related to Hill yield function were calculated through Lankford's anisotropy coefficients and can be seen in Table 3.

Table 3. Anisotropy parameters of quadratic Hill yield function for AA 2090-T3 alloy

	F	G	H	N
AA 2090-T3	0,2515	0,8264	0,1734	2,242

As a sample, thickness distribution after forming process can be seen in Fig. 5, for 40 elements in circumferential direction. Analyses were performed according to models containing 20, 30 elements in circumferential direction and 5,7 and 9 layers in thickness direction for element formulations separately.

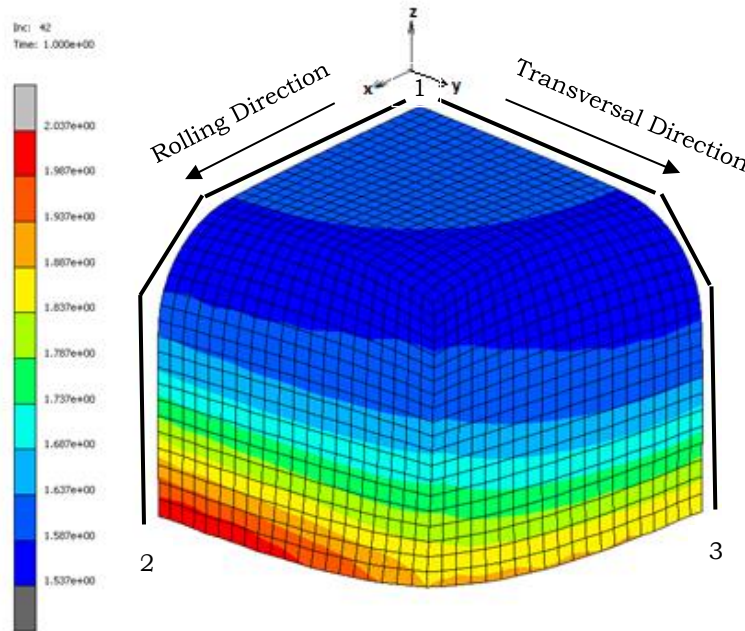
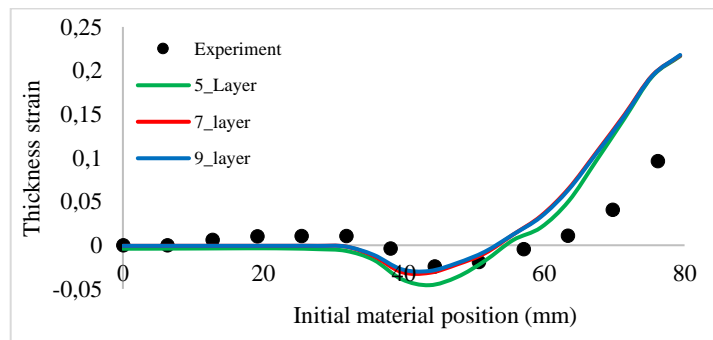


Figure 5. Thickness distribution after cup drawing process for model containing 40 elements in circumferential direction

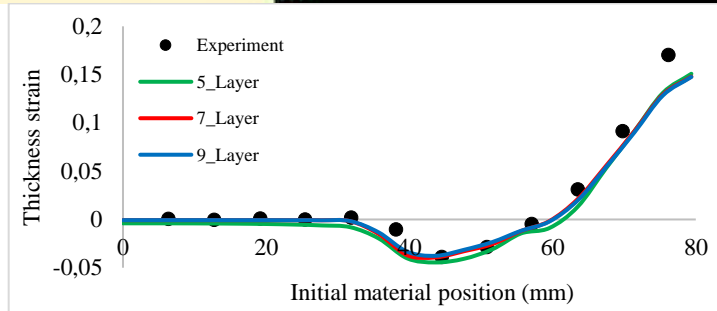
Thickness strain may be calculated according to the Eq. (11).

$$\epsilon_t = \ln \left(\frac{t}{t_0} \right) \tag{11}$$

Gage lines of thickness strain distributions were designated between points 1,2 and 1,3 for rolling direction and transversal direction respectively. Thickness strain distributions of cup drawing process depending on the layer numbers in thickness direction can be seen in Fig. 6, Fig. 7 and Fig. 8 for the models which contains 20, 30 and 40 elements respectively in circumferential direction. Also thickness strain distributions for rolling direction and transversal direction can be seen for every simulation in Fig. 6, Fig. 7 and Fig. 8 separately. Results were compared with the experimental outcomes attained from the literature studies [1], [4].

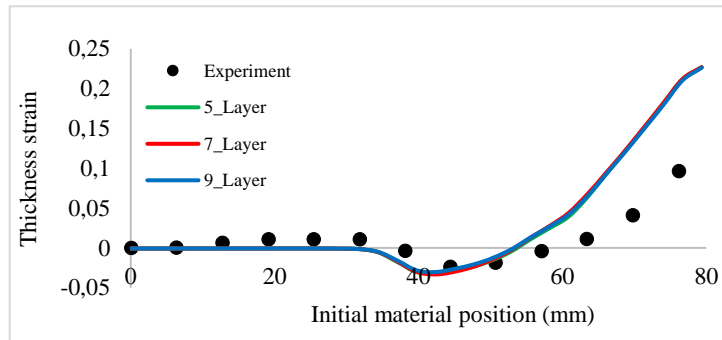


a)

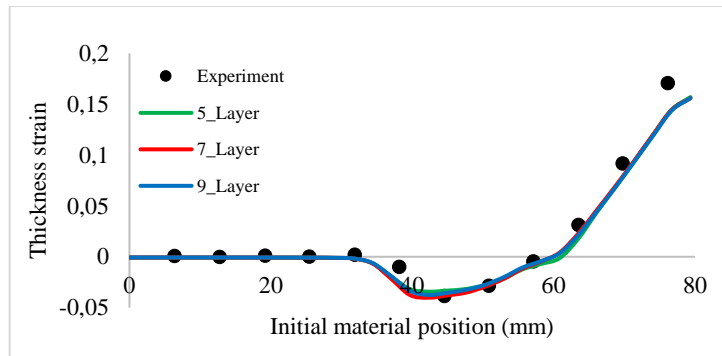


b)

Figure 6. Thickness strain distributions after forming a) in rolling direction, b) in transversal direction (20 elements in circumferential direction)

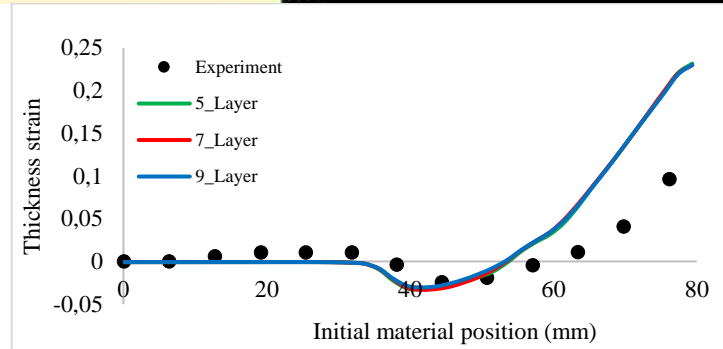


a)

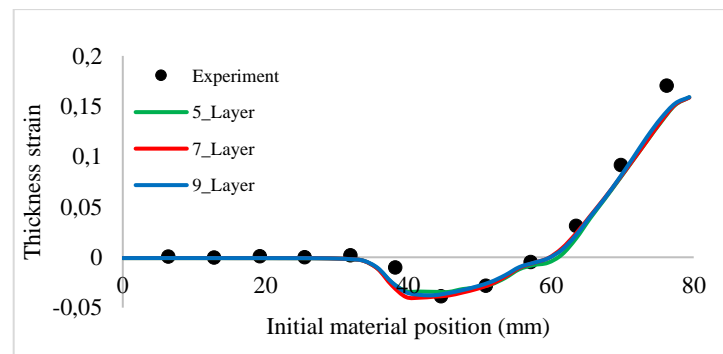


b)

Figure 7. Thickness strain distributions after forming a) in rolling direction, b) in transversal direction (30 elements in circumferential direction)



a)



b)

Figure 8. Thickness strain distributions after forming a) in rolling direction, b) in transversal direction (40 elements in circumferential direction)

As it seen in Fig. 6-8, similar results were obtained for different layer numbers in shell elements. Thickness strain values in rolling directions were diverged from the experimental values but thickness strain values in transversal directions were captured successfully. In general, outcomes attained from different element densities and different layer numbers were coherent with each other. Element numbers did not affect the results dramatically but best correlations were obtained using 40 elements in circumferential direction. For transversal direction, thickness values were predicted accurately. Earing profile after cup drawing process can be seen in Fig. 9 for the model consisting of 40 elements in circumferential direction.

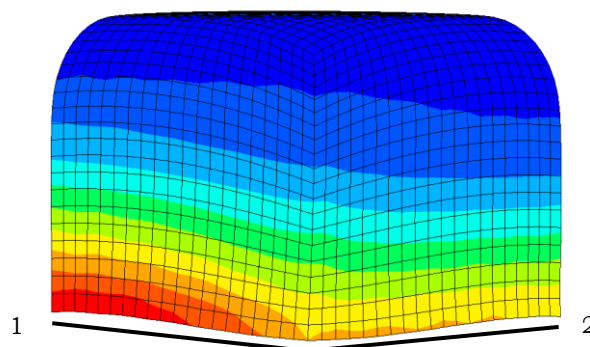


Figure 9. Earing profile after cup drawing process (40 elements in circumferential direction)

In order to determine the cup height values, path plot was generated from point 1 and point 2 as it seen in Fig. 10. Due to the fact that the model was created as quarter model, cup height values were obtained and generated until 90° from rolling direction. Cup height values according to the circumferential element numbers can be shown in Fig. 10. Simulation results were compared with the experimental outcomes obtained from the literature studies [1].

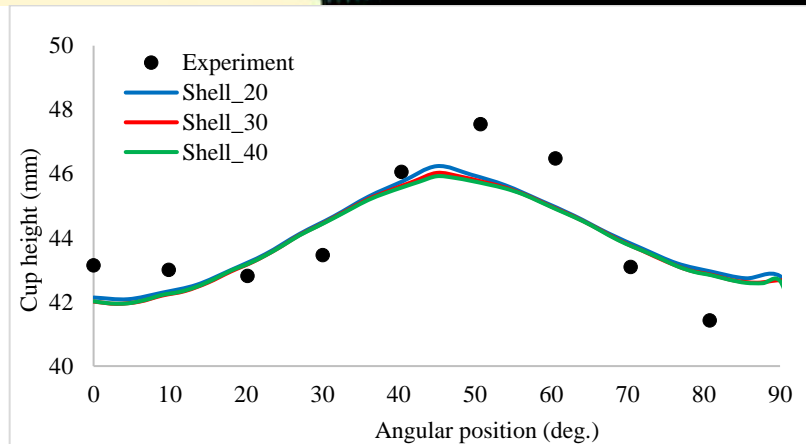


Figure 10. Cup height values after cup drawing process

4. CONCLUSION

In this study, analyses of deep drawing process were performed using finite element method. Material of the circular blank was determined as AA 2090-T3 and the blank was modeled through shell elements consisting of 5, 7 and 9 layers in thickness direction respectively. To regard the anisotropy of the material, quadratic Hill yield function was implemented to the material model. First, coarser mesh structure was generated and analyses were performed. Then the element density of the mesh structure was increased and the analyses were repeated. Along with the thickness strain distributions, earing profile were investigated after forming processes.

According to the simulation results, thickness strain distributions were obtained and compared with the experimental results. In transversal direction, simulation results were matched with the experimental data. In the other hand, results considering the quadratic Hill yield function were inadequate for capturing the thickness strain distributions in rolling direction. Cup height profiles were also plotted and compared with the experiments. Results were diverged from the experiments but compatible outcomes were obtained. In general, Results regarding Hill yield function were insufficient for capturing the experimental data.

In future works, material models containing the yield surface translation can be implemented and another sophisticated material models can be used for sheet metal forming simulations. Especially, to predict the earing profile, material models containing additional anisotropy parameters for yield surface or combined hardening plasticity can provide better correlations.

REFERENCES

- [1]. J. W. Yoon, F. Barlat, K. Chung, F. Pourboghra, D. Y. Tang, "Earing predictions based on asymmetric nonquadratic yield function," *International Journal of Plasticity*, vol 16, pp. 1075-1104, 2000.
- [2]. J. H. Yoon, o. Cacazu, J. W. Yoon, R. E. Dick, "Earing predictions for strongly textured aluminum sheets," *International Journal of Mechanical Sciences*, vol 52, pp. 1563-1578, 2010.
- [3]. Y. Shi, H. Jin, P. D. Wu, "Analysis of cup earing for AA3104-H19 aluminum alloy sheet," *European Journal of Mechanics / A Solids*, vol 69, pp. 1-11, 2018.
- [4]. S. C. Soare, "On the use of homogeneous polynomials to develop anisotropic yield functions with applications to sheet forming," PhD Dissertation, Department of Mech. and Aerospace Engineering, Florida, U.S.A, 2007.
- [5]. G. E. Dieter, *Mechanical Metalurgy*, SI metric ed., United Kingdom, 1988.
- [6]. M. Firat, B. Kaftanoglu, O. Eser, "Sheet metal forming analyses with an emphasis on the springback deformation," *Journal of Materials Processing Technology*, vol 196, pp. 135-148, 2008.
- [7]. M. Firat, "A numerical analysis of sheet metal formability for automotive stamping applications," *Computational Materials Science*, vol 43, pp. 802-811, 2008.
- [8]. J. W. Yoon, F. Barlat, R. E. Dick, M. E. Karabin, "Prediction of six or eight ears in a drawn cup based on a new anisotropic yield function," *International Journal of Plasticity*, vol 22, pp. 174-193, 2006.



The Metrics to Measure and Evaluate Software Developers' Performance

Kokten Ulas Birant¹, Mustafa Batar²

Abstract

Up to now, several metrics have been determined and arisen in order to measure and evaluate software developers' performance: Productivity, Engagement, Attention to Quality, Code Based Knowledge, Skills and Management, Adherence to Coding General Structure and Techniques, Learning and Skills, Personal Responsibility, etc. However, there is not any universally accepted a set of metrics or a methodology to measure and evaluate software developers' performance. Three main reasons of this situation which may be thought; Firstly, each part of software creation is unique. There is no compelling reason to assemble two times the same parts of software as it might be duplicated by copying it. This makes it truly difficult to make a formal and thorough correlation between two parts of software based on both qualitative and quantitative approach. Secondly, the current technology is something that changes at a truly fast pace (phase). So, as a natural result of this situation, each time a methodology in respect to a certain wave of technology or technology-based metrics is dependable enough, it is for the most part as of recently old and obsolescence in time. Thirdly, there is a gigantic zone for innovativeness in discovering the diverse answers for a unique issue. For instance, calculating coding lines that software developers write for the same problem means size of the solution, not the problem. This case shows us difficulty of turning or converting tangible data to the metric in software developers' performance. In this study, the researches, which have been done before about performance criteria, and the case studies, which have been published before about performance criteria, have been observed, analyzed and evaluated (in total 18 separate research and study). In the light of these consequences, a measurement and evaluation criteria set about the software developers' performance have been created and centered into "Software Engineering".

Keywords: Software Engineering, Software Developers, Performance

1. INTRODUCTION

"Measurement" means the digits, numbers, questions or intermediaries that some standards and related rules specify or disclose. The numbers alone are not meaningful, so they don't make sense alone. Numbers are values that have a quantitative importance and value, such as weight and height, and are also considered to be open to investigation. Markers with the ability to allocate and analyse variables are the most critical part of the estimation, because weak principles reveal empty results. Ideas are generally not accurately measured or predictable, so with generally use of "speed", "justification", "verbal ability", "written ability" and etc., some results are tried to be inferred, and also, a number of results are obtained by using these markers. [1] The following Fig. 1 describes what the measurement process is like and shows which of the following steps has reached a certain and a clear conclusion:

Real Life Cases → Criteria belonging These Cases → Measurement of These Criteria → Numerical Value of This Measurement → Try & Feed-Back → Formulation

Figure 15. Steps of Measurement

¹ Corresponding author: Dokuz Eylül University, Department of Computer Engineering, 35390, Izmir, Turkey. ulas@cs.deu.edu.tr

² Dokuz Eylül University, The Graduate School of Natural and Applied Sciences, 35390, Izmir, Turkey. mbatar@cs.deu.edu.tr



“Evaluation” is the process of collecting data in a methodical manner about the qualifications, studies and results of administrations or projects to evaluate the degree of achievement of the objectives-objectives, to recognize the necessary changes or to decide on the choices related to future programming (planning). [2]

“Evaluation” differs from “determining” and “appraisal”: it examines data on the procedure of the social matter and the current state of a characterized people or geographic region and unmet management needs. In conjunction with the “CARE Act”, it is a form of management that needs to address the needs of individuals living with HIV/AIDS (those who take into consideration and those not taken into consideration). [2]

“Evaluation” differs from “monitoring”: project execution is a continuous methodology of monitoring and reporting the consumption of regulatory exercises and management suppliers. The control methodology effectively controls the standard audits of each management supplier’s progress in terms and conditions of satisfactory terms, the distinctive evidence of the remedial action areas and the effective restoration of the restorative activities. [2]

“Evaluation” differs from “research”: this is the procedure for social tutelage data for new learning, hypothesis testing or realization. The main role of the research is to increase or teach administrative competence rather than expanding the learning group in a field or making recommendations. [2]

“Evaluation” differs from “improvement”: a methodology; continuity, including those authorized to control and evaluate inputs (staff time, consumables, etc.), forms (courses delivered by administrations), efficiency (number of management units transmitted) and permanent increase of results. [2]

This study has been prepared and written based on the findings of 17 articles with SCI-indexed published since 1998 and information obtained from a master’s thesis in 2008.

2. CRITERIA RESEARCH

In his study, Gallivan showed the relationship between the job and the professional profession related to the measurement and evaluation of the performance of software developers: satisfaction and difficulty, the actual (active) performance, technical knowledge of the profession, analytical thinking skills, verbal skills, work habits, new ideas and creativity to open and revealed various special points. (18 significant criteria have been determined.) [3]

Sawyer and Guinan have shown several points to work as a software development team to measure and evaluate the performance of software developers. These issues have been team support, team loyalty, team vision, team personalities, team meeting, team members and team leader. In addition, they have tried to find answers to some questions about software development. These questions; software development method, code retention, code library, working time and related to software development documentation. (44 significant criteria have been determined.) [4]

Hall, Wilson, Rainer and Jagielska have tried to find answers to a few questions about a few issues related to the measurement and evaluation of software developers’ performance. These questions have been related to software team, software project, business life, work and personality. (26 significant criteria have been determined.) [5]

In measuring and evaluating the performance of software developers, Baggelaar emphasized the importance of several points in the master’s thesis. These important points have been abstraction, testability, coupling, modularity, templates, test coverage, error handling and exceptional case use. In addition, software developers have tried to find out the effect of code and comment line numbers in measuring and evaluating their performance. (22 significant criteria have been determined.) [6]

Lee, Joshi and Kim have analyzed and evaluated software developers’ performances in terms of personality and work habits. (12 significant criteria have been determined.) [7]

Thing was interested in and focused on the issues of personality, working style, workload and software development process in measuring and evaluating the performance of software developers. (14 significant criteria have been determined.) [8]

Zhang, Wang and Xiao first asked a few questions for their work and received some answers about software developers’ performance measurement and evaluation. These questions have been number of lines of code, number of comment lines, number of classes, number of samples, class relation, number of method (methods),



degree of heritability depth and software development issues related to the difficulty. (13 significant criteria have been determined.) [9]

Calikli and Bener provided a general overview of the performance measurement and evaluation of software developers. In their work, they showed the effect of software developers' level of education and some points and issues in the field of software development (satisfaction level, confidence level, work experience, etc.) on software development process. (4 significant criteria have been determined.) [10]

Chilton, Hardgrave and Armstrong have put forward several points for software developers to measure and evaluate their performance during work days. These points have been work-life, working habits, personality, age and gender. (22 significant criteria have been determined.) [11]

Ramler, Klammer and Natschläger have tried to research and find answers to some questions about software quality in measuring and evaluating the performance of software developers. (3 significant criteria have been determined.) [12]

Wang and Zhang highlighted a number of important issues in the measurement and evaluation of software developers' performance. These points have been work-life, work experience, workload, education level and gender. (14 significant criteria have been determined.) [13]

In their study, Baljepally, Nerur and Mahapatra tried to find answers of many questions related to personality traits in measuring and evaluating the performance of software developers. (8 significant criteria have been determined.) [14]

Duarte, Faria and Raza have tried to find out the effects of various issues in measuring and evaluating the performance of software developers. These issues have been timing error, size error, segmentation error, missing parts, unrelated parts, number of errors and the number of unit tests. (10 significant criteria have been determined.) [15]

Ehrlich and Cataldo discussed some aspects of software development in order to measure and evaluate the performance of software developers in their work. These issues have been team leader, team coordination, company management, company employees and private life. (10 significant criteria have been determined.) [16]

Kelly and Haddad have tried to find out the extent to how "error" has an impact on software developers' performance measurement and evaluation. (3 significant criteria have been determined.) [17]

Schroter, Aranda, Damian and Kwan have tried to answer various questions in the minds about of software developers about measuring and evaluating their performance. These questions have been related to the number of constructs, code changes, method (method) number, fixed code parts, work-life, work quality, team leader, software project documents and software development tool. (22 significant criteria have been determined.) [18]

Westermann emphasized the importance of certain points in the software development process. Reliable code writing has been investigated about the impact of software project outputs and work style on measuring and evaluating the performance of software developers. (7 significant criteria have been determined.) [19]

Calikli and Bener have shown some important points in measuring and evaluating the performance of software developers. These points; software project development plan and software team psychology. (4 significant criteria have been determined.) [20]

3. CRITERIA TO EVALUATE SOFTWARE DEVELOPERS

In the light of the 17 SCI indexed article findings and the success of the master's degree successfully completed in 2008, some criteria have been considered for measuring and evaluating the performance of software developers. As a result of our research, the 8 criteria have been found to be "key value" and have been listed below and explained why each should be a benchmark.

Using any pre-determined model or method in the software development process: While developing a software project, it means benefiting from the models and methods that have been previously used, tested and operated by some employees. [4]

In their study, Sawyer and Guinan showed that while the software has been being developed, the business has had a product or a production dimension as well as the social dimension of the business (software developers, project team, stakeholders, customers, etc.). Both the software (product) in terms of quality as well as the



efficiency of team work (social dimension) in terms of the use of tools such as models or methods have been found to be effective in the software development process. They found that the use of these tools increased the quality of the product by up to 25%, and they showed that the social relationship between the software team and the customers became more positive due to this quality work. The fact that this material has such a multidimensional effect shows us that it should be one of the main developers' measurement and evaluation criteria. [4]

Dependent on any software development method in the software development process: When developing the software project, the software development process under the main headings such as "heavy-weight" or "light-weight" is put into a specific plan. The use of one or more of the methods means benefiting from these. [4]

In the connection with the previous criterion, depending on the method of software development, based on it, as a natural consequence of this, the concept of reusability-applicability emerges and this allows the use of tools such as the previously developed model or method. Thanks to this opportunity, it has been seen that the quality of the software has increased by up to 25%. This data has emerged in the light of the results of the work of 40 software development teams developing products with commercial-financial value. This concrete, tangible result shows us that this matter should be one of the basic developers' measurement and evaluation metrics. [4]

Whether developed software makes it easier for customers to do their job or not: A software is developed based on the customer's wishes and requirements is expected to facilitate the solution of the existing problem. If it makes the work done earlier more complicated, the effectiveness of the software produced has to be questioned. [8]

In this study of Thing, a formula based on the concept of function point was created in order to measure and evaluate the performance of the software developer. It is concluded that this special formula based on mathematics gives an objective result with general validity which is tried for a predetermined situation and coincides with the nature of science. As a result of this general assessment and evaluation, the concept of quality has been dealt with and it is seen that the most influential factor is based on customer (customer requirements, requirements, degree of satisfaction, accessibility, etc.). Since the main goal of the software development process is to produce quality software, this matter should be mainly a criterion based on the developers' measurement and evaluation. [8]

In the software development process, to do the process of erroneous, exceptional situation: software development process in the coding part of the program when writing, "error handling" and "exception handling" are expected to be used; otherwise, the developed program will produce erroneous results in the test section, meaning that it will collapse, and as a result, the desired product will not emerge. [6]

In this master's thesis, Baggelaar emphasized the importance of "sustainability", "robustness" and "testability" concepts for the product that emerged as a result of software development process and showed it to us. In order to achieve the goal of "robustness", he emphasized the concept of "defense". It is based on two key elements to successfully achieve and present this concept: dealing with errors and dealing with exceptional situations. It is inevitable that this matter, which is effective in the emergence of the concept of "defense" and indirectly contributes to the development of "robust software", is one of the basic developers' performance measurement and evaluation criteria. [6]

Whether the developed software has good quality or not: The essential aim of the software development process is producing and developing qualified software, which is the sine qua non of the "Software Engineering". [12] [14]

In both of these studies, software (product) quality was taken as a basis in software development process. In Balijepally, Nerur and Mahapatra studies, a model (hypothesis) based on mathematical background related to the mental and psychological states of software developers was revealed. They tried these hypotheses in a controlled way and realized that the concept of quality should be included in the model as the main element. Because the quality affects both the working styles and performances of the developers and mentally changes their moods and draws them positively-positively. Ramler, Klammer and Natschläger in their study, in the process of software development, the error is to make no mistake, the code without error, and if a mistake has been made, it should be done immediately to repair and repair-correcting the error. They also showed that the quality assurance of a software product with no error was more concrete, more tangible and more accurate. In the light of these two studies, it has been proved that the aim-target quality in the software development process should be one of the main developers' performance measurement and evaluation metrics. [12] [14]



In the software development process, pay attention to the concept of “re-usability”: As in other projects rather than software, it is inevitable to use some modules, some functions or some structures previously created in developing software projects, and this is in fact a facilitating feature. The higher the concept of re-usability, the lower the cost of the software development process. [8]

In his study, Thing designed, created and developed a mathematical formula based on the function point mechanism that measures and evaluates the performance of software developers in the software development process. It is concluded that this particular formula has been tried and general-validated for a specific case that has already been determined. There are 14 different substances in this formula, and one of the most influential ones is the ease of the concept of “re-usability”. The main purpose of this formula is to reveal the software (product) quality assurance in a concrete way in the light of measuring and evaluating the developer performance. This shows us that the concept of “re-applicability” indirectly, even if not directly. It affects the concept of software quality which is one of the main elements of software engineering. The substance with such an effect should be one of the main developers’ performance measurement and evaluation criteria. [8]

To develop reliable/secure code while developing software: In order to ensure reliable operation of the product that will be produced during the software development process and to give the desired results, it requires the reliable writing of the program of the software, which means that the codes of the program are developed according to the reliable structure. [19]

In this study of Westermann, the importance of 7 conditions, more precisely 7 features, is emphasized in the software development process. These concepts are “simplicity”, “goal-oriented”, “reliability”, “adaptability”, “accuracy”, “practicality” and “efficiency”. These properties have been shown to directly or indirectly affect the quality of the software developed. Among these elements, the concept of plan righteousness-rigor comes to the fore. In the light of the main parameters, it is stated that it is possible to write function, method, module or procedure based code and to provide reliable code writing. It has been shown that the true feature of the software (product) as well as being correct and the “reliability” feature of the software (product) are closely related with the trust based code writing. It is inevitable that this substance having such a multi-faceted effect and relationship is one of the basic developers’ performance measurement and evaluation criteria. [19]

Whether the developed software is understandable and usable or not: The developed software must be able to be used in a practical way by customers to produce solutions to existing problems; for this to be effective, the product in hand is understandable and therefore should be usable. [3]

In this study, Gallivan conducted a survey on creativity, authenticity and practical (understandable & available) product development with 200 software developers working in 2 different software companies. As a result of this study, it was seen that customer based study positively-positively affected the performance of the developer. This effect, which has a positive effect on performance, shows us that it should be one of the main developers’ performance measurement and evaluation metrics. [3]

4. CONCLUSION

The criteria for the measurement and evaluation of the performance of the software developers, which are the result of our research and which are taken into consideration as a result of our analyses: software development process by relying on a specific method, taking care of reliable code writing, using tried and tested models, developing a product that is understandable and error-free by focusing on problem solving and, of course, as a result of which is an important point for software engineering. It shows us that the gold of the concept must be filled with concrete data. As a result of this evaluation, the more effective and more efficient use of human power, which is the main source of software development process, will have been ensured and the concept of “Software Engineering” will have been filled with a little bit more and this concept will have become more tangible.

REFERENCES

- [1]. R.S. Michael, “Measurement”, http://www.indiana.edu/~educy520/sec5982/week_3/measurement_rsm.pdf, 2008.
- [2]. “What is evaluation?”, <ftp://ftp.hrsa.gov/hab/m4p1.pdf>, 2015.
- [3]. M.J. Gallivan, “The influence of system developers’ creative style on their attitudes toward and assimilation of a software process innovation”, Proceedings of the Thirty-First Hawaii International Conference on System Sciences, IEEE, 1998, pp 435-444.
- [4]. S. Sawyer and P. J. Guinan, “Software development: Processes and performance”, IBM Systems Journal, IEEE, 37, 1998, pp 552-569.



- [5]. T. Hall, D. Wilson, A. Rainer and D. Jagielska, "The neglected technical skill?", Proceedings of the 2007 ACM SIGMIS CPR Conference on Computer Personnel Research: The Global Information Technology Workforce, 2007, pp 196-202.
- [6]. H. Baggelaar, "Evaluating programmer performance visualizing the impact of programmers on project goals", Amsterdam, University of Amsterdam, 2008.
- [7]. K. Lee, K. Joshi and Y. Kim, "Person-job fit as a moderator of the relationship between emotional intelligence and job performance", Proceedings of the 2008 ACM SIGMIS CPR Conference on Computer Personnel Doctoral Consortium and Research, 2008, pp 70-75.
- [8]. C. Thing, 'The application of the function point analysis in software developers' performance evaluation', 4th International Conference on Wireless Communications, Networking and Mobile Computing, IEEE, 2008, pp 1-4.
- [9]. S. Zhang, Y. Wang and J. Xiao, "Mining individual performance indicators in collaborative development using software repositories", 15th Asia-Pacific Software Engineering Conference, IEEE, 2008, pp 247-254.
- [10]. G. Calikli and A. Bener, "Empirical analyses of the factors affecting confirmation bias and the effects of confirmation bias on software developer/tester performance", Proceedings of the 6th International Conference on Predictive Models in Software Engineering, ACM, 2010, Article No. 10.
- [11]. M. A. Chilton, B. C. Hardgrave and D. J. Armstrong, "Performance and strain levels of it workers engaged in rapidly changing environments: A person-job fit perspective", ACM SIGMIS, 2010, pp 8-35.
- [12]. R. Ramler, C. Klammer and T. Natschläger, "The usual suspects: A case study on delivered defects per developer", Proceedings of the 2010 ACM-IEEE International Symposium on Empirical Software Engineering and Measurement, 2010, Article No. 48.
- [13]. Y. Wang and M. Zhang, "Penalty policies in professional software development practice: A multi-method field study", Proceedings of the 32nd ACM/IEEE International Conference on Software Engineering, 2010, pp 39-47.
- [14]. V. Balijepally, S. Nerur and R. Mahapatra, "Effect of task mental models on software developer's performance: An experimental investigation", 45th Hawaii International Conference on System Science, IEEE, 2012, pp 5442-5451.
- [15]. C. B. Duarte, J. P. Faria and M. Raza, "PSP PAIR: Automated personal software process performance analysis and improvement recommendation", Eighth International Conference on the Quality of Information and Communications Technology, IEEE, 2012, pp 131-136.
- [16]. K. Ehrlich and M. Cataldo "All-for-one and one-for-all?: A multi-level analysis of communication patterns and individual performance in geographically distributed software development", Proceedings of the ACM 2012 Conference on Computer Supported Cooperative Work, 2012, pp 945- 954.
- [17]. B. Kelly and H. M. Haddad, "Metric techniques for maintenance programmers in a maintenance ticket environment", Journal of Computing Sciences in Colleges, ACM, 28, 2012, pp 170-178.
- [18]. A. Schroter, J. Aranda, D. Damian and I. Kwan, "To talk or not to talk: Factors that influence communication around changesets", Proceedings of the ACM 2012 Conference on Computer Supported Cooperative Work, 2012, pp 1317-1326.
- [19]. D. Westermann, "A generic methodology to derive domain-specific performance feedback for developers", 34th International Conference on Software Engineering, IEEE, 2012, pp 1527-1530.
- [20]. G. Calikli and A. Bener, "An algorithmic approach to missing data problem in modeling human aspects in software development", Proceedings of the 9th International Conference on Predictive Models in Software Engineering, ACM, 2013, Article No. 10.



EMIC: An Ensemble Approach for Improving Multi-Instance Classification

Kokten Ulas Birant¹, Pelin Yildirim Taser², Derya Birant³

Abstract

Multi-instance classification is a supervised learning technique which aims to predict the labels of the bags that consists of unlabeled instances with multi-feature vectors. In the last decade, ensemble learning has become one of the most popular machine learning methods since it generally provides more accurate classification results than the individual classifiers. Considering this motivation, the study presented in this paper combines these two techniques to benefit from their capabilities together. This paper proposes an ensemble-based multi-instance classification (EMIC) approach which combines a set of individual multi-instance classifiers to obtain final class label using a voting mechanism. This study also compares the suggested EMIC approach with the traditional multi-instance classification methods in terms of classification accuracy. In the experimental studies, the EMIC approach was tested on various real-world and well-known multi-instance datasets. The results indicate that the proposed ensemble approach generally achieves higher classification performance than the individual multi-instance classification algorithms.

Keywords: ensemble learning, multi-instance classification, machine learning.

1. INTRODUCTION

Multi-instance classification (MIC) is one of the most important tasks of *multi-instance learning* (MIL) [1] which is a special type of machine learning. In MIC, each training example, called *bag*, contains a variable number of *instances* described by feature vectors. The bag is associated with a single class label, although the individual instances within the bag are not given labels. A bag is classified as positive if it has at least one positive instance; conversely, a bag is classified as negative if all instances in the bag are negative. The objective of MIC is to predict the class label of unseen input bags using a model built from a training set.

Ensemble learning (EL) is a useful machine learning technique where multiple learners are trained and aggregated to solve the same problem. It combines the decisions of several different classifiers with the goal of improving classification performance. Bagging and boosting are two well-known techniques of developing classifier ensembles. *Bagging* is a bootstrap aggregation method that creates and combines multiple classifiers, each of which is trained on a different data partition which is generated by randomly drawing examples from the original training set. *Boosting* is a method for the construction of highly accurate classifier ensembles, where the classifiers are trained iteratively, with the weights on the training instances adjusted adaptively according to the performance of previous classifiers.

This study brings together these two machine learning paradigms: multi-instance classification (MIC) and ensemble learning (EL). It proposes an *ensemble-based multi-instance classification* (EMIC) approach which combines a set of individual multi-instance classifiers to obtain final class label using a voting mechanism. In the study presented in this paper, ensemble-based models of three multi-instance classification algorithms were compared in terms of accuracy: MILR (Multiple Instance Logistic Regression) [2], MITI (Multi-Instance Tree Inducer) [3] and MIRI (Multi Instance Rule Induction) [4]. The usefulness of the proposed approach (EMIC) was confirmed in the experiments conducted on several multi-instance datasets.

¹ Corresponding author: Dokuz Eylül University, Department of Computer Engineering, 35390, Izmir, Turkey. ulas@cs.deu.edu.tr

² Manisa Celal Bayar University, Department of Software Engineering, 45400, Manisa, Turkey. peilin@cs.deu.edu.tr

³ Dokuz Eylül University, Department of Computer Engineering, 35390, Izmir, Turkey. derya@cs.deu.edu.tr



The remainder of this paper is organized into five sections. Section 2 briefly reviews the related work. Section 3 gives background information about multiple instance classification. Furthermore, this section also describes the principle of the proposed approach (EMIC) in detail. Section 4 explains multi-instance datasets used in the experimental studies and presents the results obtained from experiments. Finally, the conclusions and possible future works are given in Section 5.

2. RELATED WORK

Multi-instance classification has received great interest mainly because of its ability to address problems with one to many relationships. Thus, multi-instance classification has been utilized in a broad range of areas such as health [5], education [6], text mining [7], computer security [8] and food industry [9]. Many empirical studies have proven the superiority of multi-instance classification over the traditional one.

Algorithms for multi-instance classification can be grouped into three classes. First, some researchers proposed new algorithms dedicated to the multi-instance (MI) problem such as MIDD (Diverse Density) and its modified version MDD (Modified Diverse Density) [10], MIEMDD (Expectation-Maximization Diverse Density) [11] and TLD (Two-Level Distribution) [12]. Secondly, standard classification algorithms, like k-nearest neighbor, adapted to deal with multi-instance data, including MISVM (Support Vector Machines for multiple-instance learning) [13], MILR (Multiple Instance Logistic Regression) [2], MITI (Multi-Instance Tree Inducer) [3], MIRI (Multi-Instance Rule Induction) [4] that utilizes partial MITI trees, and Citation-kNN (K-Nearest Neighbor) [14]. Thirdly, instead of adapting the algorithm, the data was adapted to turn it into a standard representation, including SimpleMI [15] and MIWrapper [16].

Some researchers have adapted the standard ensemble learning algorithms to address multi-instance classification problem such as MI-Boosting [17] which is the upgraded version of AdaBoost algorithm. Several ensemble approaches have also been proposed to address different MIL problems such as multi-view multi-instance (MVMI) [18], multi-instance multi-label learning (MIML) [19] and extreme learning machine for multi-instance learning (ELM-MIL) [20].

3. MATERIALS AND METHODS

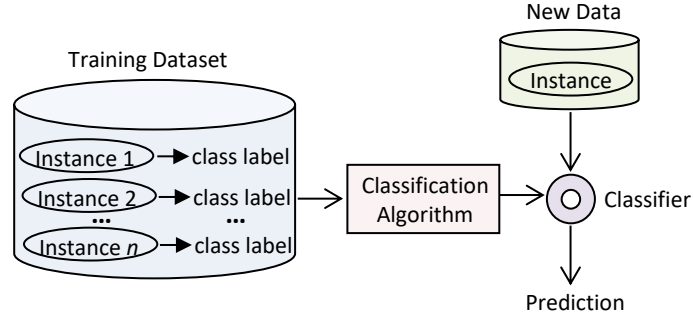
3.1. Multi-Instance Classification

Differently from traditional classification method, a multi-instance (MI) classification algorithm learns an MI dataset which consists of bags of instances, rather than single instances. The number of instances in each bag can be different, and the same instance can belong to different bags.

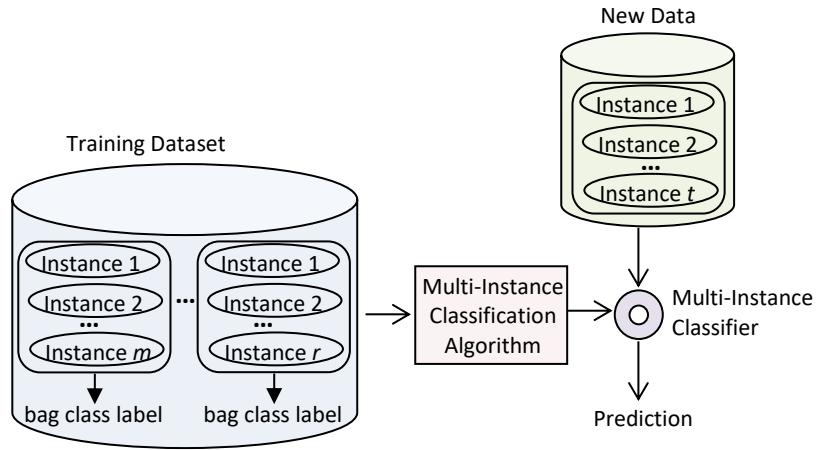
In the *traditional classification*, an instance x is a data point in the feature space X such that $X = \{x_1, x_2, \dots, x_n\}$ and $x_i \in X$. The training set D contains a set of pairs of instances and their class labels, which is denoted by $D = \{(x_1, y_1), (x_2, y_2), \dots, (x_n, y_n)\}$, and the class attribute $Y = \{y_1, y_2, \dots, y_n\}$ has k class labels, where $y \in \{c_1, c_2, \dots, c_k\}$ for $i=1, 2, \dots, k$.

In the *multi-instance classification*, a bag B is a set of m instances such that $B = \{x_1, x_2, \dots, x_m\}$ and $x_i \in B$ for $i=1, 2, \dots, m$. Training set D contains a set of bags and their class labels such that $D = \{ \langle B_j, C_j \rangle \}_{j=1}^n$, where C_j is the class label of the bag B_j . For instance, in a two-class classification, the class labels of the bags can be zero or one, i.e. $C_1=0$ and $C_2=1$.

Figure 1 illustrates the difference between multi-instance classification and traditional classification. In the standard classification, class labels are attached to instances and the aim is to predict the class labels of new instances, whereas in multi-instance classification, class labels are attached to bags (a set of instances) and the main purpose is to estimate the class labels of new bags. In this paper, we focus our study on multi-instance classification.



(a) Traditional classification



(b) Multi-instance classification

Figure 1. The difference between multi-instance classification and traditional classification.

3.2. Multi-Instance Classification Algorithms

In this study, three different multi-instance classification algorithms were applied on the datasets: MILR (Multiple Instance Logistic Regression) [2], MITI (Multi-Instance Tree Inducer) [3] and MIRI (Multi-Instance Rule Induction) [4].

MILR (Multiple Instance Logistic Regression): In this algorithm, logistic regression is used to model the conditional probability of the label of each instance in a bag, and then the bag level probability is estimated by using a combining function (i.e. softmax) to combine the posterior probabilities over the instances of the bag.

Given a set of n bags in the training data D such that $D = \{ \langle B_1, C_1 \rangle, \dots, \langle B_n, C_n \rangle \}$. Suppose that, for the i^{th} bag, m instances are obtained. The j^{th} instance of the i^{th} bag is denoted by B_{ij} . For binary classification, $\Pr(C_i = 1 | B_i = \{B_{i1}, B_{i2}, \dots, B_{im}\})$ be the probability that the i^{th} bag is positive, and $\Pr(C_i = 0 | B_i = \{B_{i1}, B_{i2}, \dots, B_{im}\})$ be the probability that it is negative. The instance-level probability with parameters $\theta = (w, b)$ is estimated with the following function:

$$S_{ij} = \Pr(C_{ij} = 1 | B_{ij}) = \frac{1}{1 + e^{-(w \cdot B_{ij} + b)}} \quad (1)$$

where w is a vector of weights associated with the features and b is a bias term.

If a classifier can estimate an equivalent probability $\Pr(C_{ij} = 1 | B_{ij})$ for an instance B_{ij} , we can use a *softmax* function to combine the probabilities of all the instances in a bag and estimate its posterior probability $\Pr(C_i = 1 | B_i)$. The bag-level probability function is:



$$S_i = \Pr(C_i = 1|B_i) = \text{softmax}_\alpha(S_{i1}, \dots, S_{in}) = \frac{\sum_{j=1}^n S_{ij} e^{\alpha S_{ij}}}{\sum_{j=1}^n e^{\alpha S_{ij}}} \quad (2)$$

where α is a constant that determines the extent to which *softmax* approximates a hard max function.

Actually, combining function encodes the multiple instance assumption. Thus, if one of the instances in a bag is very likely to be positive, the combining function highly tends to estimate the class of the bag as positive, as well. Conversely, if an instance is likely to be negative in the bag, it will affect the other instance gradients via the combining function and so the learner will focus on other potentially positive instances in that bag.

MITI (Multi-Instance Tree Inducer): MITI is a simple decision tree learner designed to solve multi-instance classification problems. The algorithm is based on the top-down decision tree approach, similar to the propositional tree inducers such as C4.5, with two key modifications. First, nodes are split in a best-first order. Second, the algorithm focuses on the creation of pure positive leaves and gives higher weights to instances from smaller bags. Once the algorithm has discovered a positive leaf, it disregards all instances of the bags that are associated with this leaf node.

MIRI (Multi-Instance Rule Induction): MIRI yields a compact set of classification rules for multi-instance classification problems. MIRI is an enhanced version of the MITI method. The disadvantage of MITI approach is that it discards instances considered as false positives from partially grown trees without updating the existing tree structure. MIRI avoids this disadvantage by eliminating any possibility of a suboptimal split since the tree is discarded and regrown.

3.3. Ensemble-based Multi-Instance Classification (EMIC)

Although individual classification algorithms can provide valuable information on class separation for a dataset, they are known to be inferior to ensemble classifiers in predictive tasks. *Ensemble learning* is to train multiple weak learners to form a strong classifier to improve predictive accuracy. In the current study, this learning paradigm was applied to the multi-instance classification problem to evaluate whether similar gains in prediction performance can be obtained or not.

This paper presents the application of bagging and boosting ensemble techniques for multi-instance classification problems. Bagging and boosting are two well-known techniques used for generating an ensemble classifier. *Bagging* is the procedure that generates several models from bootstrap samples of the original training data. *Boosting* is the process of iteratively creating multiple unique models by reweighting of the instances in the data during the learning phase. Predictions are then commonly obtained by a voting mechanism. Since the most popular boosting algorithm is adaptive boosting (AdaBoost), in this study, we preferred to use this algorithm.

This paper proposes to build ensembles of multi-instance classifiers to solve multi-instance problems. In the proposed ensemble approach (EMIC), three multi-instance classification algorithms (MILR, MITI and MIRI) are used as base learners for bagging and AdaBoost methods separately.

4. EXPERIMENTAL STUDIES

The experimental studies were carried out to test the differences in ensemble-based performances of multi-instance classification algorithms. We performed experiments with three MI algorithms available in the Weka data mining tool [21], including MILR, MITI and MIRI.

4.1. Dataset Description

In the experimental studies, the proposed approach (EMIC - ensemble-based multi-instance classification) was tested on five multi-instance datasets: musk 1, musk 2, mutagenesis-atoms, mutagenesis-bonds, mutagenesis-chains and trx. The basic characteristics of the datasets are given in Table 1. Brief description about the datasets is given as follows:

Musk datasets: Musk1 and musk2 are two well-known multi-instance datasets that were used to solve drug activity prediction problem. The datasets contain different conformations of the drug molecules. Molecules of the same type but different conformation (or shape) are grouped together in a bag, which has a class label indicating the presence of a musky smell. Here, the goal is to predict whether a molecule smelled musky or not,



based on its type and shape. Musk2 set includes more instances and more molecules than musk 1, however, some molecules are shared between the two datasets.

Mutagenesis datasets: These are another datasets for drug-activity prediction problem that focus on the estimation of the mutagenicity of the molecules. So the aim is to determine whether a molecule is mutagenic or non-mutagenic. Mutagenesis datasets consist of 188 molecules, of which 125 are mutagenic (active) and 63 non-mutagenic (inactive). There are three different types: (i) mutagenesis-atoms where a bag contains all the atoms of a compound molecule, (ii) mutagenesis-bonds where a bag contains all the atom-bond tuples of a compound molecule, and (iii) mutagenesis-chains where a bag contains all the adjacent pairs in bonds of a compound molecule.

Thioredoxin (trx) dataset: This dataset was used for protein identification task. The problem compares the sequences of each protein family and tries to identify new families by examining the structures. In this problem, the aim is to identify whether proteins belonging to the thioredoxin-fold protein superfamily or not. Each protein is represented by a bag and an instance in the bag corresponds to a position in the sequence. Each position is described by properties of the amino acid at that position.

Table 3. Multi-instance classification datasets

Dataset	Number of Instances	Number of Features	Number of Bags			Average Bag Size
			Positive	Negative	Total	
Musk1	476	166	47	45	92	5.17
Musk2	6598	166	39	63	102	64.69
Mutagenesis-atoms	1618	10	125	63	188	8.61
Mutagenesis-bonds	3995	16	125	63	188	21.25
Mutagenesis-chains	5349	24	125	63	188	28.45
Trx	26611	8	25	168	193	137.88

4.2. Experimental Results

The standard multi-instance classification algorithms (MILR, MITI and MIRI) available in the Weka data mining tool [21] were selected as base learners for bagging and boosting ensemble techniques separately. All MIC algorithms were applied by using their default parameters. In Weka, the ensemble size of the bagging and boosting methods are set to 10, an insufficient number based on our prior experience. For this reason, we increased the default iteration number to 100. In each experiment, 10-fold cross validation was performed on the datasets.

Table 2 presents the accuracies of individual and ensemble approaches considered for multi-instance classification. When the average classification accuracies for all used datasets are considered, it is possible to say that, ensemble methods outperform the individual predictors. For instance, AdaBoost(MIRI) (80.78%) and Bagging(MIRI) (82.16%) performed better than the single classifier (79.83%). According to the average results (the last column), bagging method with base learner MIRI was given the best performance among all of the multi-instance classifiers, with an accuracy of 82.16% on average.

Table 2. The comparison of ensemble-based performances of multi-instance classification algorithms in terms of accuracy (%)

Algorithm	Musk1	Musk2	Mutagenesis-atoms	Mutagenesis-bonds	Mutagenesis-chains	Trx	Average
MILR	72.83	80.39	72.34	75.00	78.19	86.53	77.55
AdaBoost(MILR)	76.09	78.43	70.74	78.19	78.19	85.49	77.86
Bagging(MILR)	79.35	77.45	72.34	76.06	81.91	86.01	78.85
MITI	65.22	71.57	81.38	81.38	84.57	32.64	69.46
AdaBoost(MITI)	73.91	70.59	84.04	82.98	84.57	64.77	76.81
Bagging(MITI)	75.00	73.53	83.51	79.79	81.91	40.93	72.45
MIRI	71.74	77.45	81.91	81.91	87.23	78.76	79.83
AdaBoost(MIRI)	72.83	72.55	86.17	84.04	85.64	83.42	80.78
Bagging(MIRI)	76.09	74.51	85.64	82.45	87.23	87.05	82.16

The MIRI method with its bagging variant obtained the best result (87.23%) on the mutagenesis-chains dataset. The accuracy estimates of this method also reached 85.64% on mutagenesis-atoms dataset and 82.45% on mutagenesis-bonds dataset. However, the ensemble version of this method seems not suitable for the musk 2



dataset. A significant improvement occurred on the trx dataset, where accuracy increased from 78.76% to 87.05%. So, ensemble approach achieved a gain of 8%.

The accuracy rates of ensemble-based methods on musk 1 dataset are all significantly better compared with their individual ones. Bagging variant of MILR obtained the best result (79.35%) on this dataset. The AdaBoost algorithm with base learner MITI performed well on the mutagenesis datasets. Its results are all over 82% and they are slightly better than individual MITI method. Especially on the mutagenesis-atoms dataset, the accuracy of AdaBoost(MITI) method (84.04%) is fairly higher than its individual version (81.91%).

Figure 2, 3 and 4 show the ranks of MILR, MITI and MIRI based methods for each dataset respectively. In the ranking method, each method is rated according to its classification accuracy performance on the corresponding dataset. This process is performed by assigning rank 1 to the most accurate method, rank 2 to the second best and so on. Thus, the method with lower rank has better performance than others. In the case of tie, the average ranking is assigned to each method. Compared with ensemble methods, only 3 out of the 18 cases an individual method is ranked as the highest, 16% of all cases. So, ensemble classifiers are most often ranked highest. Bagging and boosting methods have generally good performances since their rank values are generally 1 or 2. MITI is the best performing algorithm, where ensemble methods are always winner.

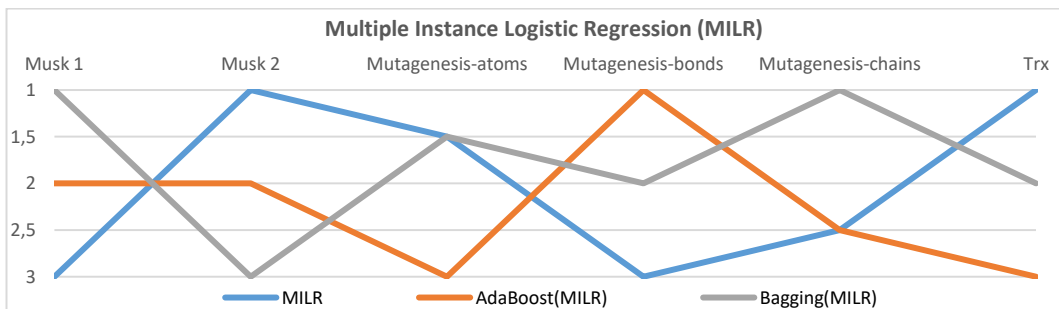


Figure 2. Ranks of MILR based methods for each dataset

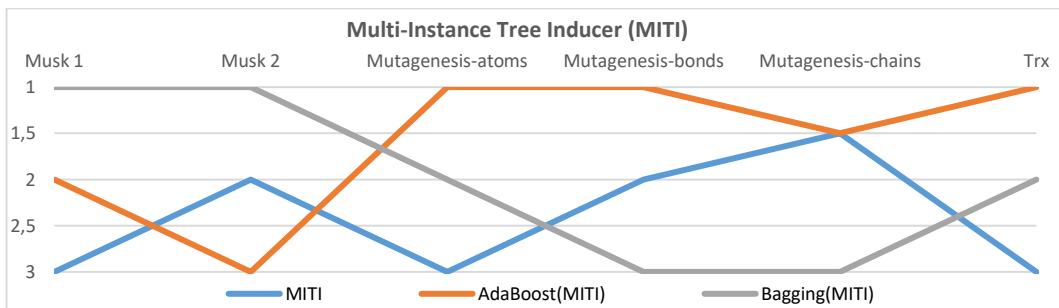


Figure 3. Ranks of MITI based methods for each dataset

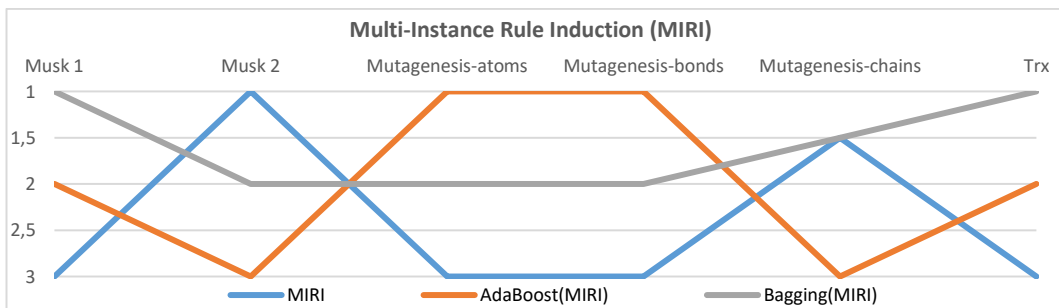


Figure 4. Ranks of MIRI based methods for each dataset



CONCLUSION AND FUTURE WORK

Multi-instance classification (MIC) is the task of predicting class labels for a bag that consists of a number of unlabeled instances. This paper proposes an ensemble-based multi-instance classification (EMIC) approach which combines a set of classifiers to improve accuracy performance. It presents an empirical study of bagging and boosting ensemble techniques for multi-instance classification problems. To show the effectiveness of the proposed approach (EMIC), experimental tests were carried out on real-world multi-instance datasets. Experiments on benchmark datasets show that ensembles of multi-instance classifiers are generally superior to single classifier in solving multi-instance problems. Although the ensemble learning imposes a higher complexity compared to a single classifier, it offers more promising results for multi-instance classification. As future work, instead of using default parameters, the optimal input parameters can be identified for each algorithm and for each dataset. In this way, classification accuracy of the proposed approach (EMIC) can be improved.

REFERENCES

- [1]. S. Vluymans, *Multi-instance Learning*, In: *Dealing with Imbalanced and Weakly Labelled Data in Machine Learning using Fuzzy and Rough Set Methods*. Studies in Computational Intelligence, vol. 807, Cham, Springer, 2019, pp. 131-187.
- [2]. S. Ray and M. Craven, "Supervised versus multiple instance learning: An empirical comparison". In: *Proceeding of the 22d International Conference on Machine Learning*, ACM Press, vol. 22, 2005, pp. 697-704.
- [3]. H. Blockeel, D. Page, and A. Srinivasan, "Multi-instance tree learning", In: *Proceedings of the International Conference on Machine Learning (ICML)*, ACM, 2005, pp. 57-64.
- [4]. L. Bjerring and E. Frank, "Beyond trees: Adopting MITI to learn rules and ensemble classifiers for multi-instance data", In: *Proceedings of the Australasian Joint Conference on Artificial Intelligence*, Springer, 2011, pp 41-50.
- [5]. M. Liu, J. Zhang, E. Adeli, and D. Shen, "Landmark-based deep multi-instance learning for brain disease diagnosis", *Medical Image Analysis*, vol. 43, 2018, pp. 157-168.
- [6]. Y. Ma, C. Cui, X. Nie, G. Yang, K. Shaheed, and Y. Yin, "Pre-course student performance prediction with multi-instance multi-label learning", *Science China Information Sciences*, vol. 62, issue 2, 2019, Article number 29101.
- [7]. H.-J. Song and S.-B. Park, "Identifying intention posts in discussion forums using multi-instance learning and multiple sources transfer learning", *Soft Computing*, vol. 22, issue 24, 2018, pp. 8107-8118.
- [8]. J. Stiborek, T. Pevny, and M. Rehak, "Multiple instance learning for malware classification", *Expert Systems with Applications*, vol. 93, 2018, pp. 346-357.
- [9]. L. Kejriwal, V. Darbari and O.P. Verma, "Multi Instance Multi Label classification of Restaurant Images", In: *Proceedings of IEEE 7th International Advance Computing Conference (IACC 2017)*, Telangana, India, 5-7 January 2017, Article number 7976884, pp. 722-727.
- [10]. O. Maron and T. Lozano-Perez, "A framework for multiple-instance learning", *Advances in Neural Information Processing Systems 10*, The MIT Press, Cambridge, MA, USA, 1998, pp. 570-576.
- [11]. Q. Zhang and S. Goldman, "EM-DD: An improved multiple-instance learning technique", *Advances in Neural Information Processing Systems 14*, The MIT Press, 2001, pp. 1073-1081.
- [12]. X. Xu, "Statistical learning in multiple instance problems". Master's thesis, University of Waikato, Hamilton, NZ, 2003.
- [13]. S. Andrews, I. Tsochantaridis and T. Hofmann, "Support vector machines for multiple-instance learning", *Advances in Neural Information Processing Systems 15*, Cambridge, MA, USA, 2003, pp. 577-584.
- [14]. J. Wang and J. Zucker, "Solving the multiple-instance problem: A lazy learning approach". In: *Proceeding of the 17th International Conference on Machine Learning, Morgan Kaufmann*, 2000, pp. 1119-1126
- [15]. L. Dong, "A comparison of multi-instance learning algorithms", Master's thesis, University of Waikato, 2006.
- [16]. E. Frank and X. Xu, "Applying propositional learning algorithms to multi-instance data", Technical report, University of Waikato, Hamilton, NZ, 2003, ISSN 1170-487X.
- [17]. X. Xu and E. Frank, "Logistic regression and boosting for labeled bags of instances", In: *Proceedings of the Pacific Asia Conference on Knowledge Discovery and Data Mining, Lecture Notes in Computer Science*, Springer, 2004, pp. 272-281.
- [18]. A. Cano, "An ensemble approach to multi-view multi-instance learning", *Knowledge-Based Systems*, vol. 136, 2017, pp. 46-57.
- [19]. J.-S. Wu, S.-J. Huang, and Z.-H. Zhou, "Genome-wide protein function prediction through multi-instance multi-label learning", *IEEE/ACM Transactions on Computational Biology and Bioinformatics*, vol. 11, issue 5, 1 September 2014, Article number 2323058, pp. 891-902.
- [20]. S. Sastrawaha and P. Horata, "Ensemble extreme learning machine for multi-instance learning", In: *Proceeding of 9th International Conference on Machine Learning and Computing (ICMLC 2017)*, Singapore, 24-26 February 2017, *ACM International Conference Proceeding Series*, volume part F128357, pp. 56-60.
- [21]. E. Frank, M.A. Hall, and I.H. Witten, *The WEKA Workbench. Online Appendix for "Data Mining: Practical Machine Learning Tools and Techniques"*, Morgan Kaufmann, fourth edition, 2016.



Response Surface Method for Optimization of Suspension Ball Joint Pull Out Force by Using Ansys

Alimurtaza Rutci¹, Fatih Selman Eren²

Abstract

Suspension ball joints are used to connect the control arms to the knuckle since they are the only joints which let rotational freedom. With the objective to an adequate performance of the ball joint, it is very important to prevent the extraction of the ball stud from the ball joint housing. Ball joint's housing material and shape design must withstand axial loads in the ball stud from axial direction in order to avoid the ball stud pull out keeping the ball stud inside the housing. The ball stud pull out force is a critical and safety characteristic function because it is related to failure mode for front suspension system. In this study, we investigate how the shape design and materials effect the suspension ball joint pull out force via response surface method for optimization based on FEA method. The objective of response surface methods (RSM) is optimization, finding the best set of factor levels to achieve some goal. With respect to optimization results, it is possible to monitoring best shape and appropriate material for the ball joint design. The result of FE analysis and RSM optimizations make it possible to determination best design characteristic.

Keywords: Response surface method, Optimizations, Ball joint, Pull out force, Ansys

1. INTRODUCTION

Ball joint is the one of the main component of the suspension and steering systems of the vehicles. This component is responsible to connect two vehicle modules allowing rotation and oscillation movements in both suspension and steering systems of the vehicles. Ball joints have critical function in both systems and defined as a safety part. These components are exposed to different kind of loads during ride and it has to be sure that the component is safe enough. To obtain the strength of the component there are some tests should be done. One of the test is the pull-out of the ball stud. This study aims to use response surface methodology for optimization of ball joint housing design dimension. ANSYS DesignXplorer is used for optimization. Optimizations algorithms uses genetic aggregation for response surface, DOE matrix for design points and MOGA (Multi-Objective Genetic Algorithm) method for candidates points in different regions. The main idea of RSM is to use a sequence of designed experiments to obtain an optimal response and aimed at reducing the cost of expensive analysis methods.

¹ Corresponding author: Teknorot Automotive Product Industry, Research-Development Center, Düzce –Turkey.
alimurtaza.rutci@teknorot.com



Figure 1. An assembly of ball joint in front suspension system

Ball joints consist various elements that their responsibilities, geometrical shapes and materials are different. The Figure 1 demonstrates a ball joint depicting its components. The ball joints main components: ball stud provide a mechanical connection between the housing and with castle nut and cotter pin. The ball stud is subject to the highest forces in the ball joint. Housing is the base component designed to accommodate the ball stud and ball bearing. Dust cover is designed for protecting the ball joint from contamination that causes additional wear on the ball bearing and corrosion of the ball stud. One of the main part of the ball joint is a plastic ball bearing due to minimize wear, reduce friction, better vibration damping. The Figure 2 shows how to assemble ball joints in the suspension system.

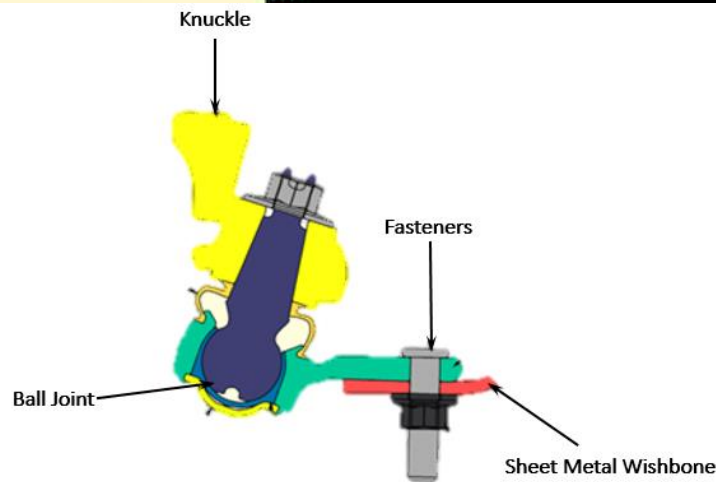


Figure 2. The Cross-Section View of Ball Joint Assembly

2. MATERIALS, BOUNDARY CONDITIONS AND FINITE ELEMENT ANALYSIS

To achieve the specific objectives this study has its own way of process and application. To determine stress distribution, force reactions and other analysis processes of the ball joint, CAD model is designed at NX Unigraphics 12.0. and imported to the ANSYS Workbench 19.1. Response surface methodology for optimization analysis performed at the process which are defined below.

2.1. Materials

Properties	Physical	Material		
		AISI 1040	AISI 5140	Delrin 100
Mechanical	Density (kg/m ³)	7800 - 7900	7800 - 7900	1420
	Poisson's Ratio	0,27 - 0,30	0,27 - 0,30	
	Young Modulus (MPa)	2,08e5 - 2,16e5	2,08e5 - 2,16e5	3000
	Tensile Strength (MPa)	525	575	
	Yield Strain (%)	24 - 36	23 - 35	26
	Yield Strength (MPa)	355	295	72
	Compressive Strength (Mpa)	315 - 390	260 - 325	110
	Flexural Modulus (GPa)	208 - 216	209 - 217	2,9
Thermal	Hardness (HV)	143 - 173	155 - 190	
	Melting Point (°C)	1430 - 1510	1430 - 1510	178

Material	Chemical Composition					
	C	Mn	P	S	Si	Cr
AISI 1040	0,37 - 0,44	0,6 - 0,9	Max. 0,04	Max. 0,05	-	-
AISI 5140	0,38 - 0,43	0,7 - 0,9	Max. 0,035	Max. 0,04	0,15 - 0,35	0,7 - 0,9
Delrin 100	POM (Polyoxymethylene)					

Table 1. Material Properties

2.2. Boundary Conditions and Finite Element Analysis

Meshed 2D axisymmetric model of the component consist of 4891 elements and 15423 nodes. Elements size of ball bearing is 0.2 mm and the rest is 0.4 mm. The model has been simplified due to reduce solving time obtain accurate results. The CAD model is constrained as the body is fixed from point A and the ball stud is forced to pull out from the point B. Boundary conditions and d meshed models are as in Figure 3.

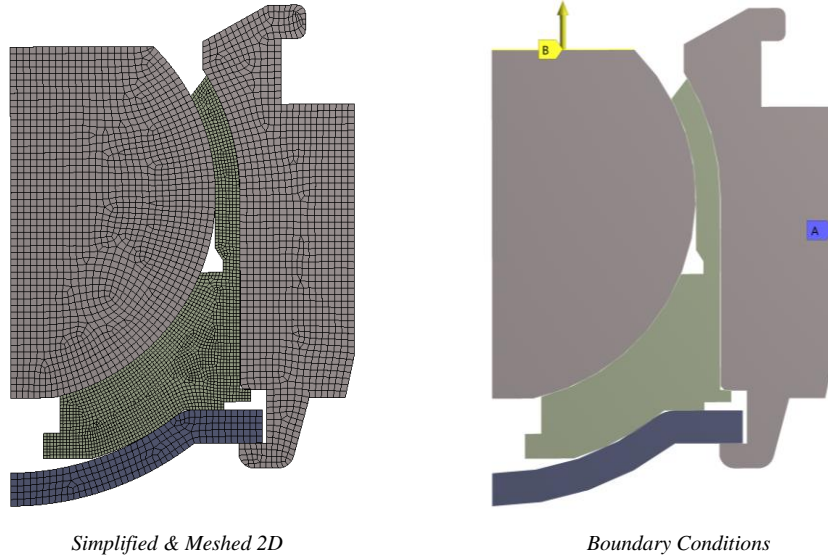


Figure 3. 2D Axisymmetric Model

Stress distribution on the component is shown in the Figure 5 below for axisymmetric model. The equivalent stress is 460 MPa at the edge of the housing.

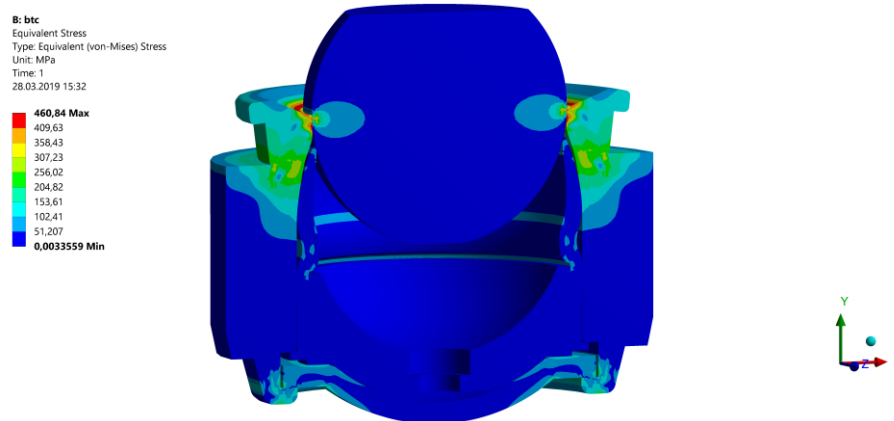


Figure 4. Stress Distribution 2D Axisymmetric Model

3. RESPONSE SURFACE METODOLOGY FOR OPTIMIZATION

Response surface methodology (RSM) is a collection of mathematical and statistical techniques for empirical model building. By careful design of experiments, the objective is to optimize a response (output variable) which is influenced by several independent variables (input variables). An experiment is a series of tests, called runs, in which changes are made in the input variables in order to identify the reasons for changes in the output response. The main idea of RSM is to use a sequence of designed experiments to obtain an optimal response.

The application of RSM to design optimization is aimed at reducing the cost of expensive analysis methods (e.g. finite element method or CFD analysis) and their associated numerical noise. The response can be represented graphically, either in the three-dimensional space or as contour plots that help visualize the shape



of the response surface Contours are curves of constant response drawn in the xi, xj plane keeping all other variables fixed. Each contour corresponds to a particular height of the response surface.

3.1. ANSYS DesignXplorer Input Parameters

In DesignXplorer applications you can define key simulation properties to be parameters. In this study we defined five parameters for the inputs. Five parameters represent an angle – A9, two vertical dimensions -V1; V7 and two horizontal dimensions - H11; H12. The Figure 5 represent the related parameters and initial dimensions.

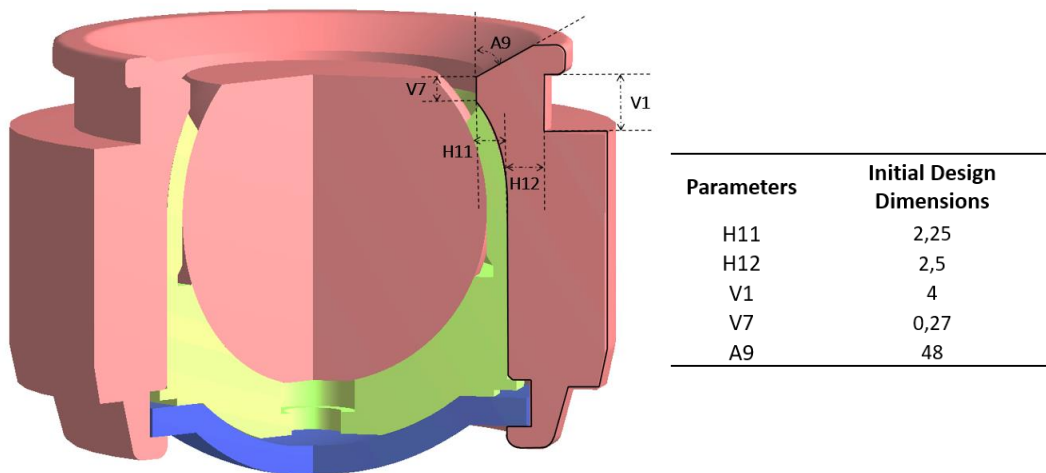


Figure 5. Ball Joints Input Parameters & Initial Design Dimensions

3.2. ANSYS DesignXplorer Design of Experiments

You can then manipulate the parameters at the project level in Workbench to investigate design alternatives. A set of parameter values representing one design alternative is called a design point. You can create a set of design points in tabular form and run them automatically to perform a what-if study.

For the most part, you work with parameters and design points on the parameters tab and the parameter set tab. However, you can also use parameters and design points in ANSYS DesignXplorer for automated design exploration studies. Design points distribution is shown below. Each point matched-up and DOE Matrix is generated.



Table of Outline A2: Design Points of Design of Experiments

1	A	B	C	D	E	F	G	H
1	Name	P8 - XYPlane.H12 (mm)	P4 - XYPlane.V1 (mm)	P10 - XYPlane.H11 (mm)	P13 - XYPlane.A18 (degree)	P14 - XYPlane.V17 (mm)	P6 - Equivalent Stress Maximum (MPa)	P12 - Force Reaction 2 Maximum Y Axis (N)
2	1	2,5	4	2,25	49,072	1,1224	690,81	29753
3	2	2	4	2,25	49,072	1,1224	667,59	28884
4	3	3	4	2,25	49,072	1,1224	686,14	33469
5	4	2,5	3,5	2,25	49,072	1,1224	703,35	34310
6	5	2,5	4,5	2,25	49,072	1,1224	678,83	29471
7	6	2,5	4	2	49,072	1,1224	635,75	25805
8	7	2,5	4	2,5	49,072	1,1224	712,25	36862
9	8	2,5	4	2,25	43,143	1,1224	687,72	33961
10	9	2,5	4	2,25	55	1,1224	651,27	27327
11	10	2,5	4	2,25	49,072	0,24689	607,25	24437
12	11	2,5	4	2,25	49,072	2	694,03	39347
13	12	2,3583	3,8583	2,3208	47,392	1,3718	692,51	31875
14	13	2,6417	3,8583	2,3208	47,392	1,3718	710,85	36349
15	14	2,3583	4,1417	2,3208	47,392	1,3718	707,96	33930
16	15	2,6417	4,1417	2,3208	47,392	1,3718	717,75	30683
17	16	2,3583	3,8583	2,1792	50,751	0,87508	652,31	25240
18	17	2,6417	3,8583	2,3208	47,392	1,3718	692,51	30722
19	18	2,3583	4,1417	2,1792	50,751	1,3718	660,29	28670
20	19	2,6417	4,1417	2,1792	50,751	1,3718	657,88	26760
21	20	2,3583	3,8583	2,3208	50,751	0,87508	687,37	32918
22	21	2,6417	3,8583	2,3208	50,751	0,87508	702,36	30049
23	22	2,3583	4,1417	2,3208	50,751	0,87508	681,04	27431
24	23	2,6417	4,1417	2,3208	50,751	1,3718	694,31	34433
25	24	2,3583	3,8583	2,3208	50,751	0,87508	687,37	32918
26	25	2,6417	3,8583	2,3208	50,751	0,87508	702,36	30049
27	26	2,3583	4,1417	2,3208	50,751	0,87508	681,04	27431
28	27	2,6417	4,1417	2,3208	50,751	1,3718	694,31	34433

Figure 6. DOE Matrix

3.3. Response Surface

Understand the sensitivities of the output parameters (results) write the input parameters. Response Surface Method addresses limitations of parametric analysis and to further explore design options and perform optimization etc.

The change of the output based on the change of each input independently is shown local sensitivity bar chart. Local sensitivity results are shown as Figure 7.

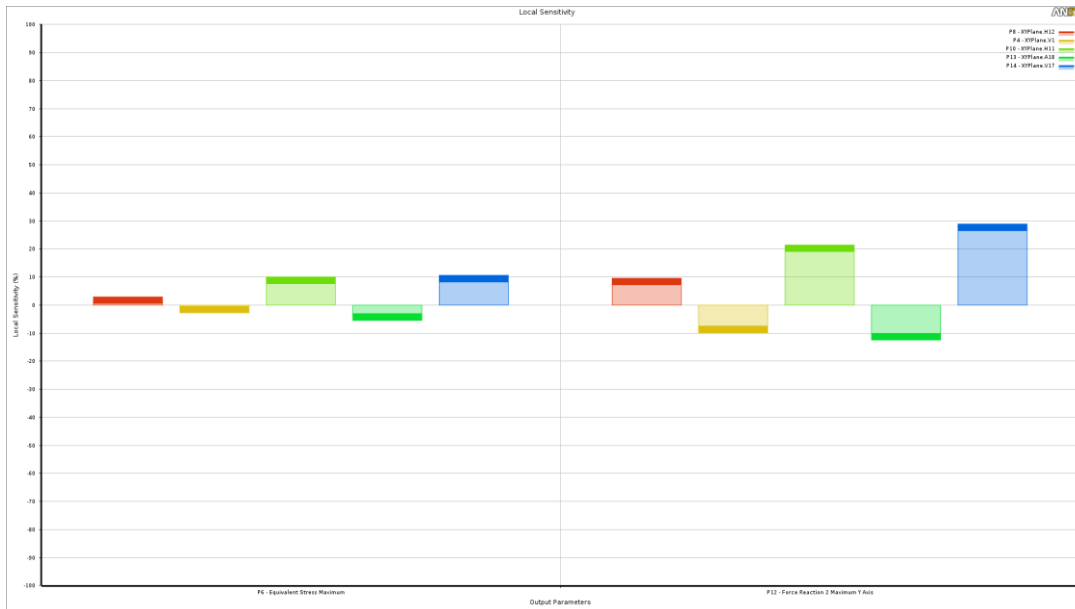


Figure 7. Local Sensitivity Bar Chart

Response surfaces are functions of different nature where the output parameters are described in terms of the input parameters and provide the approximated values of the output parameters, everywhere in the analyzed design space, without the need to perform a complete solution. There are six response surface types in DesignXplorer; Genetic Aggregation, Standard Response Surface (2nd order polynomial), Kriging, Non-parametric Regression, Neural Network, Sparse Grid.



In this study, genetic aggregation response surface type is used. It runs an iterative genetic algorithm to find the best response surface type and settings for each output parameter. It selects the best ones and combines them to build an “aggregation” of several response surfaces. It results to the best RS quality and different settings for each output parameter.

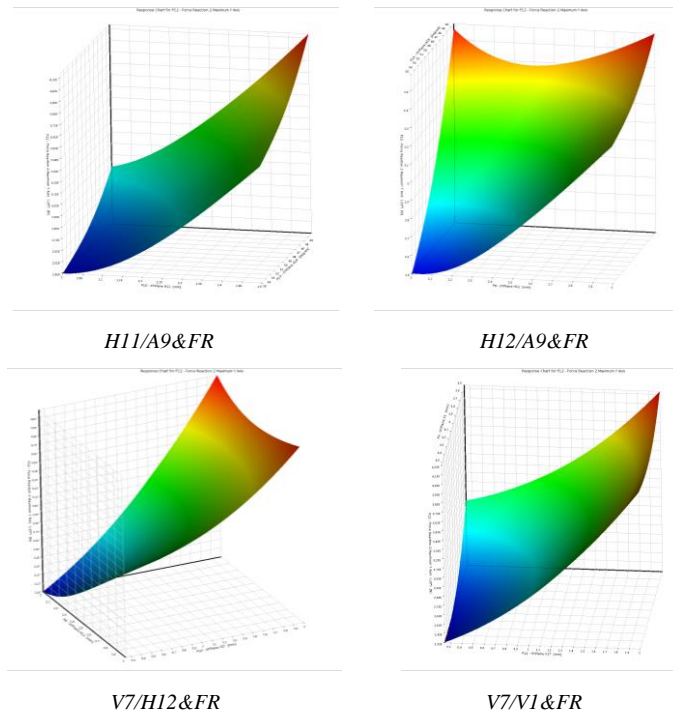


Figure 8. Response Surface of Each Parameter

4. EXPERIMENTAL STUDY

Experimental study is done with the same boundary conditions as applied on the simulation. Initial design and final design samples used for the experimental study. Force reaction and so the pull out force is obtained from the testing system (Figure 9).

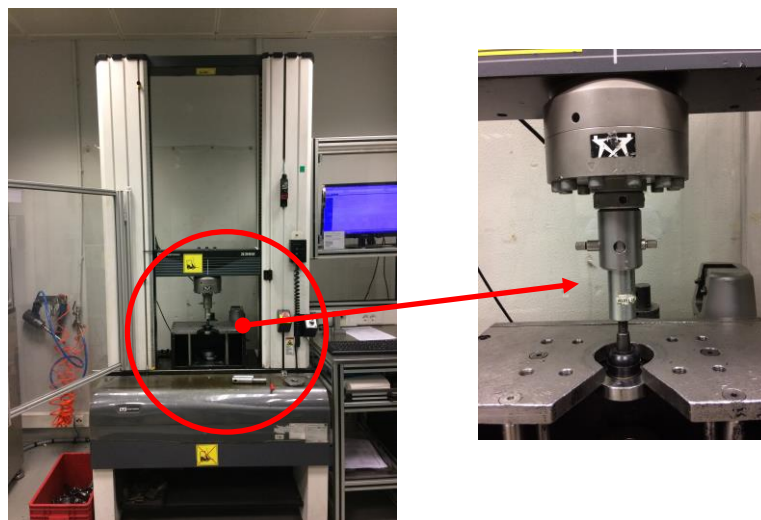


Figure 9. Ball Joint Test Ring



5. CONCLUSIONS

Optimization study uses the MOGA (Multi-Objective Genetic Algorithm) method. Method provides several candidates in different regions. Program generate 5000 samples initially, 1000 samples per iteration and find 3 candidates in a maximum of 20 iterations that converged after 15440 evaluations. In this study candidate point 3 has been selected as optimal design shown in Figure 10.

Candidate Points			
	Candidate Point 1	Candidate Point 2	Candidate Point 3
P8 - XYPlane.H12 (mm)	2,3476	2,7639	2,7362
P4 - XYPlane.V1 (mm)	3,6148	4,144	3,5521
P10 - XYPlane.H11 (mm)	2,2049	2,4184	2,1206
P13 - XYPlane.A9 (degree)	45,39	51,11	47,304
P14 - XYPlane.V7 (mm)	1,5029	1,5136	1,9105
P6 - Equivalent Stress Maximum (MPa)	700,31	698,8	675,59
P12 - Force Reaction 2 Maximum Y Axis (N)	★★★ 40000	★★★ 39999	★★★ 40001

Figure 10. Candidates Points

Initial design dimensions and final design dimensions are compared and changes are shown in Figure 11.

Parameters	Units	Initial Design Dimensions	Final Design Dimensions	Change %
H11	mm	2,25	2,12	5,7%
H12	mm	2,5	2,73	8,4%
V1	mm	4	3,55	11,2%
V7	mm	0,27	1,9	85,7%
A9	mm	48	47,3	1,45%
Force Reaction	N	23195	40000	42%
Equivalent Stress	Mpa	621,1	675,59	8%

Figure 11. Initial And Final Design Comparison Table

It can be seen that response surface optimizations provide the approximated values of the output parameters, everywhere in the analyzed design space, without the need to perform a complete solution. Thousands of configurations can be analyzed within a few seconds. With respect to optimization results, it is possible to monitoring best shape and appropriate material for the ball joint design. The result of FE analysis and RSM optimizations make it possible to determination best design characteristic.

ACKNOWLEDGMENT

These study was supported by Teknorot Automotive A.S R&D Center. We thank our colleagues from R&D Center who provided insight and expertise of this paper. Also we appreciate to R&D Director Mr. Murat ARSLANOGLU, R&D Manager Mr. Gokhan AKGUL, R&D Project Manager Mr. Fatih CAGIRANKAYA for their technical support.

REFERENCES

- [1]. A. Rutci, F.S. Eren, Investigation of Suspension Ball Joint Pull Out Force Based on FEA Method and Experimental Study. 6th International Symposium on Innovative Technologies in Engineering and Science, 2018.
- [2]. B. HeiBing, M. Ersoy (Eds.) Chassis Handbook; Fundamentals, Driving Dynamics, Components, Mechatronics, Perspectives, ISBN 978-3-8348-0994-0
- [3]. <http://dupont.materialdatacenter.com/profiler/main/>
- [4]. Teknorot Automotive R&D Center Design Guide
- [5]. https://www.sharcnet.ca/Software/Ansys/17.0/en-us/help/wb_sim/
- [6]. Herbert Ricardo Rosa M, Marcus Z. Ball Joint Pull Out Simulation using Finite Element Analysis, 2006
- [7]. Helena Osório F, Artur Pinto de A, Marcus Z, Henrique Nelson S, Sergio Cardoso da S. Suspension ball joint failure analysis based on problem solving process, 2006
- [8]. J. Reimpell, H. Stoll, J.W. Betzler. The Automotive Chassis: Engineering Principles Second Edition, ISBN 0750650540
- [9]. John C. Dixon, PhD, F.I.Mech.E., F.R.Ae.S. Suspension Geometry and Computation, WILEY, ISBN: 9780470510216



The Pure Bending Fatigue Behaviour Of The Heavily Drawn Steel Filaments

Hayrettin Ahlatci¹, Yunus Turen¹, Yavuz Sun¹, Huseyin Koymatcik²

Abstract

The aim of this study is the investigation of the effect of the manufacturing and carbon content on the fatigue strength. Fatigue tests of the steel filaments (narrowed cross-section) in diameter of 0.25 mm with two different Carbons (0.70%C and 0.90%C), carried out a frequency of 10 Hz via a custom manufactured rotating bending testing machine (designed and manufactured with TUBITAK support) of which the fully reserved strain amplitudes ($R = \epsilon_{min}/\epsilon_{max} = -1$) The applied value of strain amplitudes, has been chosen from the range 0.30%-1.07% as alternating of tension and compassion with each rotation bending strain. The fatigue strain limit values have been determined on the plot of S-N strain-cycle curves as 0.55% and 0.30% units for the steels of the NT250-70 C and UT250-90 C quality, respectively.

Keywords: Steel Tire Cord, Carbon Content, Pure Bending Fatigue.

1. INTRODUCTION

Steel filament often work with high external loads and find wide application in situations where high reliability of working is required, like different kinds of machines and devices [1]. Sensitive fatigue life estimation in the design of structures subject to variable load conditions is critical when human life is particularly at stake. Steel cord filaments used to are building blocks of a tire, with a high fatigue strength meets the needs such as long life, better fuel economy, and in particular safety. Accurate estimation of fatigue behaviors of cord steel during its service is of vital importance because of this variable repeated loading [2].

The effect of microstructure on fatigue behavior in steels has been widely investigated [3]-[7]. The crack initiation and propagation by fatigue loading are influenced by microstructural parameters of the materials such as ferritic-pearlite steel and eutectoid steels. The purpose of this study is to compare fatigue behaviors of the 0.25 mm diameter steel filaments with 0.7 wt% and 0.9 wt% C contents. Researches on the detailed influenced of fatigue mechanism of the strongly heavily drawn steel cord filaments are limited.

2. EXPERIMENTAL PROCEDURES

Steel cord filaments with carbon contents of 0.70 wt% and 0.90 wt% which were procured from Bekaert have been employed in this work. Their chemical compositions and mechanical properties are given in Table 1. The material codes of Table 1 indicates that the numbers of 250 and 70C/90C are the filament diameter in inch and carbon contents, respectively and the letters T, N and U mean Tensile, Normal and Ultra, respectively.

Table 1. Chemical and mechanical properties of the investigated steel cord filaments.

Grade Code	Chemical Composition					Tensile Strength* (N/mm ²)	Total Elongation* (%)	Drawing Deformation* (%)
	C % avg.	Mn % avg.	Si % avg.	P % max.	S % max.			
NT250-70 C	0.72	0.53	0.22	0.025	0.025	2755.50	1.97	3.25
UT250-90 C	0.92	0.35	0.22	0.020	0.015	3797.49	2.21	3.76

*Manufacturer's data.

Metallographic examination of the investigated steel cord filaments as given in Table 1 was made as standard following an etching via 4% nital have been carried out with a Carl Zeiss Ultra Plus Gemini Fesem SEM device. Five hardness measurements for each sample fine grinded and polished longitudinally and vertically have been

¹ Department of Metallurgical and Material Science Engineering, Karabuk University, Karabuk, Turkey

² Karabuk Iron Steel Industry and Trade Inc., Kardemir, Karabuk, Turkey



taken via a QNESS Q10 brand microhardness tester employing a diamond square pyramidal tip with an apex angle of 136° by applying a 3 kg of load for 15 s.

In this work, pure bending fatigue tests of the steel cord filaments have been realized via a fatigue testing machine, as exhibited in Fig. 1a. Fatigue testing machine was designed and produced in compliance with ASTM E2948-14 standard by authors of this paper. The features of the motor used in the machine are 0,37 kw three-phase electric motor and frequency inverter driver, 1400 rpm, 25 kg/cm of torque, up to 50 Hz of frequency.

The cord filaments of certain length are semi circular grooved between special clamps so that they do not sustain plastic deformations [8] and [9]. During the testing each end of the filaments was clamped in a motor driven chucks as seen in Fig. 1b and the chuck rotated at a frequency of 10 Hz, with the strained filament experiencing an alternating state of tension and compression with each rotation at fully reserved strain ratio of $R=-1$. In the fatigue tests carried out in this work, alternating strain amplitudes were varied between 0.30%-1.07% as bending strain.

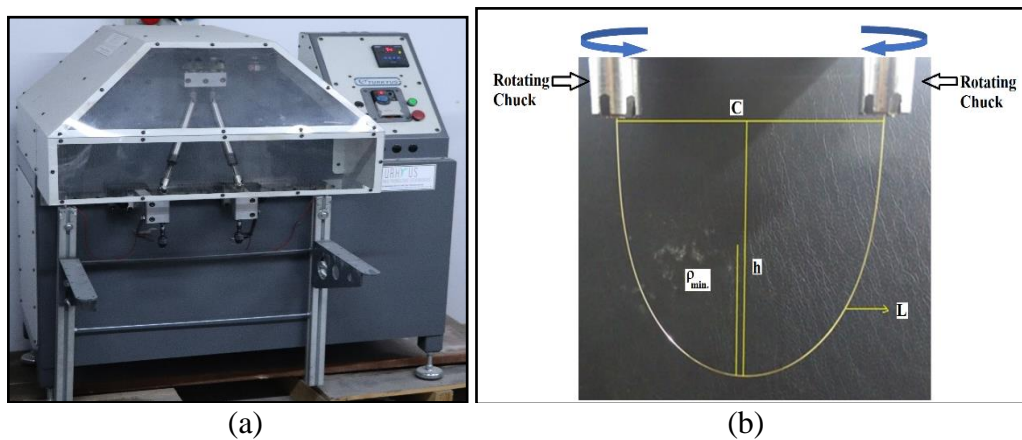


Fig. 1. (a) Pure bending fatigue testing machine designed and produced for this work and (b) actual sample installed in chucks and motion direction of the filament during test.

3. RESULT AND DISCUSSION

Fig. 2 displays SEM images of the etched NT250-70 C and UT250-90 C filaments at high magnification. The microstructures of the inspected filaments are of fibrous structure due to the strongly heavily drawing and more coarse fibrous structure have occurred in the UT250-90 C quality steel which has a higher carbon content. Hardness of the NT250-70C filament is 750 HV3 while that of the UT250-90C filament is 860 HV3. This is attributed to the carbon content and amount of the drawing deformation of the NT250-70 C and UT250-90 C filaments which are 3.25% and 3.76% (Manufacturer's data.), respectively. In this study the angular and longitudinal pearlite produced parallel structure oriented to the drawing axis while the vertical pearlite formed waved structure in the direction perpendicular the drawing axis after the drawing process (Fig. 3).

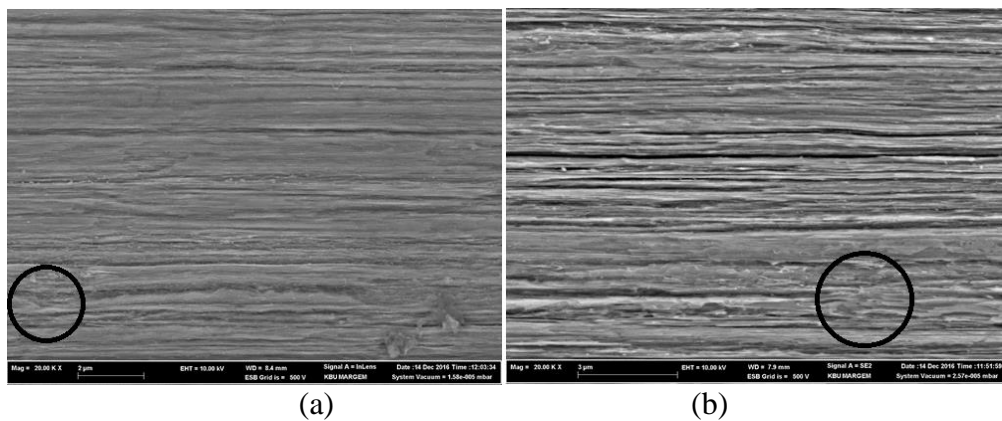




Fig. 2. SEM images of the (a)NT250-70C and (b) UT250-90C filaments at high magnification (waved formation is shown inside the circle).

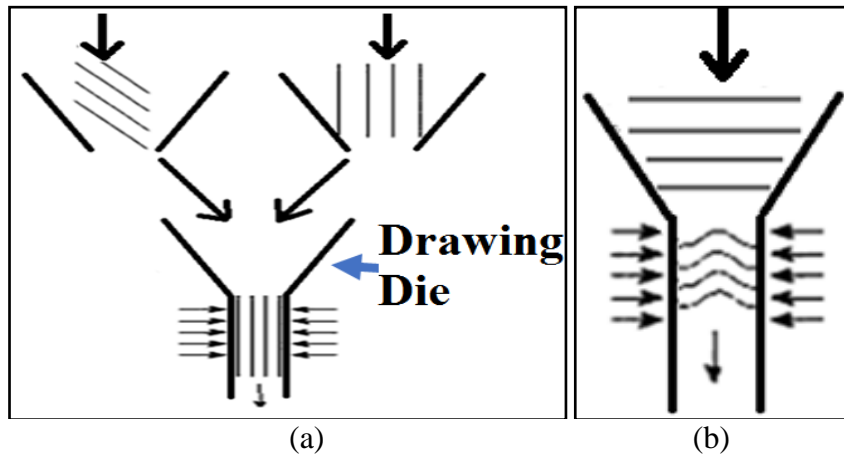


Figure 3. Schematic views of the formation of (a) parallel and (b) wavy microstructures after heavily drawing (Horizontal, angled and vertical lines to drawing axis indicate pearlite before drawing processes.)

S-N curves for 2 different quality filaments which have been inspected in this work are exhibited in Fig. 4. S-N curves are plotted on a logarithmic scale as damage realized at a given strain amplitudes versus number of cycles (fatigue life). In Fig. 4, the fatigue life data are represented by filled symbols while the fatigue limit data are shown by hollow symbols.

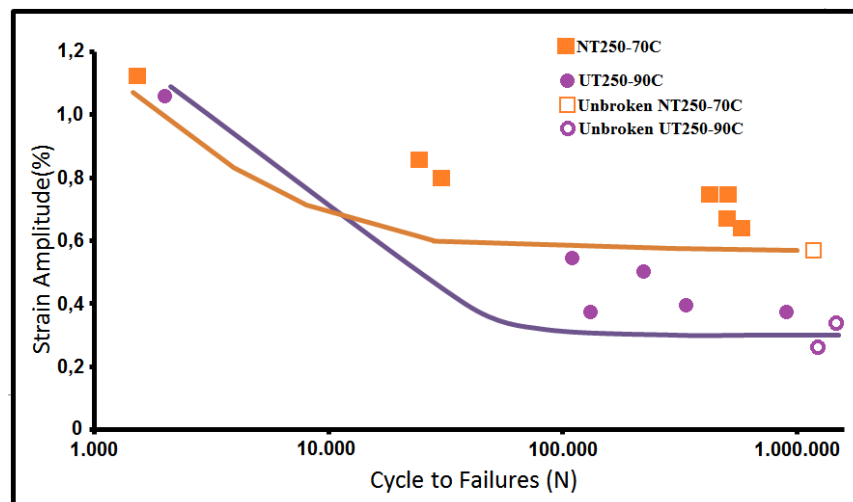


Fig. 4. Strain amplitude(%) - cycle to failures curves of the investigated steel cord filaments.

Fatigue limit values for the investigated NT250-70C and UT250-90C filaments as inspected by exploiting Fig. 4 are 0.55% and 0.30%, respectively. This value indicates that despite hardness increases with increasing carbon content, the fatigue limit decreases. The UT250-90 C filament with the highest hardness value of 860 HV3 in comparison with the hardness of the NT250-70C filament has the lowest fatigue limit value of 0.30%, as shown in Fig. 4. We assume [9] that the factor to the low fatigue strength of the UT250-90 C steel filament is due to a rougher texture compared to the NT250-70 C filament.

4. CONCLUSIONS

In the present study, the influence of carbon content and microstructure on the fatigue resistance has been investigated for the tire cord filament drawn up to 0.25 mm diameter and conclusions have been drawn from this work in cold drawn pearlitic steel. In fully pearlite cord steel with oriented fine fibrous pearlite



microstructure of the NT250-70C filaments as a consequence of strongly heavily cold drawing the orientation of fine ferrite/cementite lamellae increased the fatigue resistance. The reason for this behavior is the fact that the fine fibrous cementite lamellae act as serious obstacles in front of dislocations and therefore for crack advance.

5. ACKNOWLEDGMENTS

The authors would like to express thanks to Bekaert Izmit Steel Cord Industry and Trade Inc. Technology department and The Scientific and Technological Research Council Of Turkey (1005 - National New Ideas and Products R&D Funding Program coded as 117M102) for supplying steel wires and supporting this work financially.

References

- [1] R.Kruzal, M. Suliga, The effect of multiple bending of wire on the residual stresses of high carbon steel wires, *Metalurgija* 52 (2013), 93-95.
- [2] C. Wei and O. A. Olatunbosun, The effects of tyre material and structure properties on relaxation length using finite element method, *JMADE*, vol. 102, pp. 14–20, 2016.
- [3] Y. Mutoh, Akhmad A.Korda, Y. Miyashita and T. Sadasue, Stress shielding and fatigue crack growth resistance in ferritic-pearlitic steel, *Materials Science and Engineering A* 468-470(2007), 114-119.
- [4] A.A. Konda, Y. Mutoh, Y. Miyashita, T. Sadasue, Effects of pearlite morphology and specimen thickness on fatigue crack growth resistance in ferritic-pearlitic steels, *Materials Science and Engineering A* (2006), 262-269.
- [5] F. Walther and D. Eifler, Local cyclic deformation behavior and microstructure of railway wheel materials, *Materials Science and Engineering A*(2004), 387-389.
- [6] J. Toribio, B. Gonzalez and J. Matos, Analysis of fatigue crack paths in cold drawn pearlitic steel, *Materials* 8-11(2015), 7439-7446.
- [7] J. Toribio, B. Gonzalez and J. Matos, Initiation and propagation of fatigue cracks in cold-drawn pearlitic steel wires, *Theoretical and Applied Fracture Mechanics* 92(2017), 410-419.
- [8] H.Koymatcik, H. Ahlatci, Y. Sun and Y. Turen, Effect of carbon content and drawing strain on the fatigue behavior of tire cord filaments, *Engineering Science and Technology, an International Journal* 21(2018), 289-296.
- [9] H.Koymatcik, Investigation of steel filaments fatigue behaviors with pure bending fatigue test methodology, *Institute of Science and Technology* (2019), 59-102.



The Fatigue Crack Propagation Of The Heavily Drawn Steel Cord Filaments

Hayrettin Ahlatci¹, Yavuz Sun¹, Yunus Turen¹, Huseyin Koymatcik²

Abstract

The effect of the pearlite morphology on the fatigue fracture mechanisms was examined. The crack path progressed by rotating bending fatigue test is affected by microstructure features of the investigated filaments, which was narrowed cross-section and/or drawn. The rotating bending fatigue device is designed and manufactured with TUBITAK support. The SEM inspection has demonstrated that a tortuous stable fatigue crack areas and angled rapid fatigue fracture zones carried out in a sequential order. The tortuous crack path induced crack interlocking as well as crack closure. The crack interlocking areas of the NT250-70C filaments are higher than that of the UT250-90C quality filaments. The crack path progressed by fatigue test is effected by microstructures features of the investigated filaments. Inclined rapid fatigue crack advances along the cementite fiber seam in the structure.

Keywords: Fracture Surfaces, Crack mechanism, crack growth.

1. INTRODUCTION

Accurate estimation of fatigue behaviours of cord steel during its service is of vital importance because of this variable repeated loading [1] The fatigue cracking morphology of the ferritic-pearlitic steels with networked and/or islands of pearlite colonies (isolad distribution) is lower tortuous than in those with uniformly distributed pearlite structure [2] [3] [4]. In eutectoid steels with fully pearlitic microstructure fatigue loading leads to break the cementite ferrite lamellae classified as transcollonial fracture [5],[6].

The purpose of this study is to compare the microstructures and propagation of fatigue cracks in the strongly heavily drawn steel cord. Researches on the detailed influenced of microstructure on fatigue behavior [7] and fatigue cracking mechanism of the strongly heavily drawn steel cord filaments are limited.

2. EXPERIMENTAL PROCEDURES

Steel cord filaments with carbon contents of 0.70 wt% and 0.90 wt% which were procured from Bekaert have been employed in this work. Their chemical compositions and mechanical properties are given in Table 1.

Table 1. Chemical and mechanical properties of the investigated steel cord filaments.

Grade Code	Chemical Composition					Tensile Strength* (N/mm ²)	Total Elongation* (%)	Drawing Deformation* (%)
	C % avg.	Mn % avg.	Si % avg.	P % max.	S % max.			
NT250-70 C	0.72	0.53	0.22	0.025	0.025	2755.50	1.97	3.25
UT250-90 C	0.92	0.35	0.22	0.020	0.015	3797.49	2.21	3.76

*Manufacturer's data. "Letters T, N and U mean Tensile, Normal and Ultra, respectively."

In this paper, a fracto-metallographic analysis was performed on the cracked specimens of cold drawn pearlitic steel subjected to pure bending fatigue tests. Right-Left matching surfaces of the filament fractured at the lowest number of cycles (high fatigue strain life) and close to the fatigue strain limit have been examined on the SEM

¹ Department of Metallurgical and Material Science Engineering, Karabuk University, Karabuk, Turkey

² Karabuk Iron Steel Industry and Trade Inc., Kardemir, Karabuk, Turkey Karabuk, Turkey

in order to understand and obtain information about the influence of microstructure (pearlite morphology) on fatigue crack growth mechanism by increasing carbon content and drawing proses

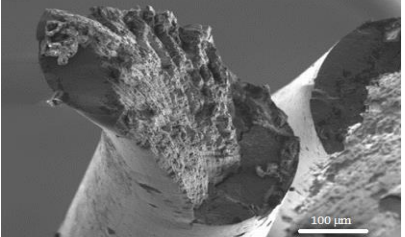
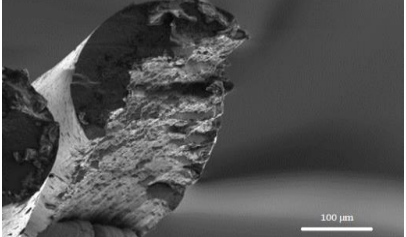
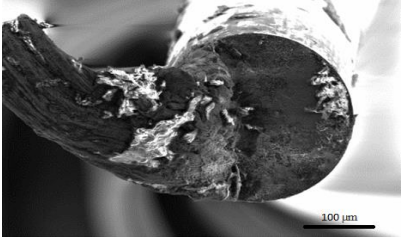
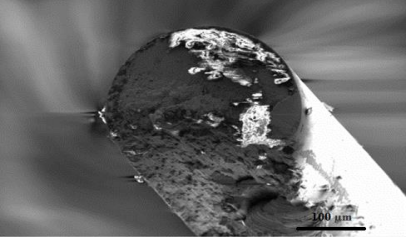
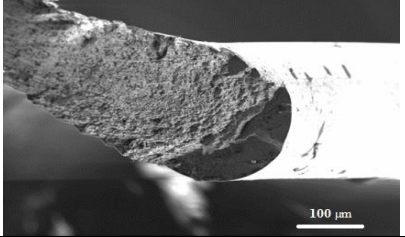
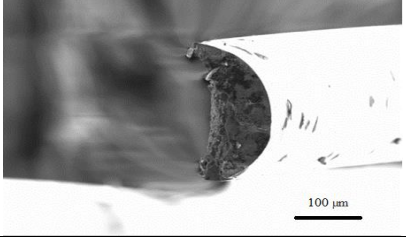
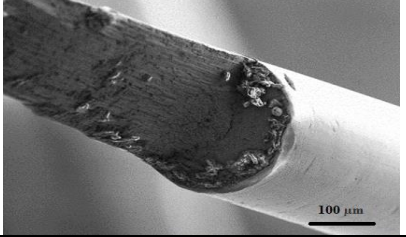
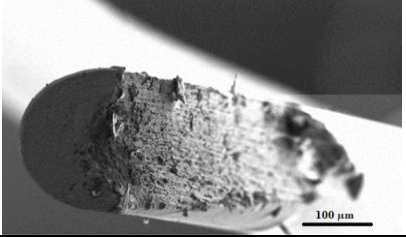
Filament Code	Bending Strain Amplitudes (%)	Right-Left Matching surfaces of the fractured filament	
0.25 NT-70 C	1.07		
	0.58 (Fatigue Strain Limits)		
0.25 UT-90 C	1.07		
	0.21 (Fatigue Strain Limits)		

Fig. 1. Cross-section SEM images of the 0.25 NT-70 C and 0.25 UT -90C filaments after fatigue testing.

3. RESULTS AND DISCUSSION

The fatigue strain limit values have been determined by pure bending fatigue test [8] as 0.55% and 0.30% units for the steels of the NT250-70 C and UT250-90 C quality, respectively. Despite the differences in fatigue life, carbon content and manufacturing factors of the investigated filaments, the SEM inspection of right-left matching fractured surfaces has demonstrated that the morphology of the fracture surfaces was similar to each other. Each fracture surface consisted of two distinct regions: tortuous stable fatigue crack growth and inclined rapid fatigue fracture with respect to the drawing axis. A sudden slit occurs during the transition between the two zones. With respect to the relative area of two regions, the crack growth area increased significantly with decreasing strain amplitude (Fig. 1) and carbon content, increasing the fatigue strain limit [8],[9].



Fig. 2 shows the longitudinal SEM appearance of the fatigue fracture morphology of the investigated filaments. This reveals that fatigue cracks of the filaments initiate and propagate from the surface towards the bulk perpendicular to the surface and terminate at the final inclined rapid fatigue crack path which are obliquely oriented to the drawing axis. An increase in roughness of the fatigue fracture surface of the NT250-70C filament can also be detected by tortuous cracking. No capillary, progressing transverse cracks and tortuous cracking are able to be detected on the (fractured) surface of the UT250-90C filaments with lower fatigue resistance. The tortuous cracking as well as interlocking mechanisms cause the fatigue crack closure and the increase of the fatigue resistance.

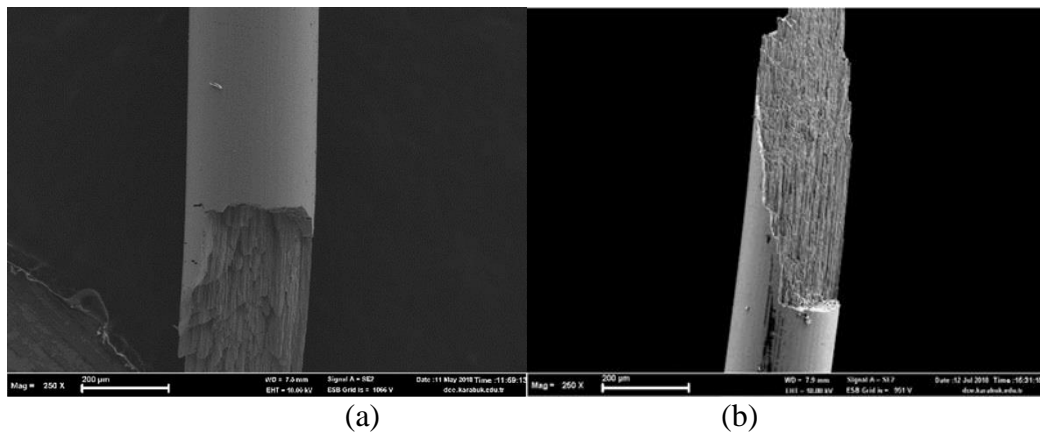


Fig. 2. Longitudinal SEM appearance of the fatigue fracture morphology of (a) the NT250-70 C and (b) UT250-90C filaments tested at 1.07 % strain amplitude.

Fig. 3 schematically illustrates the appearance of fatigue cracks in two regions. Fatigue cracks in the tortuous stable fatigue crack growth region progresses by cutting the cementite lamellae, while fatigue cracking along the connection line between the cementite lamellae in the inclined rapid fatigue fracture region is rapidly completed. The regions of the tortuous stable fatigue crack growth and the inclined rapid fatigue fracture are separated by a deep and sharp crack formed between the cementite lamellae.

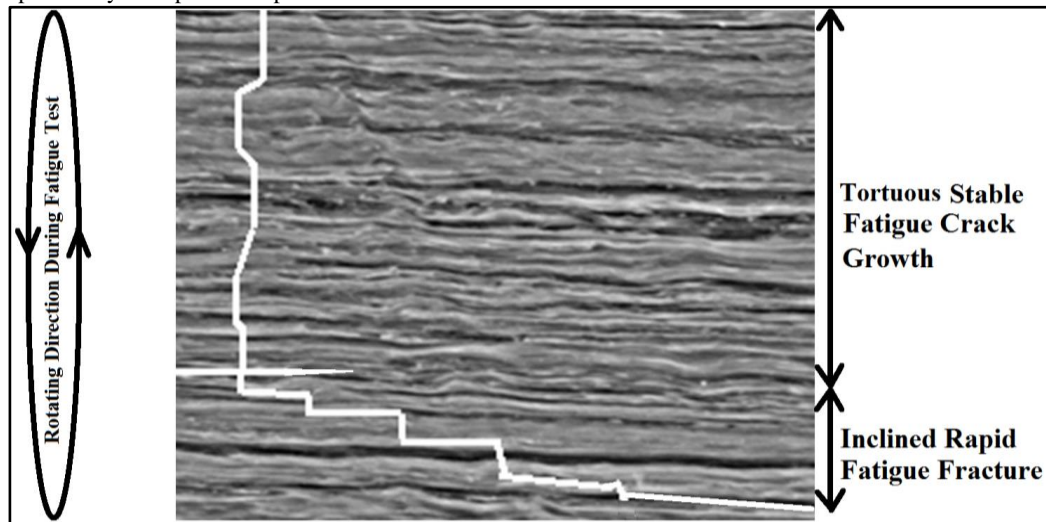


Fig. 3. Schematic of crack growth mechanisms.

4. CONCLUSIONS

In the present study, the influence of carbon content and microstructure on the fatigue fracture mechanism has been investigated for the tire cord filament drawn up to 0.25 mm diameter and conclusions have been drawn from this work regarding the fracto-metallographic analysis of fatigue cracking in cold drawn pearlitic steel. The fractured surfaces obtained after the fatigue test are divided into two regions: as inclined and tortuous



zones. The tortuous zones is crack growth region while the inclined zone is final rapid crack region of the creaked surface .The greater the area of the tortuous zone, the higher the fatigue strength.

5. ACKNOWLEDGMENTS

The authors would like to express thanks to Bekaert Izmit Steel Cord Industry and Trade Inc. Technology department and The Scientific and Technological Research Council Of Turkey (1005 - National New Ideas and Products R&D Funding Program coded as 117M102) for supplying steel wires and supporting this work financially.

REFERENCES

- [1] C. Wei and O. A. Olatunbosun, The effects of tyre material and structure properties on relaxation length using finite element method, *JMADE*, vol. 102, pp. 14–20, 2016.
- [2] Y. Mutoh, Akhmad A.Korda, Y. Miyashita and T. Sadasue, Stress shielding and fatigue crack growth resistance in ferritic-pearlitic steel, *Materials Science and Engineering A* 468-470(2007), 114-119.
- [3] A.A. Konda, Y. Mutoh, Y. Miyashita, T. Sadasue, Effects of pearlite morphology and specimen thickness on fatigue crack growth resistance in ferritic-pearlitic steels, *Materials Science and Engineering A* (2006), 262-269.
- [4] F. Walther and D. Eifler, Local cyclic deformation behavior and microstructure of railway wheel materials, *Materials Science and Engineering A*(2004), 387-389.
- [5] J. Toribio, B. Gonzalez and J. Matos, Analysis of fatigue crack paths in cold drawn pearlitic steel, *Materials* 8-11(2015), 7439-7446.
- [6] J. Toribio, B. Gonzalez and J. Matos, Initiation and propagation of fatigue cracks in cold-drawn pearlitic steel wires, *Theoretical and Applied Fracture Mechanics* 92(2017), 410-419.
- [7] K. Lambrihgs, M. Wevers, B. Verlinden, and I. Verpoest, A fracture mechanics approach to fatigue of heavily drawn steel wires, *Procedia Eng.*, vol. 10(2011), 3259–3266.
- [8] H.Koymatcik, Investigation of steel filaments fatigue behaviors with pure bending fatigue test methodology, *Institute of Science and Technology* (2019), 59-102.
- [9] H.Koymatcik, H. Ahlatci, Y. Sun and Y. Turen, Effect of carbon content and drawing strain on the fatigue behavior of tire cord filaments , *Engineering Science and Technology, an International Journal* 21(2018), 289-296.



Optimization of Parameters of Tuned Mass Dampers by Using Hybrid Metaheuristic Algorithms

Sinan Melih Nigdeli¹, Gebrail Bekdas² and Eylem Ayyildiz³

Abstract

In vibration control of mechanical systems, tuned mass dampers (TMDs) are used as a passive control device. TMDs have been also added to civil structures excited by wind, earthquake and traffic loads. The key factor of a TMD is the perfect tuning of the parameters such as stiffness and damping coefficients. Otherwise, TMD will not be effective in the vibration control of the main structure. For this purpose, several optimum tuning approaches have been developed. Most of the methods employ metaheuristic algorithms inspired by natural phenomena. In the present study, several hybrid algorithms are developed for optimum tuning of TMD positioned on a single degree of freedom structure under earthquake excitation in order to find a precise solution. The hybridization is done by using metaheuristic algorithms called Flower Pollination Algorithm (FPA), Teaching Learning Based Optimization (TLBO) and Jaya Algorithm (JA). These algorithms have different features. FPA is a two-phase algorithm with a switch probability to choose a phase in an iteration. TLBO is also a two-phase algorithm, but the two phases are consequently done. JA is a single-phase algorithm. The hybrid methods are effective in finding the optimum parameters of TMDs.

Keywords: Tuned mass dampers, metaheuristic algorithms, hybrid algorithms, optimum parameters.

1. INTRODUCTION

The absorber device invented by Frahm [1] is to damp vibrations of mechanical system and this invention is the first form of tuned mass dampers (TMDs). TMDs are used in a wide range of mechanical systems such as vibrating machines, automobiles, trains, ships, robotics and structures. In structures, the main application purpose is to reduce vibration of high-rise and tower buildings under wind excitation, but TMDs are also used for seismic structures. For example, Berlin TV Tower (Figure 1) has a 1.5t TMD using three cables and four hydraulic telescopic shock absorbers to reduce wind indicated vibrations. For seismic structures, Lax Theme Building (Figure 2) can be shown as an example. A 20% mass was installed during the seismic retrofit of Lax Theme Building to reduce responses between 30% and 40% [2].

¹ Corresponding author: Istanbul University-Cerrahpaşa, Department of Civil Engineering, 34320, Avcılar/İstanbul, Turkey. melihnig@istanbul.edu.tr

² Corresponding author: Istanbul University-Cerrahpaşa, Department of Civil Engineering, 34320, Avcılar/İstanbul, Turkey. bekdas@istanbul.edu.tr

³ Corresponding author: Istanbul University-Cerrahpaşa, Department of Civil Engineering, 34320, Avcılar/İstanbul, Turkey. eylemayyildiz@gmail.com



Figure 16. The Berlin TV Tower



Figure 2. The LAX Theme Building

The tuning of mass dampers is an important factor, because the main working principle of TMDs is to add an additional mode and this mode must be close to critical frequency of main structure. In that case, two frequencies will be around the frequency of uncontrolled structure to reduce effect at resonance state.

The first equations about tuning of mass dampers were proposed by Den Hartog [3] after damping added to the system of Frahm [1] to reduce responses of excitations with various frequencies. The equations of Den Hartog



[3] are the optimum frequency ratio (f_{opt}) and optimum damping ratio (ξ_{opt}) as shown in Eq. (1) and (2), respectively. These values are found according to mass ratio (μ) of TMD and single degree of freedom (SDOF) main structure. In the equations, the frequencies of TMD and main structure are shown with $\omega_{d,opt}$ and ω_s , respectively. In damping ratio formulation, c_d and m_d are the damping coefficient and mass of TMD, respectively. The damping coefficient of TMD (k_d) is found according to Eq. (3).

$$f_{opt} = \frac{\omega_{d,opt}}{\omega_s} = \frac{1}{1+\mu} \quad (1)$$

$$\xi_{d,opt} = \frac{c_d}{2m_d\omega_{d,opt}} = \sqrt{\frac{3\mu}{8(1+\mu)}} \quad (2)$$

$$k_d = \omega_{d,opt}^2 m_d \quad (3)$$

Differently from the equation of Den Hartog, several formulations have been also provided [5-9]. Also, Sadek et al. implemented inherent damping (ξ) of the structure to the equation as seen in Eqs. (4) and (5). Sadek et al. [10] derived these equations by using curve fitting of numerical analysis. A proposal for multiple degree of freedom (MDOF) systems in modification of equations by Sadek et al. and the critical vibration mode is only used in the proposal according to advice of Warburton and Ayorinde [11].

$$f_{opt} = \frac{1}{1+\mu} \left[1 - \xi \sqrt{\frac{\mu}{1+\mu}} \right] \quad (4)$$

$$\xi_{d,opt} = \frac{\xi}{1+\mu} + \sqrt{\frac{\mu}{1+\mu}} \quad (5)$$

By using numerical iterations, the effect of all vibration modes can be considered. For that reason, metaheuristic based methods have been proposed for optimum tuning of TMDs. The metaheuristic algorithms used in optimization of TMDs are genetic algorithm (GA) [12-16], particle swarm optimization (PSO) [17-18], bionic algorithm [19], harmony search algorithm (HS) [20-24], ant colony optimization (ACO) [25], artificial bee colony algorithm (ABC) [26], flower pollination algorithm (FPA) [23, 24, 27], teaching learning based optimization (TLBO) [23, 24, 28], bat algorithm [29] and Jaya [30-31].

In the present study, two hybrid algorithms were used in optimization of TMD using time-domain responses as objective function. The results were compared with other metaheuristic algorithms in mean of computational time and robustness of finding optimum results.

2. DYNAMIC ANALYSIS OF STRUCTURE

The time history analyses used in the optimization process were obtained by the developed code using Matlab with Simulink [32]. The physical model of a SDOF structure with a TMD on the top is given as Figure 3. The mass, stiffness and damping coefficient of SDOF structure were shown as m , k and c , respectively. The displacement of the structure is x and the displacement of the TMD is x_d . The TMD parameters are mass (m_d), stiffness (k_d) and damping (c_d) coefficients.

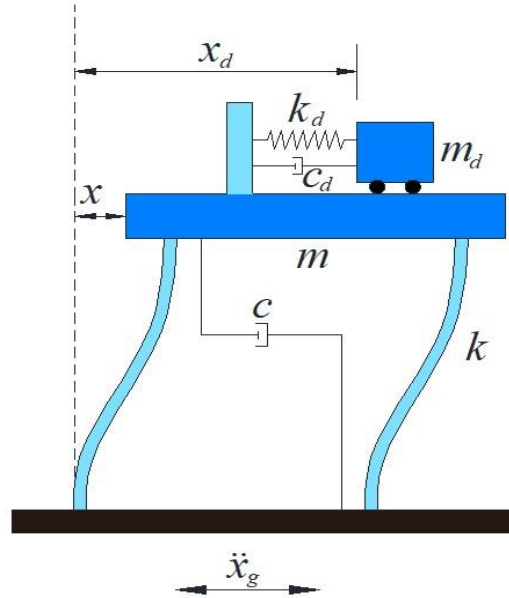


Figure 3. The physical model

The ground excitation is denoted with \ddot{x}_g . In that case, the equation of motion of SDOF structure is written as Eq. (6).

$$m\ddot{x} + c\dot{x} + kx = -m\ddot{x}_g \quad (6)$$

A dot on x represents a derivation respect to time. When a TMD is added to SDOF structure, the two coupled equations of motions are as follows:

$$m\ddot{x} + (c + c_d)\dot{x} - c_d\dot{x}_d + (k + k_d)x + k_d x_d = -m\ddot{x}_g \quad (7)$$

$$m_d\ddot{x}_d - c_d\dot{x} + c_d\dot{x}_d - k_d x + k_d x_d = -m_d\ddot{x}_g \quad (8)$$

3. THE OPTIMIZATION METHODOLOGY

In this study, two hybrid algorithms were investigated and these hybrid algorithms are combination of FPA, TLBO and JA. FPA is a nature inspired metaheuristic algorithm developed by Yang [33]. FPA uses the pollination process of flowering plants with phases of global and local pollination chosen with a switch probability (sp). TLBO is a parameter free algorithm developed by Rao [34] and it imitates the teaching and learning process of a class. Two phases called teacher and learner (student) phases are used in optimization and these phases are consequently done without using a probability as algorithm parameter. JA is a single phase algorithm and it is also parameter free as TLBO [35]. The name of the algorithm comes from a Sanskrit word meaning victory. The optimum results were also compared with classical FPA, TLBO and JA. Also, the results were compared with the music inspired metaheuristic algorithm; HS [36].

The first hybrid algorithm is Jaya algorithm with probabilistic student phase (JA1SP). The following equation of Jaya algorithm is used as the first phase of the algorithm.

$$X_{new,i} = X_{old,i} + r_1(X_{best} - |X_{old,i}|) - r_2(X_{worst} - |X_{old,i}|) \quad (9)$$

This phase uses the best (X_{best}) and the worst (X_{worst}) existing solutions with the random number between 0 and 1 (r_1 and r_2). The design variable of i^{th} population and t^{th} iteration (X_i^t) is updated to find solution of next iteration (X_i^{t+1}).

The second phase of JA1SP is the student phase of TLBO as shown as Eq. (10). In this phase, two existing solutions (X_m^t and X_k^t) are used.



$$X_i^{t+1} = \begin{cases} X_i^t + r_1(X_m^t - X_k^t) & \text{if } OF(X_m) < OF(X_k) \\ X_i^t + r_1(X_k^t - X_m^t) & \text{if } OF(X_m) > OF(X_k) \end{cases} \quad (10)$$

The two phases are chosen in an iteration by using sp. The other hybrid algorithm is Jaya algorithm using Levy Flight with probabilistic student phase (JALSP). Differently from JA1SP, r_1 and r_2 random numbers are used as number generated by a Lévy distribution.

The solution; X contains the candidate values of design variables and these design variables are μ , T_d and $\xi_{d,opt}$. T_d is the period of TMD. The objective function (OF) is the minimization of the maximum structural displacement as shown in Eq. (11).

$$OF = \min(\max|x|) \quad (11)$$

The optimization problem has a constraints (g_1) shown as Eq. (12). g_1 is related with maximum stroke capacity and st_max is the maximum allowed limit.

The optimization is done by using 6 impulsive motions seen in near fault ground excitations. These excitations are modelled with the equation of Makris [37]. 3 flint steps and 3 directivity pulses are used. The critical result under these excitations are considered in OF.

$$g_1 = \frac{\max(|x_d - x|)_{with\ TMD}}{\max(x)_{without\ TMD}} \leq st_max \quad (12)$$

4. NUMERICAL EXAMPLE CASES

In this study, 2 SDOF structure with 1.5s and 2.5s natural periods were investigated. The inherent damping of structure is taken as 5%. The pulse periods are also 1.5s, 2s and 2.5s and peak ground velocity (PGV) is taken as 200 cm/s. st_max limit is 2. All algorithms have minimum 100 function generation and 20 independent run of the processes are done to investigate the robustness of the methods.

The ranges used in the optimization process are as follows:

μ : 0.01-0.1

T_d : 0.5-1.5 times of the natural period of SDOF structures

ξ_d : 0.01-0.3

The sp is taken as 0.5 to give equal probability to both phases of algorithms. The optimum results and the maximum responses are shown in Table 1. The results contain results of all constraints, objective function with average of 20 runs (OF_{ave}), analysis number of the optimum results found (n) and standard deviation of 20 run (sd).

Table 1. The optimum results

	Period (s)	μ	$T_d(s)$	ξ_d	Max(x) (m)		n	OF_{ave}	sd	Max(\ddot{x} + \ddot{x}_g) (m/s ²)	
					Without TMD	With TMD				Without TMD	With TMD
HS	1.5	0.099	1.747	0.234	1.028	0.997	646	1.001	0.003	21.224	17.019
	2.5	0.099	2.105	0.034	1.709	1.604	225	1.611	0.005	12.697	9.159
FPA	1.5	0.100	1.753	0.231	1.028	0.994	1000	0.999	0.016	21.224	17.014
	2.5	0.100	2.049	0.010	1.709	1.600	945	1.612	0.011	12.697	9.394
TLBO	1.5	0.100	1.753	0.231	1.028	0.994	930	0.995	0.002	21.224	17.012
	2.5	0.100	2.047	0.010	1.709	1.600	910	1.604	0.003	12.697	9.401
JA	1.5	0.100	1.753	0.231	1.028	0.994	985	0.995	0.003	21.224	17.014
	2.5	0.100	2.049	0.010	1.709	1.600	915	1.612	0.032	12.697	9.394
JA1SP	1.5	0.100	1.753	0.231	1.028	0.994	990	0.994	0.000	21.224	17.014
	2.5	0.100	2.049	0.010	1.709	1.600	985	1.603	0.011	12.697	9.394
JALSP	1.5	0.100	1.753	0.231	1.028	0.994	810	0.994	0.001	21.224	17.014
	2.5	0.100	2.049	0.010	1.709	1.600	905	1.601	0.002	12.697	9.394

5. CONCLUSION

The maximum displacement of structures with period 1.5s and 2.5s are 1.028m and 1.709m, respectively. For structure with 1.5s period, 3.3% reduction of maximum displacement is seen. For structure with 2.5s period,



6.1% reduction is seen for maximum displacement. These reductions may be small, but significant reduction of maximum accelerations can be seen. By the increase of the mass ratio, better reductions can be obtained, but the feasibility of the TMD must be checked because of the axial force capacity of the structure considering ductile behavior.

The best solution of HS is a little different than the solution of design variables with minimum objective function. The other ones have been the same optimum solution for the best of 20 runs. The average of 20 runs is the best for hybrid methods. Especially, JA1SP finds the best solution for all runs, because the sd value is zero. JA has the biggest sd value and the hybridization of JA with other ones are effective to prevent local optima problem for optimum tuning of mass dampers.

REFERENCES

- [1]. Frahm H. Device for damping of bodies. U.S. Patent No: 989,958, 1911.
- [2]. Miyamoto, H.K., Gilani, A.S.J., Gundogdu, Y.Z., 2011. Innovative Seismic Retrofit of an Iconic Building. In: Seventh National Conference on Earthquake Engineering, 30 May- 3 June, Istanbul, Turkey.
- [3]. Den Hartog, J.P. (1947), *Mechanical Vibrations*, McGraw-Hill, New York.
- [4]. Ormondroyd J, Den Hartog JP. The theory of dynamic vibration absorber. T ASME50:922, 1928.
- [5]. Bishop, R.E.D., Welbourn, D.B., 1952. The problem of the dynamic vibration absorber. *Engineering (London)*, 174 and 769.
- [6]. Snowdon, J.C., 1959. Steady-state behavior of the dynamic absorber. *Journal of the Acoustical Society of America* 31,10961103.
- [7]. Falcon, K.C., Stone, B.J., Simcock, W.D., Andrew, C., 1967. Optimization of vibration absorbers: a graphical method for use on idealized systems with restricted damping. *Journal Mechanical Engineering Science* 9,374381.
- [8]. Ioi, T., Ikeda, K., 1978. On the dynamic vibration damped absorber of the vibrationsystem. *Bulletin of the JSME* 21, 6471.
- [9]. Warburton, G.B. (1982), Optimum absorber parameters for various combinationsof response and excitation parameters, *Earthquake Engineering and Structural Dynamics*, 10, 381401.
- [10]. Sadek, F., Mohraz, B., Taylor, A.W. and Chung, R.M. (1997), A method of estimating the parameters of tuned mass dampers for seismic applications, *Earthquake Engineering and Structural Dynamics*, 26, 617635.
- [11]. Warburton, G.B., Ayorinde, E.O., 1980. Optimum absorber parameters for simplesystems. *Earthquake Engineering and Structural Dynamics* 8,197217.
- [12]. Hadi, M.N.S. and Arfiadi, Y. (1998), Optimum design of absorber for MDOFstructures, *Journal of Structural Engineering-ASCE*, 124, 12721280.
- [13]. Marano, G.C., Greco, R. and Chiaia, B. (2010), A comparison between different optimization criteria for tuned mass dampers design, *Journal of Sound and Vibration*, 329, 4880-4890.
- [14]. Singh, M.P., Singh, S. and Moreschi, L.M. (2002), Tuned mass dampers for response control of torsional buildings, *Earthquake Engineering and Structural Dynamics*, 31, 749769.
- [15]. Desu, N.B., Deb, S.K., Dutta, A. (2006), Coupled tuned mass dampers for controlof coupled vibrations in asymmetric buildings, *Struct. Control Hlth.*, 13, 897916.
- [16]. Pourzeynali, S., Lavasani, H.H., Modarayi, A.H. (2007), Active control of highrise building structures using fuzzy logic and genetic algorithms, *Eng. Struct.*, 29, 346-357.
- [17]. Leung, A.Y.T., Zhang, H., Cheng, C.C. and Lee, Y.Y. (2008), Particle swarm optimization of TMD by non-stationary base excitation during earthquake, *Earthquake Engineering and Structural Dynamics*, 37, 1223-1246.
- [18]. Leung, A.Y.T. and Zhang, H. (2009), Particle swarm optimization of tuned massdampers, *Engineering Structures*, 31, 715-728.
- [19]. Steinbuch, R. (2011), Bionic optimisation of the earthquake resistance of highbuildings by tuned mass dampers, *Journal of Bionic Engineering*, 8, 335-344.
- [20]. Bekdas, G. and Nigdeli, S.M. (2017), Metaheuristic based optimization of tunedmass dampers under earthquake excitation by considering soil-structure interaction, *Soil Dynamics and Earthquake Engineering*, 92, 443-461.
- [21]. Nigdeli, S.M. and Bekdas, G. (2017), Optimum tuned mass damper design infrequency domain for structures, *KSCE Journal of Civil Engineering*, 21(3), 912922.
- [22]. Zhang, H. Y. and Zhang, L. J. (2017). Tuned mass damper system of high-riseintake towers optimized by improved harmony search algorithm. *Engineering Structures*, 138, 270-282.
- [23]. Nigdeli SM, Bekdas G, Aydn A. Metaheuristic based optimization of tuned massdampers on single degree of freedom structures subjected to near fault vibrations. 3rd International Conference on Engineering and Natural Sciences (ICENS 2017), 3-7 May 2017, Budapest, Hungary.
- [24]. Bekdas G, Nigdeli SM, Aydn A. Optimization of Tuned Mass Damper for MultiStory Structures by using Impulsive Motions. 2nd International Conference on Civil and Environmental Engineering (ICOCEE 2017), 8-10 May 2017, Cappadocia, Turkey.
- [25]. Farshidianfar, A., Soheili, S. (2013), Ant colony optimization of tuned massdampers for earthquake oscillations of high-rise structures including soilstructure interaction, *Soil Dyn. Earthquake Eng.*, 51, 14-22.
- [26]. Farshidianfar, A., Soheili, S. (2013), ABC optimization of TMD parameters for tallbuildings with soil structure interaction, *Interact. Multiscale Mech.*, 6, 339-356.



- [27]. Nigdeli SM, Bekdas G, Yang X-S (2017), Optimum Tuning of Mass Dampers by Using a Hybrid Method Using Harmony Search and Flower Pollination Algorithm. In: Harmony Search Algorithm. Advances in Intelligent Systems and Computing, vol 514, Del Ser J. (eds) Springer, pp. 222-231.
- [28]. Nigdeli SM, Bekdas G (2015), Teaching-Learning-Based Optimization for Estimating Tuned Mass Damper Parameters. 3rd International Conference on Optimization Techniques in Engineering (OTENG '15), 7-9 November 2015, Rome, Italy
- [29]. Bekdas G, Nigdeli SM, Yang X-S. A novel bat algorithm based optimum tuning of mass dampers for improving the seismic safety of structures. *Engineering Structures* 2018; 159:89-98.
- [30]. Bekdas G, Kayabekir AE, Nigdeli SM, Toklu YC. Transfer Function Amplitude Minimization for Structures with Tuned Mass Dampers Considering Soil-Structure Interaction, *Soil Dynamics and Earthquake Engineering*, 2019; 116: 552-562.
- [31]. Bekdas G, Ulusoy S, Nigdeli SM, Optimum Tuning of Mass Dampers by Impulsive Motions and Several Metaheuristic Methods. 3rd International Conference on Civil and Environmental Engineering (ICOCEE), 24-27 April 2018, Izmir, Turkey.
- [32]. MathWorks, M. U. S. G. (1992). the Mathworks. Inc., Natick, MA.
- [33]. Yang, X.-S. (2012), Flower pollination algorithm for global optimization. In *unconventional computation and natural computation*, 240-249.
- [34]. Rao, R. V., Savsani, V. J. and Vakharia, D. P. (2011). Teaching-learning-based optimization: a novel method for constrained mechanical design optimization problems. *Computer-Aided Design*, 43(3), 303-315
- [35]. Rao, R. (2016). Jaya: A simple and new optimization algorithm for solving constrained and unconstrained optimization problems. *International Journal of Industrial Engineering Computations*, 7(1), 19-34.
- [36]. Geem, Z.W., Kim, J.H. and Loganathan, G.V. (2001), A new heuristic optimization algorithm: harmony search, *Simul.*, 76, 6068.
- [37]. N. Makris, Rigidity-Plasticity-Viscosity: Can Electrorheological Dampers Protect Base-Isolated Structures From Near-Source Ground Motions. *Earthquake Engineering and Structural Dynamics*, 26, 571-591, 1997.

BIOGRAPHY

Sinan Melih Nigdeli, Associative Professor, is researcher in Structural Control and Optimization at Istanbul University. He obtained his DPhil in Structural Engineering from Istanbul Technical University with a thesis subject of active structural control. He co-organized the 15th EU-ME Workshop: Metaheuristic and Engineering in Istanbul. In optimization and structural control, he organized several mini-symposiums or special sections in prestigious international events. He co-edited *Metaheuristics and Optimization in Civil Engineering* published by Springer in 2016 and he is one of the guest editors in 2017 special issue of *KSCE Journal of Civil Engineering*. He has authored more than 150 papers for journals and scientific events.



Optimum Design of T-Beams Using Jaya Algorithm

Aylin Ece Kayabekir¹ Gebrail Bekdas² Sinan Melih Nigdeli³

Abstract

The main goal of an engineer is to find the best suitable design with the minimum cost. For that reason, the optimization of an engineering design is important. Engineering optimization problems are non-linear because of high number of design constraints. Especially, optimum cost design of reinforced concrete (RC) members has several types of constraints. For example, the optimum design problem of RC beams has behavior, strength and constructive constraints. To consider these constraints, a metaheuristic algorithm called Jaya Algorithm (JA) is employed in the development of the cost optimization method. JA is a single-phase algorithm considering best and worst existing solutions in an iteration. Because of this, it has a good convergence rate while the worst solution is diverged. Also, JA has no specific parameters. In the present study, the numerical example is compared with the classical solutions and the proposed method is effective to find the optimum design for singly reinforced RC beam.

Keywords: cost minimization, design optimization, Eurocode, RC beams, Jaya Algorithm.

1. INTRODUCTION

During the engineering design process, major goals of providing safety and minimum cost make using optimization methods inevitable. The optimization methods can be utilized all engineering fields such as civil engineering, computer engineering, mechanical engineering, electrical and electronic engineering etc.

In the recent years, metaheuristic algorithms are often used in the design process, because optimum solutions can be obtained fast with these algorithms in comparison to other classical optimization methods. Genetic Algorithm (GA), Simulated Annealing (SA), Big Bang Big Crunch (BB-BC), Bat Algorithm (BA), Flower Pollination Algorithm (FPA), Harmony Search (HS), Teaching Learning Based Optimization (TLBO) and Jaya Algorithms (JA) are a few of these metaheuristic algorithms.

In all of the civil engineering fields, metaheuristic algorithms are employed for optimization application and the reinforced concrete (RC) members are one of the major optimization applications in civil engineering, because concrete and reinforcement steel has different behavior and optimum design with minimum cost can be very challenging without optimization methods. In the literature several studies related to optimum design objected minimum cost of RC members using metaheuristic methods are exist. For example, in the studies conducted by Coello et al., Govindaraj and Ramasamy, Fedghouche and Tiliouine, optimum design objected minimum cost of RC beams using GA algorithm have been investigated [1-3]. With a similar objective, Leps and Sejnoha utilized a hybrid form of metaheuristic algorithm using together SA and GA algorithms for RC continuous beams [4]. In addition to these, HS was also employed for continuous beams [5] and T-shaped RC beams [6,7]. Also, HS and BA algorithms were tested under several different flexural moments for singly or doubly reinforced beams [8] and efficiency of TLBO algorithm was investigated comparing with HS and BA algorithms [9], respectively.

¹ Corresponding author: Istanbul University-Cerrahpaşa, Department of Civil Engineering, 34320, Avcılar/İstanbul, Turkey. ecekayabekir@gmail.com

² Corresponding author: Istanbul University-Cerrahpaşa, Department of Civil Engineering, 34320, Avcılar/İstanbul, Turkey. bekdas@istanbul.edu.tr

³ Corresponding author: Istanbul University-Cerrahpaşa, Department of Civil Engineering, 34320, Avcılar/İstanbul, Turkey. melihnig@istanbul.edu.tr



In addition to optimum design with minimum cost, optimization can be applied for different objectives such as optimum design provided minimum stress on the structural elements, minimization of carbon dioxide CO₂ or weight minimization. In the study conducted by Koumousis and Arsenis, GA was employed for minimum weight design, a maximum uniformity and the minimum number of bars [10]. Yepes et al. using together Simulated Annealing and Glowworm Swarm Optimization algorithms investigated minimum both of cost and CO₂ emission of precast–prestressed concrete U-beam road bridges [11].

Apart from these, related to optimization of other RC members including columns [12,13], frames [14,15], retaining walls [16-20] and slabs [21] has been done with metaheuristic algorithms.

In this study, optimum design of T-shaped RC beams providing minimum cost was investigated using Jaya Algorithm (JA) which do not need user defined parameters as different from most of the metaheuristic algorithms. For that reason, during the optimization process, while total cost of concrete and reinforcement was assigned as objective function, cross-section dimensions and area of reinforcements were defined as design variables.

2. THE OPTIMIZATION PROCESS

JA which is one of the metaheuristic methods was developed by Rao and Jaya means victory [22]. This algorithm has no user defined parameter and it has a single phase. The equation of this algorithm is defined with Eq. (1). The convergence of the JA is provided by using the best (g^*) and worst (g_w) existing solutions in an iteration.

During the iteration process with JA, a set of candidate design variables are represented with x_i^{t+1} , where i is the number of sets of variables (population) and t is the step number.

$$x_i^{t+1} = x_i^t + r_1(g^* - |x_i^t|) - r_2(g_w - |x_i^t|) \quad (1)$$

The design variables are shown in Table 1 and T-shaped cross section of shown as Figure 1. Also, the ranges for the design variables are shown. Effective depth and cover of reinforcements have a defined value respect to the height of the beam. For these ranges and all constraints, the rules of Eurocode 2: Design of concrete structures [23] were considered.

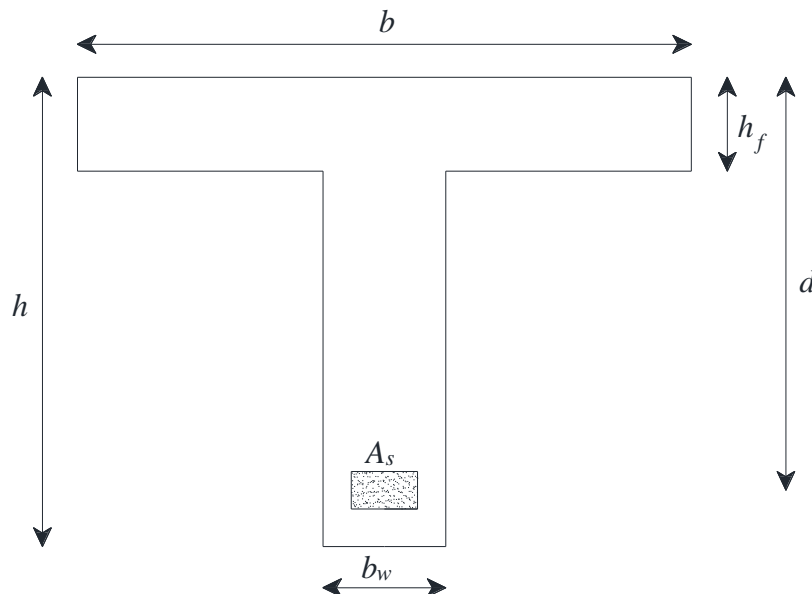


Figure 1. T-shaped cross section



The design constants of the problem are given as Table 2. The controlled design constraints are given as Table 3. The generation of a set of candidate solutions is done until all design constraints are provided in the optimization process.

Table 1. Design variables

Symbol	Definition	Range
b	Effective width of compressive flange [mm]	$b_w \leq b \leq \min [0.2L + b_w, 8h_f]$
b_w	Web width [mm]	$0.20d \leq b_w \leq 0.40d$
h	Height [mm]	$L/16 \leq h \leq 2.0$
h_f	Flange depth [mm]	$0.15 \leq h_f \leq d$
d	Effective depth [mm]	$d = 0.9h$
d_s	Cover of reinforcements [mm]	$d_s = 0.1h$
A_s	Area of reinforcing steel [mm ²]	$0 \leq A_s \leq 0.1$

Table 2. Design constants

Symbol	Definition
f_{ck}	Characteristic compressive strength for concrete
f_{cd}	Allowable compressive strength for concrete
f_{yd}	Characteristic yield strength of reinforcement
ρ_{max}	The maximum reinforcement ratio
ρ_{min}	The minimum reinforcement ratio
L	The length of beam
E_s	Young's elastic modulus for steel
M_{Ed}	The ultimate bending moment capacity
V_{Ed}	The ultimate bending moment capacity
C_s	The unit total cost of reinforcing steel
C_c	The unit total cost of concrete

Table 3. Design constraints

Constraint Number	Constraints
1	$\omega(1 - 0.5\omega) \leq 0.392$
2	$0.0035(0.8 - \omega)/\omega \geq f_{yd}/E_s$
3	$\rho_{min} \leq \rho \leq \rho_{max}$
4	$M_{Ed} \leq M_{Ed1}$
5	$V_{Ed} \leq V_{Rd max}$

The mentioned parameters in the Table 3 such as ω , ρ , M_{Ed1} and V_{Ed} are presented with Eq. (2-5).

$$\omega = (f_{yd}/f_{cd})(A_s/b_w d) - (b - b_w)h_f/(b_w d) \quad (2)$$

$$\rho = A_s/(b_w d) \quad (3)$$

$$M_{Ed1} = f_{cd}(b - b_w)h_f(d - 0.50h_f) + f_{cd}b_w d^2 \omega(1 - 0.5\omega) \quad (4)$$

$$V_{Rd max} = v_1 f_{cd} b_w z / (\tan(45) + \cot(45)) \quad (5)$$

In these equations, v_1 is a non-dimensional coefficient and z is the lever arm. The formulations of these parameters can be seen in Eq. (6) and Eq. (7), respectively.

$$v_1 = 0.6(1 - f_{ck}/250) \quad (6)$$

$$z = 0.9d \quad (7)$$

The objective function is the total material cost (C) of the beam as given in Eq. (8).

$$C = b_w d + (b - b_w)h_f + (C_s/C_c)A_s \quad (8)$$



In Figure 2, the optimization process is shown in a general flowchart of metaheuristic algorithms.

3. NUMERICAL EXAMPLE

As the numerical example, a RC T-beam with pinned supports is investigated. The beam is used for an overhead crane. The example is previously optimized by Fedghouche and Tiliouine [3] by using GA. The design constants of the problem are shown as Table 4. The optimum results are presented in Table 5 with GA and classical design results.

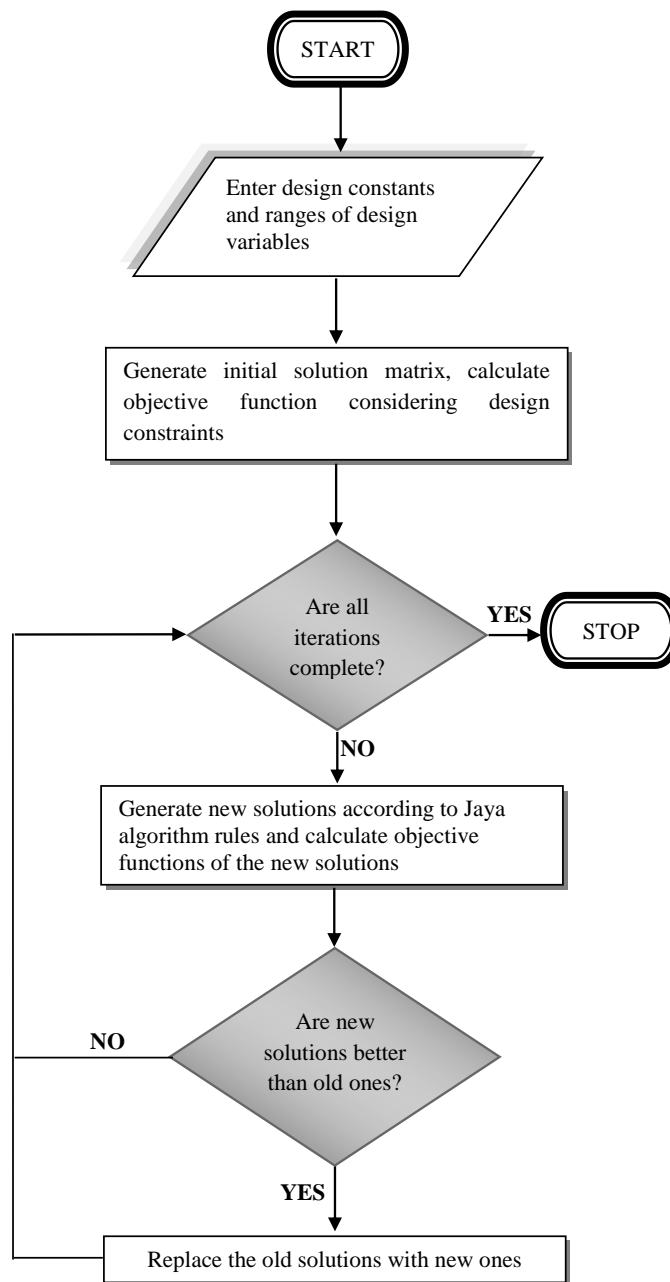


Figure 2. The flowchart of the optimization process



Table 4. Design constants of numerical example [3]

Symbol	Values
f_{ck}	20 MPa
f_{cd}	11.33 MPa
f_{yd}	348 MPa
ρ_{max}	0.04
ρ_{min}	0.0013
L	20 m
E_s	200000 MPa
M_{Ed}	4.991 N.m
V_{Ed}	1.039 N
C_s / C_c	36

Table 5. Optimum Design Variables

Design variables	Classical solution [3]	Optimum Results (GA) [3]	Optimum Results (JA)
b (m)	1.2	1.2	1.137450
b_w (m)	0.4	0.30	0.304476
h (m)	1.6	1.67	1.691535
h_f (m)	1.46	1.50	1.522382
d (m)	0.14	0.15	0.150009
A_s (m ²)	0.011702	0.01143	0.011404
ω	0.424	0.477	0.486112
C/C_c	1.117272	0.999221	0.999036

4. CONCLUSIONS

According to the results, a little improvement is provided for optimum results by using JA, which is simply to apply comparing to GA. Also, the importance of the optimization is clearly seen by the cost difference between optimum results and classical solution. In the example presented in the paper, singly reinforced beams were considered. In future studies, doubly reinforced beams can be optimized according to Eurocode 2 [23].

REFERENCES

- [1]. C. C. Coello, F. S. Hernandez and F. A. Farrera, "Optimal Design of Reinforced Concrete Beams Using Genetic Algorithms," *Expert Systems with Applications*, vol. 12, pp. 101-108, 1997.
- [2]. V. Govindaraj, J. V. Ramasamy, "Optimum detailed design of reinforced concrete continuous beams using Genetic Algorithms," *Comput. Struct.*, vol. 84, pp. 34-48, 2005. DOI:10.1016/j.compstruc.2005.09.001.
- [3]. F. Fedghouche, B. Tiliouine, "Minimum cost design of reinforced concrete T-beams at ultimate loads using Eurocode2," *Eng. Struct.*, vol. 42, pp. 43-50, 2012. DOI:10.1016/j.engstruct.2012.04.008
- [4]. M. Leps and M. Sejnoha, "New approach to optimization of reinforced concrete beams," *Comput. Struct.*, vol. 81, pp. 1957-1966, 2003. DOI:10.1016/S0045-7949(03)00215-3.
- [5]. A. Akin and M.P. Saka, "Optimum Detailed Design of Reinforced Concrete Continuous Beams using the Harmony Search Algorithm," in *The Tenth International Conference on Computational Structures Technology*, 2010, paper 131.
- [6]. G. Bekdas and S. M. Nigdeli, "Cost Optimization of T-shaped Reinforced Concrete Beams under Flexural Effect According to ACI 318, in *3rd European Conference of Civil Engineering*, 2012.
- [7]. G. Bekdas and S. M. Nigdeli, "Optimization of T-shaped RC Flexural Members for Different Compressive Strengths of Concrete," *International Journal of Mechanics*, vol. 7, pp. 109-119, 2013.
- [8]. G. Bekdas, S. M. Nigdeli, X. Yang, "Metaheuristic Optimization for the Design of Reinforced Concrete Beams under Flexure Moments,"
- [9]. G. Bekdas and S. M. Nigdeli, "Optimum Design of Reinforced Concrete Beams Using Teaching-Learning-Based Optimization," in *3rd International Conference on Optimization Techniques in Engineering (OTENG'15)*, 2015, p. 7-9.
- [10]. V. K. Koumousis and S. J. Arsenis, "Genetic Algorithms in Optimal Detailed Design of Reinforced Concrete Members," *Comput-Aided Civ. Inf.*, vol. 13, pp. 43-52, 1998.
- [11]. V. Yepes, J. V. Martí and T. García-Segura, "Cost and CO2 emission optimization of precast-prestressed concrete U-beam road bridges by a hybrid glowworm swarm algorithm," *Automation in Construction*, vol. 49, pp. 123-134, 2015.
- [12]. M. Y. Rafiq and C. Southcombe, "Genetic algorithms in optimal design and detailing of reinforced concrete biaxial columns supported by a declarative approach for capacity checking," *Comput. Struct.*, vol. 69, pp. 443-457, 1998.



- [13]. L. M. Gil-Martin, E. Hernandez-Montes and M. Aschheim, "Optimal reinforcement of RC columns for biaxial bending," *Mater. Struct.*, vol. 43, pp. 1245–1256, 2010.
- [14]. C. V. Camp, S. Pezeshk and H. Hansson, H., "Flexural Design of Reinforced Concrete Frames Using a Genetic Algorithm," *J Struct. Eng.-ASCE*, vol. 129, pp. 105-11, 2003.
- [15]. V. Govindaraj and J. V. Ramasamy, "Optimum detailed design of reinforced concrete frames using genetic algorithms," *Eng. Optimiz.*, vol. 39(4), pp. 471–494, 2007.
- [16]. B. Ceranic, C. Fryer and R.W. Baines, "An application of simulated annealing to the optimum design of reinforced concrete retaining structures," *Comput. Struct.*, Vol.79, pp. 1569–1581, 2001.
- [17]. C. V. Camp and A. Akin, "Design of Retaining Walls Using Big Bang–Big Crunch Optimization," *J Struct. Eng.-ASCE*, vol. 138(3), pp. 438–448, 2012.
- [18]. A. Kaveh and A.S.M. Abadi, "Harmony search based algorithms for the optimum cost design of reinforced concrete cantilever retaining walls," *International Journal of Civil Engineering*, vol. 9 (1), pp.1-8, 2011.
- [19]. S. Talatahari, R. Sheikholeslami, M. Shadfaran and M. Pourbaba, "Optimum Design of Gravity Retaining Walls Using Charged System Search Algorithm," *Mathematical Problems in Engineering*, vol. 2012, Article ID 301628.
- [20]. Temur, R and Bekdas, G. "Teaching learning-based optimization for design of cantilever retaining walls," *Structural Engineering and Mechanics*, vol.57(4), pp.763-783, 2016. DOI: 10.12989/sem.2016.57.4.763
- [21]. Sahab, M.G., Ashour, A.F and Toropov, V.V., "Cost optimisation of reinforced concrete flat slab buildings," *Eng. Struct.*, vol.27, pp.313–322, 2005. DOI:10.1016/j.engstruct.2004.10.002
- [22]. Rao, R. "Jaya: A simple and new optimization algorithm for solving constrained and unconstrained optimization problems." *International Journal of Industrial Engineering Computations* 7.1 (2016): 19-34.
- [23]. EN (Veranst.): EN 1992-1-1 Eurocode 2: Design of concrete structures. Brussels : CEN, 2005



Antifouling PEBA Membranes for Biobutanol Recovery by Pervaporation

Ayca Hasanoglu¹Aslihan Calhan¹, Sennur Deniz¹, Tulin Arasoglu²

Abstract

Biobutanol is an attractive biofuel which has potential to become an alternative to conventional fuels in the future due to the growing demand for energy. Butanol can be produced by ABE fermentation. Pervaporation is considered one of the most promising techniques to recover the butanol from the fermentation broth.

In this study polyetherblock amid (PEBA) pervaporation membranes were developed for butanol separation. Membranes were prepared with 5 % (wt) of PEBA solution in butanol by solvent evaporation. In order to enhance selective properties of the membrane and to give antifouling characteristics to the membrane, copper based metal organic framework particles, MOF-199, were incorporated in the membrane. Membranes were prepared at 5 and 10% (wt) of MOF-199 loadings. Pervaporation tests were carried out using membranes with and without MOF-199 to investigate the effect of the MOF-199 in the membrane. Best results were achieved with 5% MOF-199 loading. The fluxes and separation factors were in the range of 348.8-1379.0 g.m⁻².h⁻¹ and 18.6-24.8, respectively. To investigate the antifouling characteristics of the membrane, BSA adsorption on the membranes were carried out at several MOF-199 loadings. The adsorption of BSA molecules onto the membranes decreased with increasing MOF-199 content, indicating that the MOF particles give antifouling properties to the membrane. Also to determine the antibacterial activity of the membranes disk diffusion and agar well diffusion tests were applied. An antibacterial activity was not observed as a result of the experiments. The developed membranes have good potential for the recovery of the butanol from the fermentation broth.

Keywords: PEBA membrane, antifouling, pervaporation, butanol

1. INTRODUCTION

Biobutanol is an attractive biofuel which has gained high interest in recent years. It has superior properties compared to bioethanol. For example, it is less corrosive and evaporative, and it has higher combustion energy [1,2]. Biobutanol can be produced by fermentation of biomass by microorganisms usually *Clostridium* spp. This process is called ABE fermentation because the produced solvents are acetone, butanol and ethanol. One of the major drawback in ABE fermentation is the low production efficiency thus the recovery of butanol from ABE mixtures becomes more important in terms of the total costs. Conventional methods to recover butanol include mostly distillation yet the other methods are liquid-liquid extraction, gas stripping, perstraction and reverse osmosis [3]. Pervaporation is an alternative technique to conventional separation processes to recover the butanol. It has several advantages such as breaking azeotropes, low energy consumption and achieving high separation efficiency even for very dilute mixtures. In the literature pervaporation is considered one of the most promising techniques to recover the butanol from the fermentation broth [4]. Several studies reported for pervaporation separation of butanol from aqueous solutions and the researches indicate that high separation efficiencies could be achieved by pervaporation [5-9]. In pervaporation a liquid mixture in contact with a dense membrane and the separation is governed by the affinity and diffusivity of the component with the membrane material. Thus it is important to develop specific membrane for the target component to be separated. In this study polyetherbioxamide (PEBA) membrane is used as the polymer matrix. The use of PEBA membranes in pervaporation is advantageous since it unifies the characteristics of rigid polyamide segments and flexible polyether segments without crosslinking [10]. Besides it is highly hydrophobic thus it shows high performance for recovery of organic solvents from aqueous mixtures. In the literature some researchers reported that they recovered butanol from its aqueous mixtures using PEBA membrane via pervaporation with high separation efficiency [11,12]. To enhance the membrane performance, metal organic framework (MOF) fillers can be incorporated in the polymeric membrane because of its good compatibility with polymer matrix and versatile porosity [13]. In this study copper based metal organic framework fillers, MOF-199, were used as fillers. With

*Corresponding author: aymeric@yildiz.edu.tr

¹Yıldız Technical University, Department of Chemical Engineering, Davutpaşa, Istanbul, Turkey

²Yıldız Technical University, Department of Molecular Biology and Genetics, Davutpaşa Istanbul, Turkey



the inclusion of MOF fillers, as well as enhancing the membrane separation performance it was also aimed to prevent biofouling which may occur in fermentation processes.

2. EXPERIMENTAL

2.1. Materials

Polyetherblockamide (PEBA) 2533 was purchased from Arkema. 1-Butanol used as solvent was purchased from Merck Millipore. Copper (II) acetate monohydrate (98+ %, extra pure) and Trimethylamine (99 % pure) were purchased from Acros Organics (New Jersey, USA). 1,3,5-Benzenetricarboxylic acid (98 %) was obtained from Alfa Aesar (Kandel, Germany). Ethanol was purchased from J.T Baker Avantor Performance Materials. Dimethylformamide (DMF) was purchased from VWR International S.A.S. Dichloromethane (DCM) was purchased from Lab-Scan Analytical Sciences Ltd.

2.2. Membrane and MOF Filler Preparation

PEBA membranes were prepared by solvent evaporation technique. 5% (wt) of PEBA polymer was weighted and solved in 1-Butanol. Prepared solution was stirred in a magnetic stirrer for one day. Then this solution was stirred at 80°C for half an hour in the magnetic stirrer to obtain a homogeneous solution. After, the solution was cast onto the petri dish. The membrane was left to evaporate on the bench for two days at room temperature. Then the membrane was placed in the oven at 35°C for one day and the next day it was kept in the oven 70°C for one day. Subsequently the dry membrane was kept in the oven 50°C under the vacuum to remove the residue solvent in the membrane.

MOF-199 particles (also known HKUST-1) consisted of two main components; 1,3,5 benzenetricarboxylic acid and copper (II) acetate monohydrate. Two solutions were prepared for the synthesis of MOF-199 particles. 1 g 1,3,5 benzenetricarboxylic acid and 1.612 g Copper (II) acetate monohydrate were dissolved in a mixture of 8 ml of DMF, ethanol and water (8 ml each) by stirring them in a vessel. After these solutions were mixed, 0.5 ml trimethylamine was added. Then the solution was stirred 23h. Sky-blue colored solution was then washed 2 times with dimethylformamide (DMF) and 3 times with dichloromethane (DMC). After, centrifugation was carried out at 50 rpm for 20 min. The washed MOF-199 particles were placed in a beaker and allowed to dry in a closed area at room temperature.

To prepare the MOF incorporated PEBA membranes, first the dried MOF-199 particles were dispersed in 10 ml hexane for one day at the desired ratio (5 %, 10%, 20% wt of PEBA polymer). 5% PEBA solution was prepared in 1- Butanol as it was described. After, the dispersed particles were added to this polymer solution. Then this mixture was stirred with a magnetic stirrer for one day. The solution was cast on to the petri dish. The drying conditions were the same as the neat PEBA membrane drying conditions.

2.3. Pervaporation Setup

The pervaporation setup is given Figure 1. The membrane was placed in the membrane cell. The feed mixture was circulated through the upstream side of the membrane while vacuum was applied from the downstream side of the membrane. Every time intervals the collected permeate in the cold traps was weighed and injected to gas chromatography to calculate the flux, separation factor and the pervaporation separation index (PSI). The flux (J), separation factor (α) and PSI are calculated using the equations below where x is the mass fraction of the component in the mixture, A is the area (m²), t, is the time interval (h) and w is the mass of the permeate:

$$\alpha = \frac{(x_{BuOH}/x_{water})_{permeate}}{(x_{BuOH}/x_{water})_{feed}} \quad (1)$$

$$J = \frac{w}{(A.t)} \quad (2)$$

$$PSI = \alpha.J \quad (3)$$

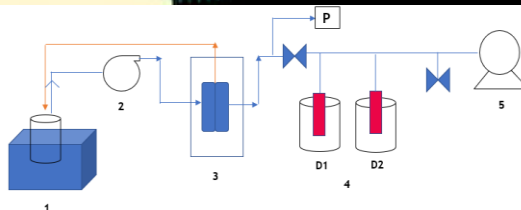


Figure 1. Pervaporation setup 1) Feed tank in water bath, 2) Peristaltic pump, 3) Membrane cell in temperature cabin 4) Cold traps of Dewar tanks 5) Vacuum pump

2.4. Antifouling Tests

BSA protein adsorption of the membranes was measured to test the antibiofouling properties. Membranes with different MOF loadings were immersed in flasks containing 1 mg/mL BSA solutions after they were saturated with water. The flasks were agitated for 3 days in the incubator and then the concentration values of the solution were read out using the UV spectrometer. The adsorbed amount of BSA molecules were calculated from the material balance.

2.5. Antibacterial Activity Tests,

The antibacterial activity of the prepared PEBA-MOF system was tested by three different methods including disk diffusion and agar well diffusion. These methods were carried out separately for model E. Coli (Gram-negative, ATCC number: 25922) and S. aureus bacteria (Gram-positive, ATCC number: 25923) since they have different bacteria cell wall structure.

2.5.1. Preparation of bacterial working suspensions

The bacterial cultures used in this study were prepared by suspending isolated colonies from Mueller Hilton Agar. It was incubated at 37 °C and 200 rpm in an incubator overnight. Then, until the optical density was reached to 0.1-0.2 at 600 nm, the bacterial suspensions were diluted with sterile buffer solution. This measured value was assigned to the concentration of 10^8 colony forming-unit/ml (CFU ml⁻¹) which was used as bacterial working dilution in the antibacterial methods applied for the study.

2.5.2. Disk diffusion method

Disc diffusion study, which works with the diffusion principle, was carried out based on the EUCAST standard (April 2013, 'Antimicrobial susceptibility testing EUCAST disk diffusion method') with minor modifications explained as follows. A bacteria culture (which has been adjusted to 0.5 McFarland standard) was used to lawn agar plates evenly using a sterile swab. The prepared PEBA-MOF membranes at different concentrations of MOF (5-10-20 %) were cut into 17 mm in diameter and placed on this agar plates instead of disk, where this step was the modified step. These plates were incubated at 37 °C for 24 hours. Next day the antibacterial activity was evaluated according to the appearance of inhibition zone around the discs.

2.5.3. Agar well diffusion assay

Agar well diffusion study, which works with the diffusion principle, was performed as described by Arasoglu et al. [14] with minor modifications explained as follows. Bacterial study culture was inoculated onto Mueller-Hinton agar and then the wells were punctured. Test samples were placed in 50 ml PBS-containing flasks without bacteria and incubated in a 220 rpm at 37 °C for 2h. Then, 100 µL of inoculum from these flasks were taken and added in the wells. The plates were incubated at 37 °C for 24 hours. After, the antibacterial activity was evaluated according to the appearance of inhibition zone around the wells.

3. RESULTS AND DISCUSSION

3.1. Pervaporation Results

The effect of the MOF content in the membranes was investigated and different PV tests were carried out for separation of 5% of BuOH at 30°C using neat PEBA membrane and membranes with 5% and 10% MOF



loadings at a thickness of 60 μm . The separation factors and fluxes are shown in Figure 2, and the PSI values are shown in Table 1.

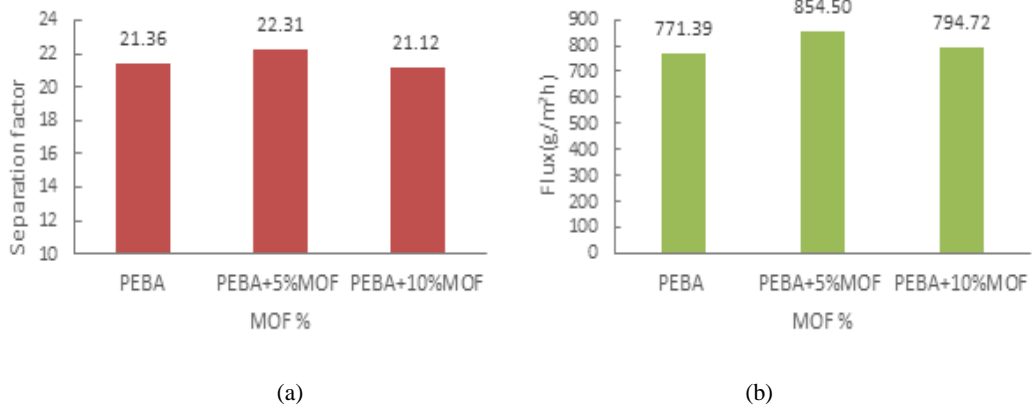


Figure 2. PV results of membranes with different amounts of MOF fillers (a) Separation factor (b) Flux

Table 1. PSI values of different membranes

	Neat PEBA	PEBA+5%MOF	PEBA+10%MOF
PSI	16479	19060	16786

As can be seen from Figure 2 and Table 1, the highest performance was achieved using 5%MOF fillers in the membrane. The presence of the filler in the membrane at this ratio increased the affinity of the membrane with butanol. Further comparisons were made with neat PEBA and PEBA at 5% of MOF loading. Next, the effect of BuOH concentration in feed at 30°C (between 2-5% BuOH) was investigated using membranes at a thickness of 110 μm . The results are shown in Figure 3.-

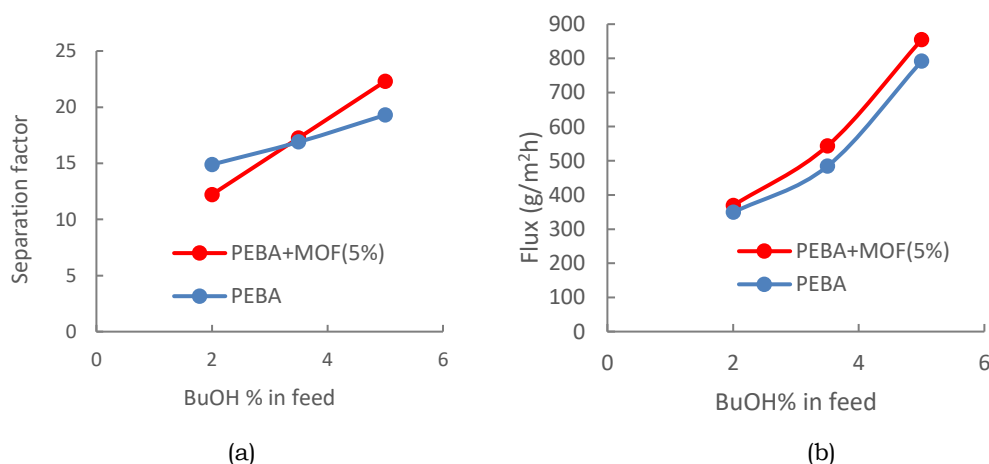


Figure 3. PV results of membranes with different amounts of MOF fillers (a) Separation factor (b) Flux

As can be seen from Figure 3, as the butanol concentration increased in feed, also separation factor and fluxes increased. The membrane with MOF filler gave better results than the neat membrane in terms of separation factor and flux. It can be concluded that the inclusion of MOF fillers in the membrane increased the PV efficiency by increasing the affinity with the membrane to butanol.

3.2. Adsorption Test Results

Biofouling is defined as undesirable accumulation of microorganisms at a phase transition interface which may occur by deposition, growth and metabolism of bacteria cells or flocs on the membranes. In fermentation processes an undesirable biofouling phenomenon may occur as a result of a biofilm formation on the membrane which is an additional resistance to mass transfer. This biofouling can be prevented with the addition of various fillers in the membrane by changing the polarity and surface charge of the membrane. The inclusion of copper based MOF fillers in the membrane may prevent this possible biofouling. In order to test this antibiofouling properties of the membranes, protein adsorption on the membranes was estimated using BSA protein as a model bacteria. The adsorption of BSA adsorption test results can be seen in Figure 4. As can be seen in Figure 4, as the MOF content increases in the membrane the adsorption amount of BSA. The adsorption of protein molecules on a

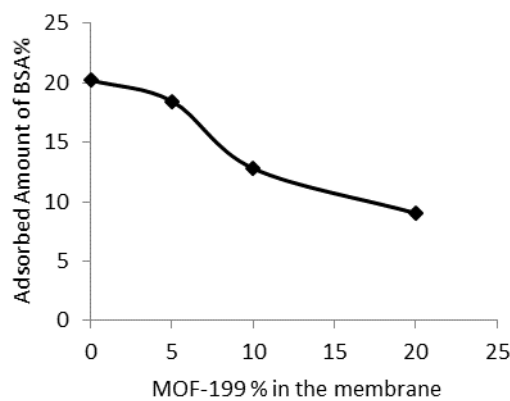


Figure 4 BSA adsorption on the membrane surface using different membranes

3.3. Antibacterial Activity Test Results

It is important that the copper based fillers in the membrane do not kill the bacteria in the fermentation broth by showing an antibacterial effect. Thus the antibacterial activity of the membranes were checked. Antibacterial activity of the growth inhibition zone with materials as represented containing the different concentrations of MOF (5-10-20 %) were evaluated using *E. coli* and *S. aureus* as model for Gram-negative and Gram-positive bacteria, respectively. The antibacterial activity was not observed in all experiments conducted with both strains. In the results of disk diffusion agar method, as shown Figure 5, the bacterial growth was not inhibited around the test samples placed on plates. Therefore, it was not observed the growth inhibition zone in this technic.

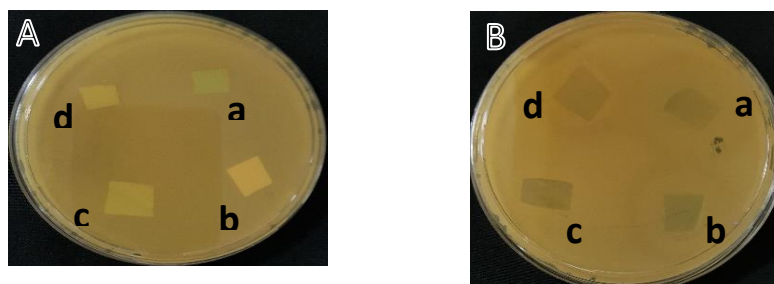


Figure 5. The results of disk diffusion method. A, the petri image of the MHA containing *E.coli*; B, the petri image of the MHA containing *S.aureus*. Names of test samples, respectively; a, PEBA; b, PEBA+MOF (5%); c, PEBA + MOF (10%), d, PEBA + MOF (20%)



The agar-well diffusion method results of the samples taken from the test samples agitated at 220 rpm for 2 hours at 37 ° C are shown in Figure 6, an inhibition zone which inhibits bacterial growth around the wells was not detected. Thus it can be concluded that the inclusion of the fillers in the membrane does not cause an antibacterial activity.

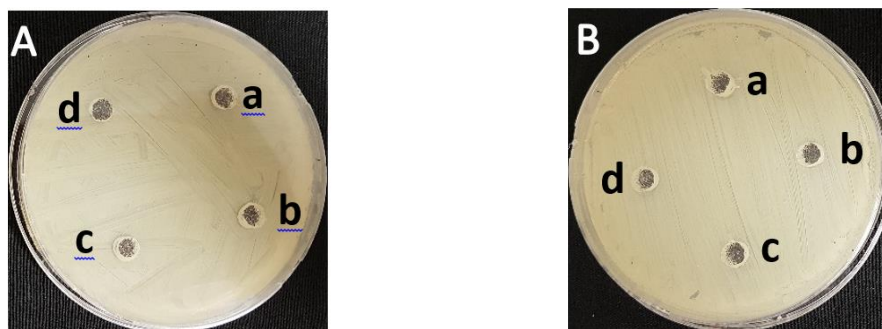


Figure 6. The results of agar well diffusion method. A, the petri image of the MHA containing *E.coli*; B, the petri image of the MHA containing *S.aureus*. Names of test samples, respectively; a, PEBA; b, PEBA+MOF (5%); c, PEBA + MOF (10%), c, PEBA + MOF (20%)

4. CONCLUSIONS

In this study PEBA membranes with copper based MOF fillers were developed for pervaporative separation butanol from it aqueous mixtures. The developed membranes were evaluated in terms of their separation performance, antifouling properties and antibacterial activity. Experimental results show that the presence of the MOF fillers inside the PEBA matrix enhanced the pervaporation performance by means of increasing the affinity of the membrane material with butanol. As well as enhancing the separation performance, the inclusion of MOF fillers inside the membrane decreased the protein adsorption onto the membrane surface indicating that the fillers may be used to prevent biofouling during the separation process. The experiments showed that the performance of the membrane can be improved with the incorporation of the fillers. Pervaporation results indicate that developed membranes have a good potential for n-butanol recovery from its aqueous mixtures. Further investigations can be carried out using the developed membranes for separation of real ABE solutions or to evaluate the mass transfer of other solvents in the mixture.

ACKNOWLEDGMENT

This work was supported by the Research Fund of Yildiz Technical University (Project No: 2015-07-01-KAP03).

REFERENCES

- [1]. Y. Li , W. Tang , Y. Chen , J. Liu , C. F. Lee “Potential of acetone-butanol-ethanol (ABE) as a biofuel”, *Fuel*, vol. 242 pp. 673-686. April 2019.
- [2]. M. F. Ibrahim, S.W. Kim, S. Abd-Aziz “Advanced bioprocessing strategies for biobutanol production from biomass”, *Renewable and Sustainable Energy Reviews*, vol. 91, pp. 1192-1204, Aug. 2018.
- [3]. B. Bharathiraja , J. Jayamuthunagai, T.Sudharsanaa, A.Bharghavia, R.Praveenkumar, M.Chakravarthy, D.Yuvaraj, Biobutanol “An impending biofuel for future: A review on upstream and downstream processing techniques”, *Renewable and Sustainable Energy Reviews*, vol. 68, pp.788-807, Feb. 2017.
- [4]. H.J. Huang, S. Ramaswamy, Y. Liu “Separation and purification of biobutanol during bioconversion of biomass”, *Separation and Purification Technology*, vol. 132, pp. 513-540, Aug. 2014.
- [5]. P. Rdzanek, J. Marszałek, W. Kamiński “Biobutanol concentration by pervaporation using supported ionic liquid membranes”, *Separation and Purification Technology*, vol. 196, pp. 124-131, 8 May 2018.
- [6]. M. Setlhaku, S. Heitmann, A. Gorak, R. Wichmann “Investigation of gas stripping and pervaporation for improved feasibility of two-stage butanol production process”, *Biores. Technol.* vol. 136, pp 102-108, May 2013.
- [7]. S.Y. Li, R. Srivastava, R.S. Parnas, Separation of 1-butanol by pervaporation using a novel tri-layer PDMS composite membrane, *Journal of Membrane Science*, vol. 363, pp 287-294, Nov. 2010.
- [8]. F. Liu, L. Liu, X. Feng “Separation of acetone–butanol–ethanol (ABE) from dilute aqueous solutions by pervaporation” *Separation and Purification Technology*, vol. 42, pp. 273–282, April 2005



- [9]. A. Rom, D. Esteve, A. Friedl “Organophilic pervaporation of butanol from an aqueous solution with POMS” *Chemical Engineering Transactions*, vol. 35, pp. 1315–1320, Oct. 2013.
- [10]. Q. Liu, Y. Li, Q. Li, G. Liu, G. Liu, W. Jin “Mixed-matrix hollow fiber composite membranes comprising of PEBA and MOF for pervaporation separation of ethanol/water mixtures”, *Separation and Purification Technology*, vol. 214, pp.2-10, May 2019.
- [11]. Yukai Li, Jie Shen, Kecheng Guan, Gongping Liu, Haoli Zhou, Wanqin Jin, PEBA/ceramic hollow fiber composite membrane for high-efficiency recovery of bio-butanol via pervaporation, *Journal of Membrane Science* , vol. 15, pp. 338-347, July 2016.
- [12]. W. Tanga, He Lou, Yifang Lib, Xiangbin Konga, Yanhui Wu, Xuehong Gu “Ionic liquid modified graphene oxide-PEBA mixed matrix membrane for pervaporation of butanol aqueous solutions”, *Journal of Membrane Science*, vol. 581, pp 93-104, July 2019.
- [13]. X.L. Liu, Y.S. Li, G.Q. Zhu, Y.J. Ban, L.Y. Xu, W.S. Yang “An organophilic pervaporation membrane derived from metal-organic framework nanoparticles for efficient recovery of bio-alcohols” *Angew. Chem.-Int. Ed.*, vol. 50 pp. 10636-10639, 2011.
- [14] Arasoglu, T., S. Derman, B., Mansuroglu, “Comparative evaluation of antibacterial activity of caffeic acid phenethyl ester and PLGA nanoparticle formulation by different methods”, *Nanotechnology*, vol. 27, pp. 1-12.

BIOGRAPHY

Ayca Hasanoglu received the B.Sc., M.Sc., and Ph.D degrees in Chemical Engineering from Yildiz Technical University in Istanbul, Turkey. She did doctoral studies in University of Oviedo, in Spain and a postdoctoral study, in University of Santiago de Chile between 2009-2010, in Chile. She has been working in Yildiz Technical University since 2000, where she is currently an associate professor. Her research interests include membrane engineering for wastewater, food and solvent recovery applications.



Systems of Systems: The Innovation phase - How are they born?

Dr. Avi Ginzburg¹

Abstract

In the last two decades there is an increased interest in System of Systems (SoS). The availability and affordability of communication and computers made many systems to connect to each other and create networks with different operators and stakeholders who collaborate to achieve common goals. There are many examples of SoS around us and they are part of our everyday life such as: Net Centric Warfare (NCW) System, air and land transportation, electric grid, logistics, hotel chains, navigation, banking etc... are all Systems of Systems. Communication, computers and miniaturization are the key enablers which are driving the evolution of systems into SoS. Those technologies are accelerating the high connectivity between many types of systems, data bases, processes' operators and stakeholders. Medium and large systems integrators industries have a growing interest in SoS. As they are always trying to move upwards the value chain in order to maintain their survivability and growth. Since systems are part of SoS even small companies must understand the new environment of SoS. To maintain growth companies must seek for introducing new systems, capabilities or processes to the market. Today this innovation phase is done in the environment of SoS. Shumpeter² claims that companies and even societies must innovate and introduce new systems in order to survive. This leads to the following most critical questions: How a System of Systems is born? What are the innovation processes the industry has to exercise in order to develop a new SoS, modify or introducing a new capability to an existing SoS? Are those processes similar to system's innovation? Or there are differences? – Those are important issues to be addressed by the academy and also by the industry in order to maintain their growth in a new world of complex SoS. Despite its importance and criticality there is not much in the literature about the innovation phase of SoS. Also there is a sever lack of engineering tools for SoS engineering to support innovation. In this paper we will discuss how Systems of Systems are born and in what aspect they are differ from Systems from the innovation point of view. We will introduce the "glue layer" concept as a new layer of SoS for engineering focus and innovation. Also we will recommend developing an innovative new engineering tool to support innovation within SoS environment.

I. INTRODUCTION: THE IMPORTANCE OF THE INNOVATION PHASE OF SOS

All industrial organizations must keep their growth in order to survive. As Shumpeter¹ stated organization which do not innovate are at a risk of destruction and he called the phenomenon: "creative destruction". Growth means mainly profit to stakeholders. Market driven and/or technology driven innovation is difficult to achieve especially in a competitive environment. Introducing a new product to the market earlier than your competitors is a dream of every industrial organization. Therefore there is a lot of literature on the innovation phase and many methods were developed to assist companies to do it. Systems are built of a mixture of subsystems and components. There are companies which are specialized in components, some in subsystems and some in systems. There are companies which have all stages of the value chain (Fig. 1) i.e. in components, subsystems and systems.

¹Head of Professional Program for Cyber Security and Senior Lecturer Systems Engineering, Israel Institute of Technology (IIT) Technion

Joseph Alois Schumpeter (German: [ˈjʊmpɛːtɐ]; 8 February 1883 – 8 January 1950) was an Austrian [political economist](#). Born in Moravia, he briefly served as [Finance Minister of Austria](#) in 1919. In 1932, he became a professor at [Harvard University](#) where he remained until the end of his career, eventually obtaining U.S. citizenship. One of the most influential [economists](#) of the 20th century, Schumpeter popularized the term "[creative destruction](#)" in [economics](#) (Wikipedia)

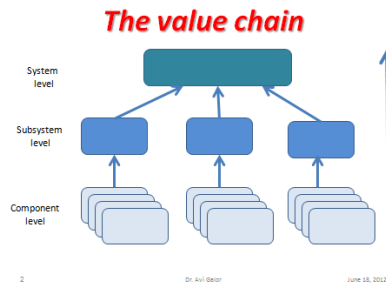


Fig. 1. - The value chain

Examples of systems are: cars, aircrafts, ships, computers etc. However, over time, when the technology matured, the industry split to those which are focused in developing and manufacturing component and those which are specialized in subsystems and those which are the systems integrators. For example first car manufacturers made most of the component and subsystems in house however today car companies are focusing on integration at the system level and bid for the subcontractors for the subsystems.

2. FROM SYSTEMS TO SYSTEM OF SYSTEM – THE BIRTH OF SOS

In the last decades a new upper state level was introduced to the system's value chain – the System of Systems level (SoS). SoS is formed of a cluster of different systems connected between them with independent stakeholders. There are many definitions in the literature of SoS, we will coin the following definition: "A collection of interconnected human operated systems". The major characteristic of SoS is that each System is human operated and free to make independent decisions. This means that SoS were existed in the past however the micro/ nano technologies accelerated the evolution of SoS. According to the above definition SoS is born out of more than two stakeholders who communicate and decide together to collaborate to achieve a common goal

Systems are very predictable even if they are human operated since we design them to follow exact embedded performance. One of the most powerful tools of Systems Engineering is simulation which enables us to predict the system's behavior to different stimuli.

However in SoS there is an interaction between the systems where one system human operator decision can affect the response of the other systems' human operator decisions. There is no pre predicted algorithm to estimate the response of each stakeholder response connected to the network. This means that we cannot predict the SoS behavior. SoS is not only about a larger complexity scale than each System by itself. There are many systems which are very complex however SoS introduce new dimension of complexity which derived from the human interaction in the network. Unlike Systems which are designed to perform a definite pre planned behavior a SoS has a goal or several goals to achieve and since it depends on human behavior it introduces an additional type of complexity.

3. THE “GLUE LAYER”

Electronics miniaturization accelerated communication and computer science and engineering. Systems were connected to each other rapidly and constructed networks (Fig 2.). In most cases it was an evolving process. Transfer of information is done over a communication “cloud”. Every system is driven by a different stakeholder and a member in the network and affects other members' behavior and influence the goal to be achieved.

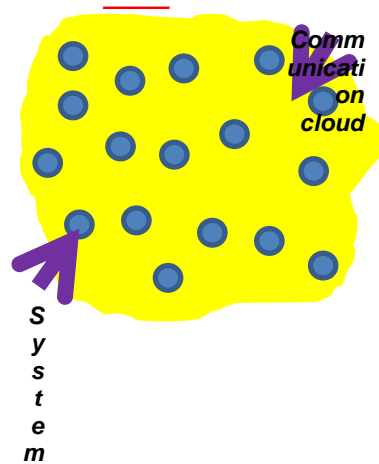


Fig. 2 - From System to SoS – the Network

Connectivity between systems in different networks evolved over the years and an Open System Interconnection (OSI) was introduced. Today it is common to describe OSI with a seven layer model depicted in Fig 3.

The Seven Layers of OSI

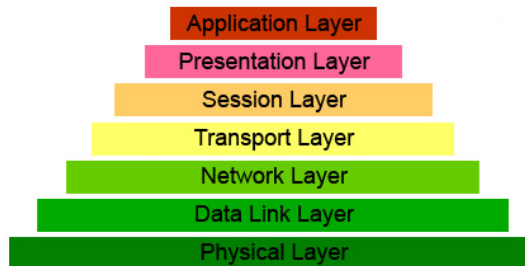


Fig. 3. - The Seven Layers model of OSI

SOS introduces an additional complexity due to the fact that they have different stakeholder and they evolved over time where new systems are connected to the network with their unique standards. This means that there is no “common language” between them SoS members. The distributed nature of the network and storage technology improvements results also with a distributed data bases rather than stored in a central storage this fact also enabling different systems with their stakeholders to be connected and join the network independently. Data release policy to the network members is done by the individual stakeholders which introduce even more complexity.

4. INNOVATION IN SOS

Innovation of SoS is involved with achieving:

- A New Common Goal (NCG) of members in the network.
- A New Capability (NC) of collection of systems which are part or SoS



This is similar to the ‘market pull’ notion in systems. A new goal or capability can be achieved only if part or all stakeholders will "play" together and collaborate. This is done by identifying gaps in the present goals or capabilities and NCG (or modification of existing goals) or NC is suggested to bridge the gap. Those NCG or NC that can also be achieved by SoS members collaboration and it means that there is a phase of negotiation between the members. Typically bridging those gaps can be done with: adding new system, new application, new/modifying policies or improving the “glue layer”.

Innovation of enablers for successful NCG or NC of the SoS i.e. improving communication channels, new subsystem or even adding a new system (with an independent stakeholder). This kind of innovation is similar to ‘technology push’ in systems thinking.

Since the backbone of a SoS is the Glue Layer (GL), existence of a GL is a necessary condition to create a SoS (Fig. 4). Systems Engineering evolved from the component level to subsystems towards systems. Traditionally innovation of systems includes introducing new features in each level. Systems thinking and innovation starts at the system level identifying improvements needed in its subsystems or its components.

Innovation from 5th wave

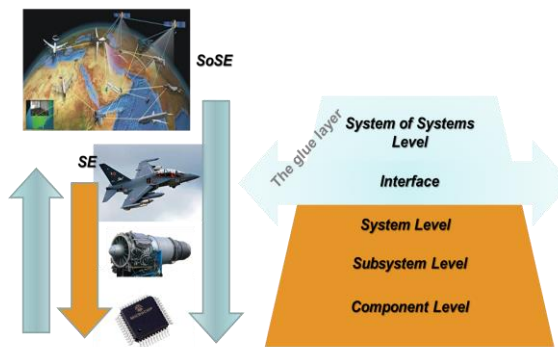


Fig. 4- Innovation from the 5th wave

In SoS the GL is introducing a new dimension which also adding a new area for innovation. The GL is about the interface between the stakeholders of its systems in a broader sense. The GL is where stakeholders exchange not only information but also: ideas, policies, agreements and disagreements. Over the GL collaborations are created to achieve NCGs. This new layer of innovation is called the 5th wave.² The 5th innovation wave includes: computers, communication technology, digital networks, distributed intelligence, software technology, information technology and micro/nano technologies.

5. SoS INNOVATION CHALLENGES

In the last years SoS engineering tools are developed however they are not mature enough which makes SoS innovation complicated. SoS Engineering do not have yet effective tools to asses new ideas impact on SoS in the ideation stage and even when we move to the feasibility we cannot predict the SoS behavior for a adding new system, policy change, communication channel replacement new application etc. SoS engineers do not have yet effective engineering tools and procedures to assist them in their innovation process. Those tools are essential for the innovation phase since they have to be used for design and validation of new concepts. The two major challenges are:

- a. Creating common language and mediation mechanism between systems’ stakeholders
- b. Simulating stakeholders’ behavior.

6. CREATING COMMON LANGUAGE BETWEEN SYSTEMS’ STAKEHOLDERS

As mentioned before SoS differs from a system by connecting between different systems which are controlled by their stakeholders. Therefore their ability to convey ideas over the network is crucial. This is more than



sending messages over communication channels of the network - it is about idea exchange like we do in free language between human beings. It is not about the data flows in the network it is about the content, the meaning of it and also interpretation of stakeholders for that content. We suggest doing it with semantic tools. Semantic tools can deal with different data bases types (structured and unstructured) and ideas. Semantic tools provide mediation mechanism between stakeholders where: RDF (Resource Description Framework) is a common model representation, OWL (Ontology Web Language) which is using RDF, inference tools, and rule base engines. This model is more appropriate for the distributed nature of a SoS where each stakeholder can use same basic algorithm to build his ontology map of the 'world' around him, make his own inference, take independent actions and convey data and ideas over the network to its members.

7. SIMULATING STAKEHOLDERS' BEHAVIOR

Additional feature we have in SoS is that we need to predict the systems' stakeholder who are members in the network. Without doing it the simulation tools describe only the network topology and data exchange between systems in the network. However SoS is also about the response of its' stakeholders to evolving situations in the network. This is more like trying to simulate social networks. SoS differs from mathematical models of static complex systems because at each mode there is a human operator. One of the options is to use intelligent agent technology to describe the human like behavior of the stakeholders who are member of the network.

8. SoS INNOVATION CHALLENGES

Innovation is about critical thinking however in SoS domain it involves with identifying gaps in goals we can achieve rather than in performance like in SE. The major challenges of SoS innovation are:

- Formalizing SoS innovation processes
- Procedures to handle independent systems with different stakeholders
- Designing several option to bridge gaps in SoS goals.
- Simulation of SoS as a tool for SoS innovation, design and validation
- Optimization of different solutions

9. SUMMARY AND FURTHER RESEARCH

Innovation phase of SoS differs from Systems innovation by the fact there are two new dimensions: (a) stakeholders are part of it, (b) network as a medium. The Glue Layer was introduced where stakeholders exchange data and ideas between them which enable them to mediate and collaborate toward new goals.

Innovation in SoS also includes the traditional innovation of SE but have a new challenge at the SoS level. Important enabler for SoS innovation are simulation tools. We suggest developing in SoS the concepts of Semantic tools and Intelligent Agent Technology to overcome the barriers of generating a common formal 'language' between stakeholder and simulating human like behavior representing them.

Further research is recommended to establish a model of innovation procedures for SoS and its simulation tools for architecting design, assessment and validation.

REFERENCES

- [1]. Creative Destruction by Richard Foster and Sarah Kaplan
- [2]. The Fifth Wave by Robrt Marcus, Collins Hemingway
- [3]. Model Integration Extracting Value from Model Based Systems Engineering, Henry Broodney, Uri Shani, Aviad Sela INCOSE 2013 International Symposium, Philadelphia

Joseph Alois Schumpeter (German: [ˈʃʊmpɛːtɐ]; 8 February 1883 – 8 January 1950)[was an Austrian political economist. Born in Moravia, he briefly served as Finance Minister of Austria in 1919. In 1932, he became a professor at Harvard University where he remained until the end of his career, eventually obtaining U.S. citizenship. One of the most influential economists of the 20th century, Schumpeter popularized the term "creative destruction" in economics (Wikipedia)

ICETI

3RD INTERNATIONAL CONFERENCE ON ENGINEERING TECHNOLOGY AND INNOVATION

www.iceti.org



WESTERN MICHIGAN
UNIVERSITY



University of
CINCINNATI



TURKISH
AIRLINES



CNRGROUP